THE UNIVERSITY OF CHICAGO

TIME-DEPENDENT RESPONSE OF THE GLOBAL OCEAN CIRCULATION TO CHANGES IN SOUTHERN OCEAN SURFACE WIND STRESS

A DISSERTATION SUBMITTED TO
THE FACULTY OF THE DIVISION OF THE PHYSICAL SCIENCES
IN CANDIDACY FOR THE DEGREE OF
DOCTOR OF PHILOSOPHY

DEPARTMENT OF THE GEOPHYSICAL SCIENCES

BY
HAILU KONG

CHICAGO, ILLINOIS
DECEMBER 2020

To my parents

All that is solid melts into air

TABLE OF CONTENTS

LIST OF FIGURES

LIST OF TABLES

ACKNOWLEDGMENTS

First and foremost, I would like to thank my advisor, mentor, and friend, Malte Jansen, for your effortless help in guiding me through this journey. Our weekly meetings have been such an inspiring experience for me; you really taught me how to do research and showed me what it means to be a true scientist and a nice person. I can never thank you enough.

I would also like to thank my committee members: Noboru Nakamura, Tiffany Shaw, and Doug MacAyeal, for providing constructive feedbacks to my research throughout the years. I have always been encouraged by our committee meetings. I also enjoyed the classes you taught so much.

I would like to thank other UChicago faculty: Liz Moyer, Dorian Abbot, Fred Ciesla, Mark Oreglia, and Jeff McMahon, whose classes I really enjoyed and well prepared me for my research.

I would like to thank the administrative staff in the department: David Taylor, Brian Lynch, Tom Indelli, Katie Casey, Jolene Hanchar, Aaron Hill, Sarah Lippert, and Victor Gavin. Your kind help has made graduate school such a smooth experience for me, especially for someone who comes from a different country.

I would like to thank my many good friends at DoGS, together we had so much joy: Pragallva, for our mutual support in making it through the graduate school, and for our comradeship in making the second Rossbypalooza fully flourish; Predrag, for our conversations, jokes, athletic and Chinese chess competitions, and the friendship between the glorious Yugoslavia and China; Grant, for our hanging-outs, discussions of politics, and cultural exchanges; Rich, Gabo, and Catlin, for how we started our graduate school together and also make it in the same year; Lei, Daniel, Feng, Jonah, Clare, Navah, and David, for all your kind help to a latecomer, and for the fun time we spent together; Zhihong, Huanzhou, Ziwei, Qi, Bowen, Hung-I, and Jenny, for all the awesome cuisines we enjoyed together and good time spent; Jun, Orli, Alice, Sina, Todd, Nathan, Osamu, and Tatsu, for the fun academic conversations we had and the group meetings you guys helped convened. It is you guys who made the department a place like

home for me. I will continuously miss all of you in the future.

I would like to thank the friends I made in our "Hyde Park Academic Group": Yukun, Yu, and Lixin, among many others. Our meetings and get-togethers immensely enriched my spiritual experience as a student at UChicago. You guys have shown me so many different possibilities outside my own field and life. I cannot imagine how these past six years in Chicago would have been without you guys. You guys truly made Hyde Park a place I hate to leave.

I would like to thank Jianghong, my good friend and awesome roommate since 2017, together we cooked so many tasty meals, watched numerous NBA games, and had so many conversations about life and the society. I wish you a successful qualify exam, and an exciting journey as an anthropologist. I would also like to thank Foling, my good friend at UChicago, ever since our "English as a second language" summer camp, for the conversations and thoughts we shared about so many aspects of life. I wish you a great journey in your future endeavors as a mathematician.

I would like to thank my friends from our Climate Dynamics group, and especially Lei, for creating such a wonderful platform. You guys brought me a true sense of scientific community, not to mention the great exposure to so many interesting topics in climate sciences.

I would like to thank my undergraduate thesis advisor, Yang Zhang, who first brought me the fascinating ideas behind atmospheric general circulation, wrote me a reference letter when I applied to the DoGS, and offered me opportunities to share my research with people from my undergraduate school.

I would like to thank my friends from my undergraduate program who also pursued their PhD studies in the U.S.: Xun, Bosong, Kang, Wandi, and Wenfu. I really cherish the community we built together throughout the graduate school. I wish you all a fantastic life in the future.

I would also like to thank my other friends from my undergraduate program who have stayed in China and always offered me the warmest welcome whenever I went back: Zhouyang, Lei, Gang, and Yun. I just want to say that I miss you guys so much.

I would like to thank my friends from our Second Drama Club in college: Tiancheng, Yu,

Xuezi, and Yichen. Thank you for bringing me different perspectives of the world while I was staying in the ivory tower studying turbulence. I wish we could sit down and read some plays again: Anton Chekhov, or David Hare.

I would like to thank my old friends from high school: Yanqing, Miao, Shuo, Song, Ran, Yan, and Han. More than ten years ago I never fancied life could bring us where we are now. I thank you for your company during the past six years in the U.S. and China, and wish you all the best that life can offer.

I would like to thank those authors whose writings accompanied me through Chicago's enduring nights: JIN Yucheng, Anton Chekhov, CAO Xueqin, Lan-ling Xiao-xiao Sheng, Earnest Hemingway, Alice Munro, and Tomas Tranströmer. Your works kept me alive as a human being.

I would like to thank my girlfriend Xun, for just being my girlfriend. Let's continue combating the nihility of life together.

I would like to thank my grandparents for all the love you gave me. Some of you will no longer know how far I have come across, but I want to let you know that I am well, and hope you all are well, too.

Finally, I would like to thank my mom and dad, for all that you have done for me, and for being the best mom and dad one can ever hope for in the world. I love you.

ABSTRACT

Geostrophic turbulent eddies are ubiquitous in Earth's oceans, but they are particularly active and important in the Southern Ocean where they mix properties such as heat, salinity, and chemical/biological tracers, thus controlling a key conduit between the surface and the deep ocean. This dissertation aims to improve our understanding of these eddies, and how they affect the responses of both the Southern Ocean and global ocean circulations to changes in Southern Ocean surface wind stress. Geostrophic eddies are usually too small for ocean general circulation models (GCM) to resolve, and therefore have to be parameterized. We first study the parameterization problem in barotropic β-plane turbulence with a quadratic bottom drag, which is arguably the most simplified yet relevant 2D model for the turbulence but has remained unexplored thus far. We propose a prognostic theory for the eddy diffusivity, a quantity that is central to eddy parameterizations. The theory matches well with a high resolution numerical model that fully resolves the eddies, and highlights the role of Rossby waves in suppressing turbulent mixing by their relative motions to the background mean flow. Second, we test state-of-the-art eddy parameterizations in several idealized channel models for the Southern Ocean, where high resolution simulations can be performed to compare to coarse resolution simulations with eddy parameterizations. We analyze the equilibrium response of the Southern Ocean circulation to changes in surface wind stress, and how bottom topography modulates this response. We find that topography significantly suppresses the Southern Ocean response through creating standing meanders, which amplify the turbulent mixing. The coarse resolution simulations with eddy parameterizations reproduce this suppression reasonably well. Third, we explore the equilibrium response of the global ocean circulation to Southern Ocean wind stress changes in an inter-hemispheric model, which builds upon the channel model by including a basin to the north, thus allowing us to explicitly model the interactions between the Southern Ocean and the basin. By comparing with a widely used theory for the global pycnocline depth, we show that the theory underestimates the equilibrium pycnocline depth while overestimating its sensitivity to wind stress changes, due to the theory's inaccurate treat-

ment of the low latitude upwelling. Last, we use the inter-hemispheric model to investigate the time-dependent response of the global ocean circulation to a sudden change in the Southern Ocean surface wind stress. We find that the pycnocline depth and the Antarctic Circumpolar Current (ACC) need multiple millennia to fully equilibrate, while the meridional overturning circulation (MOC) adjusts within several decades to a few centuries. Theoretical relations between the pycnocline depth and the ACC & MOC, which are accurate in the equilibrium state, break down throughout the adjustment processes. The relations break down because the responses of various circulation components depend on the ocean stratification at different depths, which adjusts on distinct timescales. This break-down explains why previous theories for the time-dependent response of global pycnocline depth have been unable to capture the multi-centennial adjustment timescale.

CHAPTER 1

INTRODUCTION

Geostrophic turbulent eddies are crucial in geophysical fluids for the transport and mixing of physical properties (e.g. heat, salinity) and chemical/biological tracers (e.g. CO_2). Therefore, to understand the global ocean circulation and biogeochemical cycles we need to first understand the geostrophic eddies.

Geostrophic eddies are prevalent in Earth's oceans, but are particularly active and important in the Southern Ocean, which is exceptionally important and unique among Earth's oceans. Being the only zonally reentrant ocean, it connects the other three major oceans and makes possible the exchanges of physical properties and chemical/biological constituents. This connection has important climatic implications. For example, deep, cold water sinks in the north Atlantic and upwells in the Southern Ocean, sequestering heat from the atmosphere and slowing down global warming (e.g. Talley, 2003). The upwelled water also dissolves large amounts of CO_2 before it downwells near Antarctica or flows into the Indo-Pacific, making the Southern Ocean an important carbon sink on Earth (e.g. Sabine et al., 2004).

The Southern Ocean circulation is fundamentally driven by surface westerlies, which push water equatorward through the Ekman transport in the surface Ekman layer (e.g. Marshall and Speer, 2012). The wind stress peaks around 53°S and decrease both equatorward and poleward (e.g. Lin et al., 2018). This structure results in a divergence of Ekman transport to the south of the wind stress peak, which sucks water up from the interior of the ocean into the surface layer, and a convergence of Ekman transport to the north of the peak, which pushes water down into the interior of the ocean from the surface. To replenish the loss of water due to the upwelling south of the wind peak, southward flow occurs in the deep ocean. These four branches of circulation thus form the wind-driven Southern Ocean meridional overturning circulation (SOMOC), which tilts the otherwise flat isopycnals and turns them into key passages for deep-surface ocean communications.

The SOMOC is also fundamentally affected by geostrophic turbulence. As the SOMOC tilts

the isopycnals, it increases the available potential energy and triggers baroclinic instability. As a consequence, meso-scale eddies[1] are excited. The eddies extract energy from the available potential energy, thereby flattening the isopycnals and creating the eddy-induced SOMOC, which counteracts the wind-driven SOMOC. The net result is the residual SOMOC, which is relevant for the transport of chemical/biological tracers (e.g. CO_2).

Apart from this zonally-averaged meridional circulation perspective, the major zonal current of the Southern Ocean is the Antarctic Circumpolar Current (ACC), the strongest ocean current on Earth. The ACC is dominantly baroclinic, maintained by a meridional buoyancy gradient across the Southern Ocean through the thermal wind relation. Specifically, at the surface, sea water gains buoyancy in the north via precipitation and radiative heating, while it loses buoyancy in the south through brine rejection and heat loss to the atmosphere. The slanted isopycnals, maintained by the aforementioned SOMOC, communicate the surface buoyancy gradient into the interior.

The Southern Ocean circulation profoundly influences ocean circulations elsewhere on Earth. One important example is that it controls the global ocean stratification through isopycnal slope, which results from an interplay between the surface wind stress and meso-scale eddies (e.g. Gnanadesikan, 1999; Wolfe and Cessi, 2010). Another important example is that the Southern Ocean brings the North Atlantic deep water (NADW), formed by the Atlantic meridional overturning circulation (AMOC), to the surface. The NADW is then split into intermediate water, which flows back northwards at a depth of a few hundred meters, and Antarctic bottom water (AABW), which sinks to the abyss around Antarctica, before spreading northward into the basins. Therefore, what drives the Southern Ocean circulation (e.g. surface westerlies) also influences ocean circulation elsewhere on Earth.

The westerlies over the Southern Ocean have been increasing for decades and are likely to continue to increase in the future (e.g. Swart and Fyfe, 2012). Given how significantly the global ocean circulation is influenced by the Southern Ocean surface westerlies, it is im-

1. In this work we use "meso-scale eddies" and "geostrophic turbulence" interchangeably.

portant to understand the circulation response to this wind stress change. Much progress has previously been made on the Southern Ocean circulation response to surface wind stress changes. Importantly, the "eddy compensation" theory proposes that the eddy-induced SOMOC will compensate the changes in the wind-driven SOMOC, leaving the residual SOMOC largely unchanged (Hallberg and Gnanadesikan, 2006; Viebahn and Eden, 2010). Additionally, the "eddy saturation" theory argues that the meso-scale eddies will keep the isopycnal slope, and hence (by thermal wind relation) the baroclinic ACC transport steady in response to any wind stress changes (Straub, 1993). Both of the arguments focus on the equilibrium responses in either idealized or regional models; only a few theoretical studies have considered the time-dependent response and adjustment of the northern basins (Jones et al., 2011; Allison et al., 2011; Samelson, 2011). These studies all predict a decadal adjustment timescale for the mid-depth stratification, which is significantly shorter than the centennial timescale found by their and others' simulations (e.g. Jansen et al., 2018).

The key to understanding the response of the global ocean circulation to changes in Southern Ocean surface wind stress are the meso-scale eddies. A major challenge is their small size: being only tens of kilometers in the Southern Ocean region, they are too computationally expensive for comprehensive general circulation models (GCMs) to fully resolve (e.g. Flato et al., 2013). Various eddy parameterizations have therefore been proposed, which relate the sub-grid scale eddy properties to resolvable large-scale circulation parameters. One popular method to parameterize the effect of meso-scale eddies is the diffusive closure, which assumes that the turbulence-induced tracer transport (or, specifically, the along-isopycnal component of the transport) can be related to the tracer's mean large-scale gradient, via an eddy diffusivity. The parameterization problem is then converted to one of determining this diffusivity.

In chapter 2 we aim to make progress towards improved parameterizations by proposing a prognostic theory for the eddy diffusivity (Kong and Jansen, 2017). We do so by considering a simplified geophysical fluid system, namely, the barotropic (i.e. 2D) β-plane turbulence with a quadratic bottom drag, which is arguably the most simplified yet relevant mathematical

model for Earth's oceans. We first review the classical scaling theories for the diffusivity and identify three regimes: the friction regime, the β regime, and a transition regime in between. We then propose a generalized prognostic theory for the eddy diffusivity in this model. An analytical model for the eddy flux of a passive tracer is derived from the spectral vorticity and tracer budget equations, which are closed by representing the non-linear eddy-eddy interactions as a combination of a stochastic forcing and a linear damping. This treatment allows us to analytically solve for the diffusivity at different spatial scales, before integrating to yield a bulk diffusivity that can be used in a parameterization. The solution illustrates how turbulent mixing is suppressed given a significant β, through relative motions of Rossby waves to the background mean flow. The generalized theory reduces to the classical scaling arguments in the limit regimes where either friction or the β-effect becomes dominant.

In chapter 3 we compare different state-of-the-art eddy parameterizations by investigating the response of the Southern Ocean circulation to changes in surface wind stress (Kong and Jansen, 2020, under revision). We consider two idealized channel setups of the Southern Ocean, one with flat bottom and one with moderately complex topography. In each setup we perform wind stress experiments with one group of high resolution simulations where the meso-scale eddies are fully resolved, and several groups of coarse resolution simulations where different state-of-the-art eddy parameterizations are implemented. We find that in the absence of topography, coarse resolution simulations significantly overestimate the sensitivity of the ACC transport to wind stress changes when comparing to the high resolution simulations, due to an underestimate of the sensitivity of transient eddy diffusivity. When topography is present, as a contrast, coarse resolution models capture the responses of both the ACC transport and the SOMOC reasonably well, due to the models' ability to resolve stationary eddies, which dominate over transient meso-scale eddies. Mechanistically, the presence of topography significantly suppresses the responses of both the ACC transport and the SOMOC by inducing standing meanders, which, by elongating the mixing contours and sharpening the cross-contour gradients, substantially enhance turbulent mixing.

In chapter 4 we investigate both the equilibrium and time-dependent responses of the global ocean circulation to changes in Southern Ocean surface wind stress. To do so we use an inter-hemispheric model, which is an extension of the channel model used in chapter 3 that includes a basin to the north of the channel. This configuration not only allows us to explore the global circulation outside of the Southern Ocean, but explicitly represents how the global ocean adjustment feeds back on the Southern Ocean circulation. For the equilibrium response, we find that the SOMOC and ACC transport in the inter-hemispheric model are relatively insensitive to Southern Ocean wind stress changes, consistent with previous findings. We compare the results with chapter 3 and find that the channel model setup with an adiabatic northern boundary condition significantly underestimates the ACC transport, while overestimating the sensitivity to wind stress changes. This is caused by the use of the adiabatic northern boundary condition, which presumes a perfect eddy compensation, hence distorting the response of the isopycnal structure. We also find that the inter-hemispheric model produces a similar SOMOC response to the channel model with a restoring northern boundary condition. We then compare the inter-hemispheric model simulations with a theory for the global pycnocline depth, proposed by Gnanadesikan (1999). We find that the theory underestimates the magnitude of the pycnocline depth while overestimating the sensitivity to wind stress changes, primarily because of an inaccurate treatment of low latitude upwelling.

For the time-dependent response, we find that the e-folding adjustment timescale for the ACC and global pycnocline depth is multi-centennial, while that for the SOMOC and AMOC is only multi-decadal. The remarkable difference is because the adjustment of the MOC only depends on the upper ocean stratification, which changes rapidly, while the adjustment of the ACC and pycnocline depth also relies on the abyssal ocean stratification, which responds much more slowly. This difference is not captured by existing two-layer theoretical models that include only one depth scale to represent the global pycnocline depth. Relatedly, we find that the relations between the pycnocline depth and the ACC & MOC that hold for equilibrium solutions, do not generally apply during the adjustment processes, again because the relations

do not account for the distinct stratification adjustment at different depths. These findings explain why previous theories significantly underestimated the adjustment timescale for the global pycnocline depth (Jones et al., 2011; Allison et al., 2011; Samelson, 2011) and suggest a pathway to improve the theories.

Finally, in chapter 5 we conclude with a summary and discussion of our main findings.

CHAPTER 2

THE EDDY DIFFUSIVITY IN BAROTROPIC β-PLANE TURBULENCE

2.1 Introduction

Geostrophic turbulent eddies are crucial in geophysical fluids for the transport and mixing of properties. However, in the earth's oceans they cannot be fully resolved by current IPCC-class climate models, due to their relatively small size (Flato et al., 2013). Therefore, their representation has to rely on adequate eddy parameterization schemes (e.g. Hallberg and Gnanadesikan, 2006; Downes and Hogg, 2013; Farneti et al., 2015). A common practice to parameterize sub-grid scale turbulence is to employ a diffusive closure, which assumes that unresolved eddy fluxes can be related to the large scale mean gradient via an eddy diffusivity. The eddy parameterization problem then comes down to expressing the eddy diffusivity based on resolvable large scale quantities. This paper aims to improve parameterizations for the eddy diffusivity by studying 2D turbulence as a reduced model for geostrophic turbulence.

2D turbulence is characterized by an inverse energy cascade. Once kinetic energy (KE) is created by forcing at small scales, it will be transferred to larger scales via non-linear eddy-eddy interactions, which will become increasingly sluggish as the scale increases. If large scale friction is present, a steady state can be achieved when the non-linear interaction becomes as slow as the energy dissipation rate by friction, and the cascade will be arrested at the so-called halting scale, where most of the energy will be found (e.g. Vallis, 2006).

The simplest case to study this phenomenon is f-plane turbulence with linear drag and forcing (e.g. Smith et al., 2002; Grianik et al., 2004). However, the f-plane approximation (i.e. the assumption of constant background vorticity) excludes dynamics that are crucial to large-scale geophysical fluids, such as the formation of Rossby waves. This limitation is overcome by the use of a β-plane approximation, which accounts for the importance of a planetary vorticity gradient. Unfortunately, including β significantly complicates the problem by adding a non-dimensional parameter. Moreover, the introduction of β can lead to anisotropy, where eddy

kinetic energy (EKE) is channeled into zonal modes, creating strong zonal flows or jets (Smith et al., 2002; Rhines, 1975; Vallis and Maltrud, 1993; Galperin et al., 2006) and suppressing meridional mixing.

While a linear drag is mathematically convenient, turbulent dissipation in the ocean's bottom boundary layer is arguably better described by a quadratic drag (e.g. Grianik et al., 2004; Holton, 2004). In fact, presently a quadratic drag is prevalently implemented in numerical ocean models (e.g. Willebrand et al., 2001; Egbert et al., 2004; Jansen et al., 2015). An important distinction lies in the dimensions: while a linear drag coefficient r provides a time scale (the inverse of the damping rate), a quadratic drag coefficient C_D has a dimension of inverse length in a barotropic model. (The effective quadratic drag coefficient for a barotropic flow is related to the standard non-dimensional C_D^* as $C_D = C_D^*/H$, where H is the depth of the flow.) As pointed out by Grianik et al. (2004), the quadratic drag coefficient by itself provides the halting scale in f-plane turbulence, which differs significantly from the linear drag case. The most realistic case of β-plane turbulence with quadratic drag has remained unexplored thus far and will be the focus of this work.

The two limit cases where either friction or β dominates can likely be understood from the existing work. Assuming that β is unimportant in the strong friction limit, the conclusions drawn from f-plane turbulence are expected to hold, such that the problem reduces to that studied by Grianik et al. (2004). In this case, the arresting scale solely depends on C_D. The turbulent flow in this regime is fully isotropic which implies the dominance of EKE over zonal mean KE, enabling the use of total KE as a good approximation to EKE. Therefore, once the KE budget is known, we can estimate both the characteristic eddy velocity and the halting scale. Finally, the eddy diffusivity can be formulated based on mixing length theory (Prandtl, 1925). Alternatively the scaling relationship for the eddy diffusivity can be derived directly from dimensional consideration, if we assume that β does not enter. In the strong β limit, a large amount of KE falls in the zonal mean mode whose amplitude is unknown a priori, but the characteristic turbulent eddy velocity can be determined dimensionally if we assume that

friction only affects the zonal jets. Meanwhile, the mixing length is given by the so-called β scale, which again follows directly from dimensional arguments, and is interpreted as the largest scale that is reached by the isotropic KE cascade (Smith et al., 2002; Vallis and Maltrud, 1993).

The regime where both friction and β matter (a transition regime) remains poorly understood, despite its relevance to Earth's ocean. Jansen et al. (2015) investigate the diffusivity for baroclinic turbulence for such an ocean-like transition regime and find that the mixing length is well approximated by the Rhines scale, even as the total KE remains dominated by the eddies. An equation for the EKE is formed based on a balance between the source of EKE and dissipation by quadratic bottom drag, which then is used to formulate an expression for the eddy diffusivity following standard mixing length theory. The resulting scaling relation provides a useful approximation over a wide range of idealized simulations in an ocean-like parameter regime.

A separate line of recent work has attempted to derive an expression for the eddy diffusivity analytically by linearizing the equation of motion for a single wavenumber, κ, representing the energy containing scale (Ferrari and Nikurashin, 2010, hereafter FN10; Klocker et al., 2012; Klocker and Abernathey, 2014, hereafter KA14). The resulting expression highlights the importance of mixing suppression by the relative propagation of eddies to the mean flow (hereafter "propagation-suppression argument"). (Srinivasan and Young, 2014, hereafter SY14) obtain the same result (albeit generalized in a number of ways) for a barotropic flow, and point out that it is in fact the intrinsic Rossby wave phase speed, arising from the meridional gradient of potential vorticity, that suppresses the eddy diffusivity. While all theories point towards the suppression of mixing for large β, it is not obvious how exactly the expression of FN10 or SY14 relates to the classical β-plane turbulence scaling arguments. We will show below that this connection can only be recovered by noting that mixing in reality is not necessarily dominated by the most energetic eddies. Adopting the linearization technique used in FN10, we have developed a generalized theory for the full diffusivity spectrum in barotropic turbulence,

whose integral yields a "bulk" diffusivity that agrees with simulations across all three regimes. This generalized theory is shown to reduce to the classical scaling relations for barotropic turbulence in the limit cases of strong β and strong friction. The idea of considering the full spectrum for the diffusivity is not new. In particular, Chen et al. (2015) proposed a way of representing the eddy diffusivity that takes into account the multi-scale nature of eddy and mean flow velocities. However, their formulation requires detailed knowledge of the flow field, and therefore remains a highly diagnostic theory. Our work aims to predict the eddy diffusivity based only on external parameters.

This study has four main goals: 1) document the results of a numerical exploration of barotropic turbulence on a β-plane with quadratic drag; 2) test previously proposed scaling arguments for the eddy diffusivity in the friction regime (Grianik et al., 2004), in the β regime (Vallis and Maltrud, 1993), and in the transition regime (Jansen et al., 2015); 3) develop a generalized theory for the eddy diffusivity based on the propagation-suppression argument of FN10; and 4) clarify the connection between the propagation-suppression theory and the classical scaling arguments for the eddy diffusivity in β-plane turbulence.

This paper is organized as follows. Section 2.2 introduces the equations of motion and the numerical model used to solve them. Section 2.3 discusses and tests the scaling arguments for 2D turbulence and mixing. In section 2.4 we derive a generalized theory for the eddy diffusivity, building on the propagation-suppression argument of FN10. Section 2.5 discusses the connections between the generalized theory and scaling arguments, and section 2.6 provides a concluding discussion.

2.2 Equations of motion and the numerical model

We want to study the turbulent flow on a β-plane, described by the barotropic vorticity equation

$$\frac{\partial q}{\partial t} + J(\psi, q) + \beta \frac{\partial \psi}{\partial x} = F - C_D \left[\frac{\partial (|\mathbf{u}| v)}{\partial x} - \frac{\partial (|\mathbf{u}| u)}{\partial y} \right] \tag{2.1}$$

where $q = \nabla^2\psi$ is the vorticity, ψ is the stream function, $J(\psi, q) \equiv \partial_x\psi\partial_y q - \partial_y\psi\partial_x q$ is the Jacobian operator, β is the background vorticity gradient, F is a small scale forcing that crudely represents the generation of eddies by baroclinic instability, C_D is a quadratic drag coefficient, and $\mathbf{u} \equiv (u,\ v) = (-\partial_y\psi,\ \partial_x\psi)$ is the velocity. A spectral filter (not explicitly included in Eq. (2.1)) removes enstrophy near the grid scale (see Appendix 2.A).

To study turbulent mixing, we consider a passive tracer advected by the turbulent flow, which stirs up a constant meridional gradient g:

$$\frac{\partial c}{\partial t} + J(\psi, c) + g\frac{\partial \psi}{\partial x} = 0 \tag{2.2}$$

where c is tracer concentration. Grid-scale variance is again removed using the same spectral filter as for vorticity. The eddy diffusivity D is computed as

$$D = -\frac{\overline{\langle v'c'\rangle}}{g} \tag{2.3}$$

where the overbar denotes a time mean and angle brackets indicate a domain average.

The numerical model used to solve Eqs. (2.1)(2.2) uses a pseudo-spectral barotropic solver in a doubly-periodic domain with a real space resolution of 512 by 512 grid points. The forcing is located at total wavenumber 140 or 80 (differing between simulations), and is formulated as a Markovian forcing, following Maltrud and Vallis (1991). Details of forcing, filter, and integral scheme are documented in Appendix 2.A. The model is integrated from a state of rest until a statistical equilibrium is reached. The quantities β, C_D, and the forcing amplitude are varied across a wide range of experiments.

2.3 General results and scaling arguments

In this section we discuss scaling arguments for the eddy diffusivity based on classical β-plane turbulence theory. We first discuss the qualitative role of β in affecting the inverse energy cas-

cade and turbulent mixing. Then the scaling relations for mixing length and eddy velocity are introduced, which finally provide estimates for the eddy diffusivity based on classical mixing length theory.

The characteristic scales for quantities appearing in Eq. (2.1) are

$$|\mathbf{u}| \sim u \sim v \sim U,\ x \sim y \sim L,\ q \sim \frac{U}{L},\ \psi \sim UL,\ F\psi \sim \epsilon \tag{2.4}$$

where the last term ϵ is the energy generation rate which describes how fast KE is created by F. Ignoring the size of the domain, and the forcing scale, the only external parameters in this system are C_D, β, and ϵ. Noting that we have two independent dimensions (length and time). Buckingham π theorem implies the existence of one non-dimensional number, which we call μ:

$$\mu \equiv \epsilon^{-1/5}\beta^{3/5}C_D^{-1}. \tag{2.5}$$

μ describes the importance of β relative to C_D and is the only factor controlling the transition between different regimes. We shall point out that we have carefully chosen the range of parameters in our simulations such that the energy containing scale and mixing length are significantly larger than the forcing scale, but smaller than the domain size, such that neither should interfere much with the scaling expressions achieved hereafter.

2.3.1 General results

We start by looking at three typical simulations from the three regimes discussed in the introduction (Fig. 2.1). The three rows in Fig. 2.1 show simulations with $\mu = 14.3,\ 98.8$, and 782.9, which puts them into the friction, transitional, and β regime, respectively. In addition to kinetic energy, we show spectra of eddy diffusivity, defined as the ratio of the eddy tracer

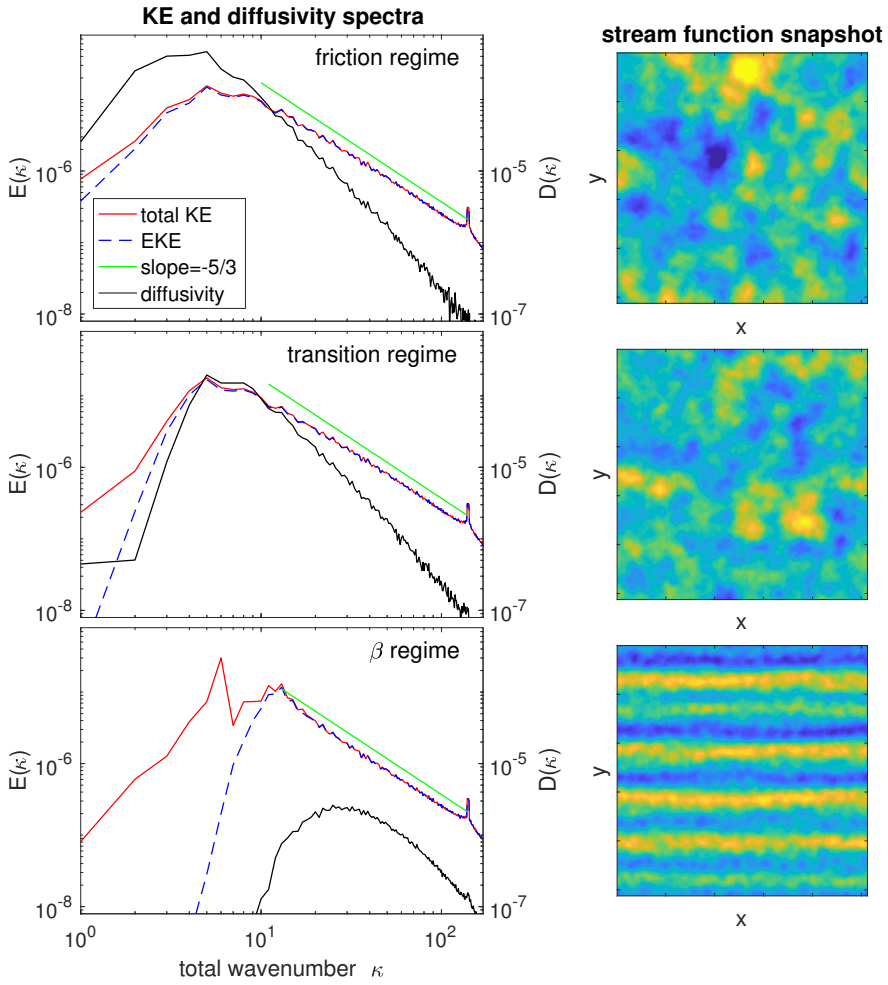

Figure 2.1: (left panel): total and eddy kinetic energy spectra and eddy diffusivity spectrum as functions of total wavenumber κ in 3 simulations, with the same ϵ and C_D but varied β; (right panel): snapshots of stream function in the 3 corresponding simulations, where yellow and blue color denotes positive and negative values, respectively.

flux cross spectrum to the background mean gradient of the passive tracer, g:

$$D(\kappa) \equiv \sum_{k^2+l^2=\kappa^2} D(k,l), \text{ where } D(k,l) = -\frac{\mathrm{Re}\left(\overline{\hat{v}_{k,l} \cdot \hat{c}^*_{k,l}}\right)}{g}. \tag{2.6}$$

The hat denotes Fourier transforms, * denotes the complex conjugate, and (k,l,κ) are zonal, meridional, and total wavenumbers, respectively. The summation amounts to a (discretized) integration in wavenumber space along circles with fixed total wavenumber. The diffusivity spectrum shows at which scale most of the mixing happens. The right panels show snapshots

of the streamfunction, illustrating how (an)isotropic the flow is.

Fig. 2.1 contains rich information about the flow and mixing behavior in each regime. The flow in the upper panel is in the friction regime so the energy spectrum is similar to f-plane turbulence, with a relatively smooth energy peak and nearly complete overlap between EKE and total KE, as the flow is highly isotropic (see also right panels). The mixing length is larger than the energy containing scale by roughly a factor of 2, due to the dependence of diffusivity on the KE spectrum and on the wavenumber itself. Classical mixing length theory suggests that the diffusivity spectrum can be estimated as

$$D_{\mathrm{ml}}(\kappa) \sim \frac{E(\kappa)}{\gamma} \sim \frac{E(\kappa)}{E(\kappa)^{1/2}\kappa^{3/2}} = E(\kappa)^{1/2}\kappa^{-3/2} \tag{2.7}$$

where γ is the eddy turnover rate and the subscript "ml" stands for "mixing length" theory. Eq. (2.7) shows that a shift of the peak in the eddy diffusivity spectrum, as compared to the EKE spectrum, results directly from the inverse wavenumber dependency of the eddy diffusivity (given a smooth peak in the spectrum). A more quantitative test and modification of this argument will be discussed in section 2.4.

As μ increases, the flow enters the transition regime (middle panel). In this case β starts to suppress mixing, as reflected by the reduction in the eddy diffusivity at large scales. Nevertheless, EKE remains the primary component of total KE, as can be seen from the similarity between the EKE and total KE spectrum in the left panel; as well as by noting that the flow field shown in the right panel remains largely isotropic.

Finally, in the β regime, the flow properties change significantly due to the dominant importance of β. The EKE spectrum significantly deviates from the total KE spectrum near the energy containing scale and at larger scales, reflecting the channeling of energy into zonal jets. This is also illustrated by the stream function snapshot shown in the right panel, which clearly shows the alternating zonal jets. Moreover, the eddy diffusivity is substantially suppressed, due to the suppression of both EKE and mixing length. Notice that the location of the peak in

the diffusivity spectrum is now at smaller scales than the peak of the EKE spectrum, indicating that the energy containing scale and the mixing length can differ significantly.

2.3.2 *Regime-based diffusivity scaling expressions*

In this section, the scaling relations for eddy velocity, mixing length, and eddy diffusivity are presented using both physical and dimensional arguments. The results from the scaling relations are compared to the numerical simulations.

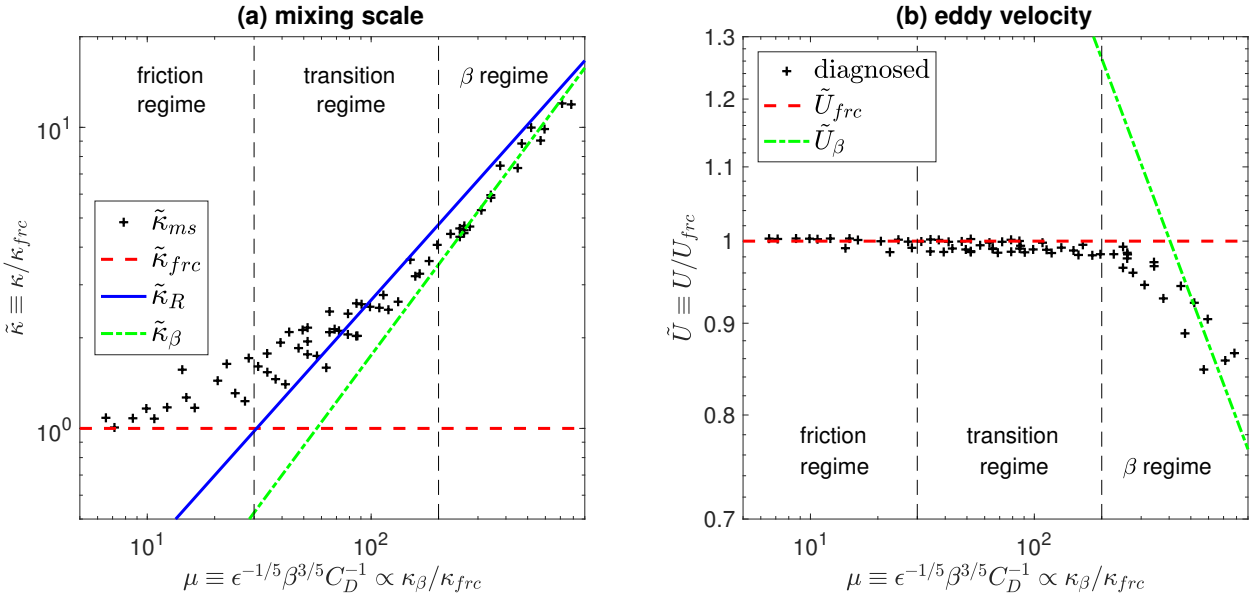

Figure 2.2: Testing the scaling expressions for the mixing length and characteristic eddy velocity (defined here as the domain-averaged root mean square eddy velocity). The non-dimensional mixing length (a) [2] and eddy velocity (b) are plotted as a function of the non-dimensional parameter μ. Various scaling relations are indicated with colored lines (see legend and text). Vertical black dashed lines indicate the boundaries between different regimes.

2. The mixing length is computed based on the inverse centroid of the diagnosed diffusivity spectrum, which is a better representation of the mixing length than the centroid of the diffusivity spectrum:

$$\kappa_{\mathrm{ml}} \equiv \frac{\int_0^\infty D(\kappa)\mathrm{d}\kappa}{\int_0^\infty \frac{D(\kappa)}{\kappa}\mathrm{d}\kappa}$$

Friction regime

The strong friction regime emerges at small μ, where β can be neglected, and the flow essentially behaves like f-plane turbulence. In this case, the mixing length is expected to scale with the energy containing scale (although it is typically slightly larger), which in turn is given directly by the quadratic drag coefficient C_D, as documented in Grianik et al. (2004):

$$L \sim \frac{1}{C_D},\ \kappa_{\text{frc}} \sim \frac{1}{L} \sim C_D \tag{2.8}$$

where L is the mixing length and κ_{frc} is the corresponding wavenumber, which will be called the frictional wavenumber.

κ_{frc} is shown in Panel (a) of Fig. 2.2, which compares the diagnosed mixing length with various scales from the scaling arguments. The frictional wavenumber successfully captures the mixing length at the smallest value of μ but tends to overestimate the mixing length as μ increases.

The characteristic eddy velocity is determined based on the EKE budget, which in the friction regime is well approximated by the total KE budget. The KE budget can be derived by multiplying Eq. (2.1) by $-\psi$ and integrating over the whole domain:

$$\frac{\partial \text{EKE}}{\partial t} \approx \frac{\partial \text{KE}}{\partial t} = -\int \psi \frac{\partial q}{\partial t} \text{dA} = -\int \psi F \,\text{dA} + C_D \int \psi \left[\frac{\partial (|\mathbf{u}|v)}{\partial x} - \frac{\partial (|\mathbf{u}|u)}{\partial y} \right] \text{dA}. \tag{2.9}$$

In steady state, the time derivative term in Eq. (2.9) drops out, and using Eq. (2.4) we find a scaling relationship between the rate of energy input, the bottom drag, and the eddy velocity as

$$U_{\text{frc}} \sim (\frac{\epsilon}{C_D})^{1/3}, \tag{2.10}$$

which is shown in Fig. 2.2(b). U_{frc} provides an accurate prediction of eddy velocity. Combing Eqs. (2.8) and (2.10), we recover the scaling expression for the eddy diffusivity in the friction

regime by Grianik et al. (2004):

$$D_{\text{frc}} \sim \frac{U_{\text{frc}}}{\kappa_{\text{frc}}} = \frac{\epsilon^{1/3}}{C_D^{4/3}}. \tag{2.11}$$

Notice that Eq. (2.11) can also be derived based on purely dimensional analysis: since β is assumed to be negligible in the friction regime, it shall not appear in the scaling for the eddy diffusivity, in which case the only dimensionally feasible way to express D_{frc} is Eq. (2.11).

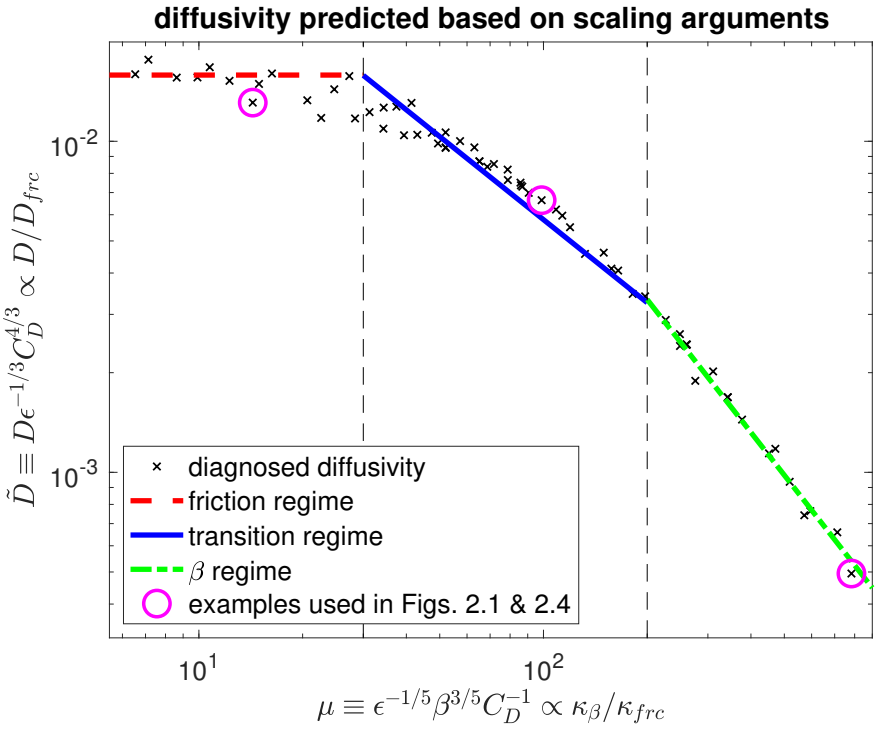

Figure 2.3: Diagnosed and predicted eddy diffusivity based on scaling arguments. x axis is the non-dimensional parameter μ, y axis shows the non-dimensionalized eddy diffusivity. Black crosses are the diagnosed diffusivity from numerical simulations; colored lines denote the predicted eddy diffusivity for the three regimes; vertical black dashed lines denote the boundaries between different regimes.

The scaling predicted by Eq. (2.11) is shown in Fig. 2.3, where eddy diffusivities have been non-dimensionalized using C_D and ϵ. The non-dimensional expression for the predicted eddy diffusivity in the friction regime then becomes

$$\tilde{D}_{\text{frc}} \sim 1 = \mu^0 \tag{2.12}$$

which captures the distribution of the eddy diffusivity in the friction regime reasonably well. A slight overestimation of the diffusivity near the right boundary of the friction regime arises from the overestimate of the mixing length as shown in Panel (a) of Fig. 2.2. Also notice that the non-dimensional parameter, μ, captures most, but not all of the spread among different simulations. The remaining spread between simulations is likely explained by the role of the forcing scale and domain size, whose relevance cannot be completely eliminated due to numerical constraints on the resolution and domain size.

β regime

If μ is very large, the flow enters the strong β regime. While friction necessarily remains important to dissipate energy, it has been argued that the bulk of the dissipation occurs in zonal jets, while the properties of the turbulent eddy field become independent of friction(Vallis and Maltrud, 1993). If C_D shall not appear in the scaling expression, the only dimensionally feasible way to express the mixing length is

$$L \sim \epsilon^{1/5}\beta^{-3/5},\ \kappa_\beta \sim \frac{1}{L} \sim \epsilon^{-1/5}\beta^{3/5}, \tag{2.13}$$

which is called the β scale. κ_β is generally interpreted as the crossover scale between isotropic and anisotropic (wave-)turbulence. For scales smaller than the β scale, the β effect remains negligible and the flow is isotropic. For scales larger than the β scale, however, the timescale of Rossby waves becomes shorter than the eddy turnover timescale, leading to anisotropic flows, where wave-like disturbances co-exist with zonal jets (e.g. Vallis and Maltrud, 1993; Smith et al., 2002; Vasavada and Showman, 2005).

The idea that the β scale provides the mixing length in β-plane turbulence is well documented and tested in previous studies (Vallis and Maltrud, 1993; Smith et al., 2002), although previous work assumed a linear rather than a quadratic drag. If eddy properties indeed become independent of friction, we may expect the results to apply similarly in the case of quadratic

drag, which is confirmed by our simulations. κ_β is shown in Panel(a) of Fig. 2.2, which provides an accurate prediction for the mixing length in the β regime.

The characteristic eddy velocity at the β scale can be determined from the Kolmogorov -5/3 spectrum (hereafter "Kolmogorov spectrum") which applies in the inertial range of isotropic turbulence and thus at scales up to κ_β:

$$E(\kappa) = K\epsilon^{2/3}\kappa^{-5/3} \tag{2.14}$$

where $K = 8$ is the non-dimensional Kolmogorov constant. U_β can therefore be estimated as

$$U_\beta \sim \sqrt{E(\kappa_\beta)\kappa_\beta} \sim \epsilon^{2/5}\beta^{-1/5}. \tag{2.15}$$

Notice that U_β is not necessarily the velocity corresponding to the full EKE; but rather, it is the characteristic velocity at the β scale, where energy is thought to be converted into both waves (that don't contribute to mixing, but do contribute to EKE) and jets (that don't contribute to either mixing or EKE). Nevertheless, Eq. (2.15) qualitatively predicts the reduction of EKE at large β (as shown by the dash-dot green line in Panel (b) of Fig. 2.2).

Combining Eqs. (2.13) and (2.15), we obtain a relationship for the eddy diffusivity as:

$$D_\beta \sim \frac{U_\beta}{\kappa_\beta} = \frac{\epsilon^{3/5}}{\beta^{4/5}}. \tag{2.16}$$

Again, Eq. (2.16) can also be retrieved directly from dimensional analysis by assuming that C_D does not appear in D_β, but the derivation presented above highlights that the suppression of eddy diffusivity in the β regime arises from the role of β in suppressing both the mixing length and turbulent EKE.

Using the non-dimensional formulation, D_β becomes:

$$\tilde{D}_\beta \sim \epsilon^{4/15}\beta^{-4/5}C_D^{4/3} = \mu^{-4/3}, \tag{2.17}$$

which successfully captures the distribution of the eddy diffusivity (green dash-dot line in Fig. 2.3).

Notice that our non-dimensional parameter, μ, can be related to the friction and β scale as

$$\mu \equiv \epsilon^{-1/5} \beta^{3/5} C_D^{-1} \sim \frac{\kappa_\beta}{\kappa_{\text{frc}}} \tag{2.18}$$

which makes its physical meaning clearer: while a small μ suggests the energy cascade is arrested at κ_{frc}, a large μ indicates the termination of the isotropic cascade at κ_β.

Transition regime

The most realistic scenario for Earth's ocean is one where both friction and β are important - a transition regime between the strong β and strong friction limits. Analyzing idealized simulations of baroclinic turbulence in a parameter regime thought to be crudely representative of the Southern Ocean, Jansen et al. (2015) find that the mixing length is well approximated by the Rhines scale:

$$\kappa_R \sim \sqrt{\frac{\beta}{U}} \approx \sqrt{\frac{\beta}{U_{\text{frc}}}}, \tag{2.19}$$

while the EKE remains controlled by bottom friction, similar to the friction regime. The notion that EKE remains controlled by bottom friction throughout most of the transition regime is supported by the results in Panel(b) of Fig. 2.2, which shows that the diagnosed eddy velocity is well approximated by U_{frc} throughout most of the transition regime. κ_R is also displayed in Panel(a) of Fig. 2.2, and indeed appears to be a reasonable estimate for the mixing length in the transition regime - although it's not a perfect fit everywhere.

Combining Eqs. (2.10) for the EKE and Eq. (2.19) for the mixing length yields

$$D_{\text{tr}} \sim \frac{U_{\text{frc}}}{\kappa_R} = \frac{\epsilon^{1/2}}{\beta^{1/2} C_D^{1/2}}. \tag{2.20}$$

Notice that in this formulation β only suppresses mixing by decreasing the mixing length, and

the suppression is more moderate compared to the β regime.

The non-dimensional form of D_{tr} is again shown in Fig. 2.3:

$$\tilde{D}_{\text{tr}} \sim \epsilon^{1/6}\beta^{-1/2}C_D^{5/6} = \mu^{-5/6}. \tag{2.21}$$

Eq. (2.21) captures the first order distribution of the eddy diffusivity in the transition regime. Nevertheless, notice that the eddy diffusivity in the transition regime is actually smoothly distributed along a curve, rather than following a straight line, indicating the limitations of using a single power-law scaling relation to represent the eddy diffusivity in this regime.

2.4 A generalized theory for the eddy diffusivity

The scaling arguments above are useful but not perfect, as they fail to capture the smooth transition of diffusivity between regimes, thus relying on a somewhat arbitrary specification of regime boundaries. The scaling argument is particularly unsatisfying in the (oceanographically relevant) transition regime where the eddy diffusivity does not follow a power law (Fig. 2.3). This motivates us to develop a more general expression for the diffusivity, which captures the behavior across all regimes.

In this section we adopt the linearization method in FN10 to derive a generalized expression for the eddy diffusivity in barotropic turbulence and compare it with the scaling arguments discussed above. In addition to providing a generalized expression for the eddy diffusivity, the result helps to reconcile the propagation-suppression argument of FN10 with the classical scaling arguments for the eddy diffusivity in the frictional and β regimes.

2.4.1 A stochastic model for non-linear eddy-eddy interactions

In FN10 the authors obtain an analytical solution for eddy diffusivity in a surface quasi-geostrophic model for a single wavenumber, which is interpreted as the energy containing scale. Their method is to linearize the non-linear eddy-eddy interaction as a combination of a stochastic

white noise forcing and a linear damping process. Here we want to use this parameterization not only for a single wavenumber but at every wavenumber pair (k, l). In spectral space, the Jacobian term thus becomes

$$\hat{J}(\psi,\ q) \equiv -Q\sqrt{\gamma}\ r_1(t) + \gamma\hat{q}. \tag{2.22}$$

The hat denotes the Fourier transform, Q is the amplitude of the stochastic forcing and has the same dimensions as $\hat{q}$, γ is the linear damping rate that describes how fast eddies decorrelate with itself, and $r_1(t)$ is the white noise process. Q and γ in general can also be functions of k and l. Physically, the forcing term represents how enstrophy is transferred into the respective wavenumber by non-linear eddy-eddy interactions, while the damping represents transfer to other wavenumbers.

Similarly, we will parameterize the Jacobian term in Eq. (2.2) as

$$\hat{J}(\psi, c) = -C\sqrt{\eta}\cdot r_2(t) + \eta\hat{c} \tag{2.23}$$

where C is the forcing amplitude, η is the tracer's linear damping rate, and $r_2(t)$ is again a white noise process assumed to be independent of $r_1(t)$. η may or may not be the same as γ. Notice that FN10 does not consider forcing and damping in the tracer equation, arguably consistent with the assumption that stirring is dominated by a single most energetic wave.

With these parameterizations, Eqs. (2.1) and (2.2) can be formulated in spectral space as

$$\frac{\partial\hat{q}}{\partial t} + ik\beta\hat{\psi} = Q\sqrt{\gamma}r_1(t) - \gamma\hat{q} \tag{2.24}$$

$$\frac{\partial\hat{c}}{\partial t} + ikg\hat{\psi} = C\sqrt{\eta}\cdot r_2(t) - \eta\hat{c}. \tag{2.25}$$

The forcing term $\hat{F}$ that appears originally on the right hand side of Eq. (2.24) has been dropped as we are here only interested in scales larger than the forcing scale. The quadratic drag term is also ignored because its amplitude turns out to be negligible at scales near or smaller than

the mixing length.

Solving Eq. (2.24) yields the streamfunction (see also Appendix 2.B):

$$\hat{\psi}(t) = -\frac{Q\sqrt{\gamma}}{\kappa^2}\int_0^\infty r_1(t-t_1)\exp[(\frac{ik\beta}{\kappa^2}-\gamma)t_1]\mathrm{d}t_1. \tag{2.26}$$

The EKE at wavenumber (k,l) can then be computed as (see Appendix 2.C)

$$E(k,l) = \frac{1}{2}\overline{|\kappa\hat{\psi}|^2} = \frac{Q^2}{4\kappa^2}. \tag{2.27}$$

Using Eqs. (2.2) and (2.26) we can solve for the tracer concentration:

$$\begin{aligned}\hat{c}(t) &= C\int_0^\infty r_2(t-t_2)\mathrm{e}^{-\eta t_2}\mathrm{d}t_2 \\ &\quad + \frac{ikgQ\sqrt{\gamma}}{\kappa^2}\int_0^\infty\int_0^\infty r_1(t-t_3-t_4)\exp\left[(\frac{ik\beta}{\kappa^2}-\gamma)t_4-\eta t_3\right]\mathrm{d}t_3\mathrm{d}t_4\end{aligned} \tag{2.28}$$

Together with Eq. (2.26), the mean meridional eddy tracer flux at wavenumber (k,l) can be computed as (see Appendix 2.C)

$$\mathrm{Re}\left(\overline{\hat{v}\cdot\hat{c}^*}\right) = -\frac{k^2Q^2g}{2\kappa^4}\cdot\frac{(\gamma+\eta)}{(\gamma+\eta)^2+\frac{k^2\beta^2}{\kappa^4}}. \tag{2.29}$$

Consequently, the eddy diffusivity spectrum at wavenumber (k,l) can be written as

$$D_{k,l} \equiv -\frac{\mathrm{Re}\left(\overline{\hat{v}\cdot\hat{c}^*}\right)}{g} = \frac{2k^2}{\kappa^2}\cdot\frac{1}{1+\frac{k^2\beta^2}{\kappa^4}\cdot\frac{1}{(\gamma+\eta)^2}}\cdot\frac{E(k,l)}{\gamma+\eta} \tag{2.30}$$

which is similar to Eq.(12) in FN10, except that: 1) β^2/κ^4 is the barotropic analog to $[c_w - U(z)]^2$ in FN10; 2) the damping rate γ in FN10 is replaced by $\gamma+\eta$; 3) Eq. (2.30) is here taken to represent the entire diffusivity spectrum, as opposed to just a single wavenumber; and 4) the factor 2 is missing in FN10 (which we believe is due to a mistake).

The last term on the right hand side, $D_{\mathrm{ml}}(k,l) \equiv E(k,l)/(\gamma+\eta)$, gives the scaling for the

eddy diffusivity spectrum based on mixing length theory. The first term, $2k^2/\kappa^2$, accounts for the anisotropy of turbulence. The suppression is given by the middle term, which modifies $D_{\mathrm{ml}}(k,l)$ in the presence of β via the ratio of the intrinsic Rossby wave frequency $\omega = k\beta/\kappa^2$ to the sum of the two damping rates, $\gamma + \eta$. Eq. (2.30) shows that eddy phase propagation relative to the mean flow (which controls the wave frequency) will suppress the diffusivity, as pointed out in FN10.

In its present form, Eq. (2.30) requires knowledge of the full two-dimensional EKE spectrum, which makes it not very useful for practical purposes. As a first step to simplify the expression to a more useful relationship, we want to reduce it to an equation for the one-dimensional diffusivity spectrum $D(\kappa)$:

$$D(\kappa) = \frac{1}{1 + \frac{\beta^2}{2\kappa^2(\gamma+\eta)^2}} \cdot \frac{E(\kappa)}{\gamma + \eta} \tag{2.31}$$

where we have made the simplifying substitution that $k^2/\kappa^2 = 1/2$, following FN10. This formally implies the assumption that the EKE is located along the diagonals with $|k| = |l|$ in wavenumber space, which is not realistic. A more realistic assumption would be to assume that the EKE is isotropic in wavenumber space, a case that has been discussed by SY14. However, in practice we find that the difference between the solutions arising from the two assumptions is small. We therefore proceed with the assumption of FN10, which simplifies the algebra considerably.

2.4.2 Relating eddy diffusivity to the EKE spectrum

Following FN10, the eddy damping rate γ can be interpreted as the eddy turnover rate, which scales as

$$\gamma \sim E(\kappa)^{1/2}\kappa^{3/2}. \tag{2.32}$$

We will similarly assume that η scales with the eddy turnover rate, which allows us to

combine the two as

$$\gamma + \eta = c_1 E(\kappa)^{1/2} \kappa^{3/2} \tag{2.33}$$

where c_1 is a non-dimensional constant of proportionality. We here simply set $c_1 = 1$, which provides a reasonably good fit to the results of the numerical simulations. However, since this is not a priori clear, we will include the parameter c_1 in all following equations for generality.

Substituting Eq. (2.33) into Eq. (2.31) gives

$$D^d(\kappa) = \frac{1}{c_1} \cdot \frac{E(\kappa)^{1/2} \kappa^{-3/2}}{1 + \frac{\beta^2}{2c_1^2 E(\kappa)\kappa^5}}. \tag{2.34}$$

where the superscript d indicates that the *diagnosed* EKE spectrum, $E(\kappa)$, is used.

Fig. 2.4 shows $D^d(\kappa)$ for the same three simulations as previously discussed in Fig. 2.1. The generalized theory provides a useful prediction for the diffusivity spectrum, giving a considerably better fit than the unsuppressed mixing length scaling $D_{\mathrm{ml}}(\kappa)$. However, $D^d(\kappa)$ still overestimates the eddy diffusivity in the β regime, i.e. when μ is large.

The reasons for this overestimation remain unclear to the authors. The role of the anisotropy does not appear to explain the misfit: no significant improvement is found when using the equation for the full 2D diffusivity spectrum $D(k, l)$ with the diagnosed 2D EKE spectrum (not shown). Another potential candidate is the vorticity gradient associated with the jets. However, over the parameter regime considered here, this gradient remains relatively small compared to β, suggesting that this effect is unlikely to explain the observed discrepancy. Another possible cause for discrepancy lies in the spatial inhomogeneity. As pointed out by Nakamura (2008), significant variations in the meridional gradient of zonal mean vorticity can create large differences between the arithmetic and the harmonic meridional mean of the diffusivity, with the latter arguably being more relevant. However, this can here only explain up to about 20% of the difference between the diagnosed and predicted diffusivity, hence leaving it as a minor factor.

We speculate that one possible explanation for the misfit is that the eddy turnover rate γ

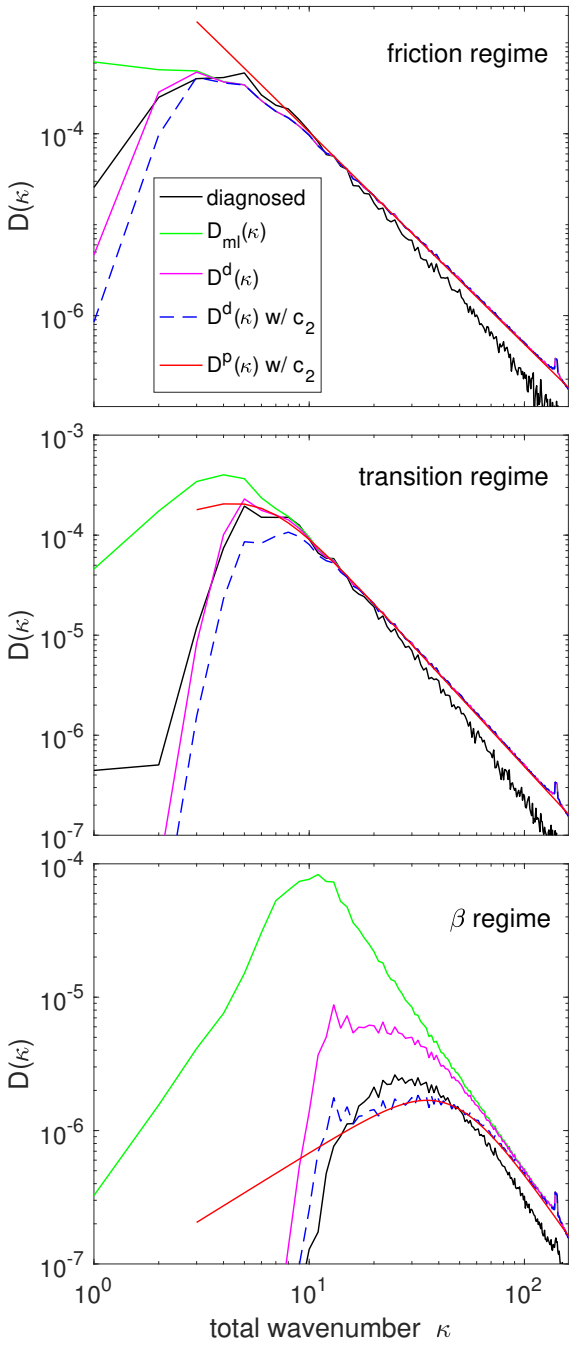

Figure 2.4: Diagnosed and predicted eddy diffusivity spectra for the same three simulations as in Fig. 2.1 (see legend and text for an explanation of the different theoretical spectra). Notice that the prediction $D^p(\kappa)$ assumes no energy (and thus no mixing) at wavenumbers below the frictional halting scale κ_{frc}.

itself needs to be altered as the eddies become more wave-like. Additionally, the meridional shear of the zonal velocity, created by the formation of jets, may suppress the eddy diffusivity

when μ is large: we find that the shear at the flanks of the jets is comparable to the eddy turnover rate γ (not shown). Unfortunately, we did not find a way to quantitatively incorporate these factors into our theory, without making the model overly complicated.. SY14 include the suppression of mixing by a constant background shear in their linearized model, but even with the simplifying assumption of a given constant background shear, the expressions become highly involved.

In practice, we find that an improved fit can be obtained by including an empirical fudge factor, $c_2 = 5.5$, in front of the β^2 term in Eq. (2.30), which is shown by the dashed curves in Fig. 2.4. Eq. (2.34) then becomes

$$D^{d\prime}(\kappa) = \frac{1}{c_1} \cdot \frac{E(\kappa)^{1/2}\kappa^{-3/2}}{1 + \frac{c_2\beta^2}{2c_1^2 E(\kappa)\kappa^5}}. \tag{2.35}$$

It is worth noting that FN10, albeit not explicitly discussing this issue, effectively include a similar factor to enhance the suppression effect in their equation (21). From footnote 2 in FN10 and the text below equation (17), one gets $d_2 = 4\alpha^2 d_1^2$ (using the definition of FN10). α here represents the ratio of the eddy phase speed to the surface current velocity. In the Southern Ocean we generally find $0 < \alpha < 1$, which leads to $d_2 < 4d_1^2$. However, combining their Eqs.(19) and (21) one retrieves $d_1 = 0.32$ and $d_2 = 4$, implying that d_2, which governs the strength of the suppression, is chosen much larger than what is suggested by the theory. The adopted values for d_1 and d_2 therefore reflect the same need to enhance the suppression effect, which in the current work is achieved by introducing the fudge factor c_2. Throughout the rest of this manuscript, we will include this fudge factor, but for readability we will drop the prime sign in the diffusivity.

For practical purposes, we may be more interested in the total "bulk" diffusivity, as opposed

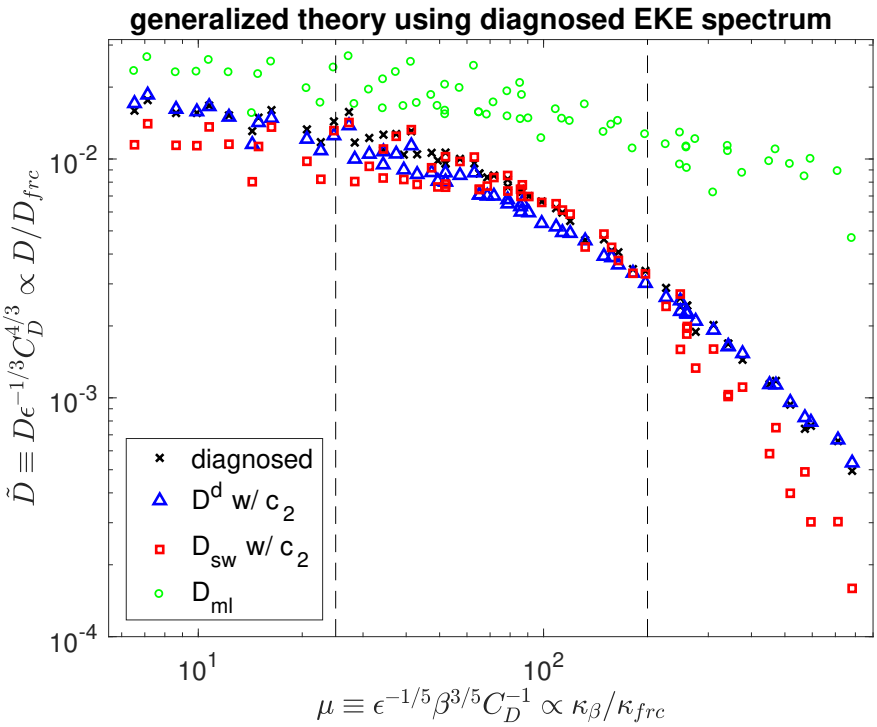

Figure 2.5: As Fig. 2.3, but showing the generalized theory for the eddy diffusivity using the diagnosed EKE spectrum (blue triangles), as well as the single wavenumber theory based on FN10 (red squares). The vertical black dashed lines are the same regime boundaries as in Figs. 2.2 & 2.3.

to the full diffusivity spectrum. The bulk diffusivity can be obtained by integrating Eq. (2.34)

$$D^d = \int_0^\infty D^d(\kappa)\mathrm{d}\kappa = \frac{1}{c_1}\int_0^\infty \frac{E(\kappa)^{1/2}\kappa^{-3/2}}{1+\frac{c_2\beta^2}{2c_1^2E(\kappa)\kappa^5}}\mathrm{d}\kappa, \tag{2.36}$$

which is compared against the numerical simulations in Fig. 2.5. D^d successfully reproduces the eddy diffusivity across all regimes, although it somewhat underestimates the diffusivity in the transition regime.

While providing a single bulk diffusivity, the prediction in Eq. (2.36) is based on the entire energy spectrum, which is the key aspect that distinguishes it from the approach of FN10 and KA14, who focus on a single wavenumber representing the scale of the most energetic eddies. To demonstrate the difference quantitatively, we compare our results to those obtained by

evaluating Eq. (2.30) for a single wavenumber taken as the diagnosed energy containing scale[3] κ_0. $E(\kappa)$ is taken to be the diagnosed EKE, and $\gamma = c_1\sqrt{\kappa^2 \mathrm{EKE}}$. Consistent with FN10 and KA14, we still assume $|k| = |l|$. Including again the fudge factor c_2 we obtain

$$D_{\mathrm{sw}} = \frac{\mathrm{EKE}}{\gamma + \frac{c_2\beta^2}{2\kappa^2\gamma}} = \frac{\mathrm{EKE}}{c_1\kappa\sqrt{\mathrm{EKE}} + \frac{c_2\beta^2}{2c_1\kappa^3\sqrt{\mathrm{EKE}}}} \tag{2.37}$$

where the subscript "sw" denotes the "single wavenumber" approximation. The results from Eq. (2.37) are shown in Fig. 2.5. The single wavenumber theory captures the distribution of the diffusivity in the friction and transition regimes reasonably well. However, D_{sw} significantly underestimates the diffusivity when μ gets large. This misfit can readily be understood by noting that mixing is no longer dominated by the energy containing scale at large μ (see e.g. the bottom row of Fig. 2.1). As the eddy diffusivity becomes strongly suppressed at the energy containing scale, smaller-scale eddies, which are ignored in the single wavenumber approximation, maintain the bulk of the mixing.

Fig. 2.5 may also explain some of the discrepancy between the theory and observations found in KA14. Fig. 2.6 in KA14 suggests that the theory accurately predicts the eddy diffusivity only in the Southern Ocean; at most other latitudes, the diffusivity is systematically underestimated. Meanwhile, FN10 only focus on a sector in the Southern Ocean. It is plausible that the Southern Ocean falls within a regime where the single wavenumber theory remains appropriate. In less energetic regions and at lower latitudes, μ instead may be larger, causing the single wavenumber theory to overestimate the mixing suppression.

3. κ_0 is computed based on the inverse centroid of the diagnosed EKE spectrum, similar to the way the mixing length is calculated (see footnote 1):

$$\kappa_0 \equiv \frac{\int_0^\infty E(\kappa)\mathrm{d}\kappa}{\int_0^\infty \frac{E(\kappa)}{\kappa}\mathrm{d}\kappa}$$

2.4.3 Towards a predictive theory

Despite its success, D^d is not able to predict the diffusivity without the knowledge of $E(\kappa)$. We seek to close this problem by assuming that $E(\kappa)$ can be approximated by the Kolmogorov spectrum [Eq. (2.14)] for $\kappa \gtrapprox \kappa_{\mathrm{frc}}$, while dropping rapidly to zero for $\kappa < \kappa_{\mathrm{frc}}$. Generally, we may not expect the Kolmogorov spectrum to extend all the way to κ_{frc} when β is large. However, since mixing at large scales is strongly suppressed in this limit, the results are expected to depend only weakly on the choice of the cut-off wavenumber. For the sake of simplicity we therefore refrain from introducing another halting scale for the energy spectrum. Combining Eqs. (2.14) and (2.34) we get:

$$D^p(\kappa) = \frac{\sqrt{K}}{c_1} \cdot \frac{\epsilon^{1/3}\kappa^{-7/3}}{1 + \frac{1}{2Kc_1^2} \cdot \frac{c_2\beta^2}{\epsilon^{2/3}\kappa^{10/3}}} \tag{2.38}$$

where the superscript p indicates the use of the *prognostic* relation for $E(\kappa)$. Eq. (2.38) is assumed to hold for $\kappa \gtrapprox \kappa_{\mathrm{frc}}$, while $D^p(\kappa) = 0$ is assumed for $\kappa < \kappa_{\mathrm{frc}}$.

$D^p(\kappa)$ is included in Fig. 2.4 where it is denoted by red curves. Generally speaking, it is able to capture the basic features of the diffusivity spectra, albeit with some caveats. First, D^p is unable to predict the detailed shape of the spectrum near the mixing length, which is unsurprising as the Kolmogorov spectrum is not applicable outside of the inertial range. Second, as μ becomes large, D^p is overestimated at scales larger than the mixing length. This "over-reaching" to large scales results directly from the use of the Kolmogorov spectrum all the way to κ_{frc}.

The bulk diffusivity can again be computed by integrating $D^p(\kappa)$:

$$D^p \approx \int_{\kappa_{\mathrm{frc}}}^{\infty} D^p(\kappa)\mathrm{d}\kappa = \frac{\sqrt{K}}{c_1} \int_{\kappa_{\mathrm{frc}}}^{\infty} \frac{\epsilon^{1/3}\kappa^{-7/3}}{1 + \frac{1}{2Kc_1^2} \cdot \frac{c_2\beta^2}{\epsilon^{2/3}\kappa^{10/3}}} \mathrm{d}\kappa. \tag{2.39}$$

The non-dimensional form of D^p plotted in Fig. 2.6 is:

$$\tilde{D}^p = \frac{\sqrt{K}}{c_1} \int_{c_0}^{\infty} \frac{\tilde{\kappa}^{-7/3}}{1 + \frac{c_2}{2Kc_1^2} \cdot (\frac{\mu}{\tilde{\kappa}})^{10/3}} \mathrm{d}\tilde{\kappa}, \tag{2.40}$$

where $c_0 \equiv \kappa_{\mathrm{frc}}/C_D$ and $\tilde{\kappa} \equiv \kappa \cdot C_D^{-1}$.

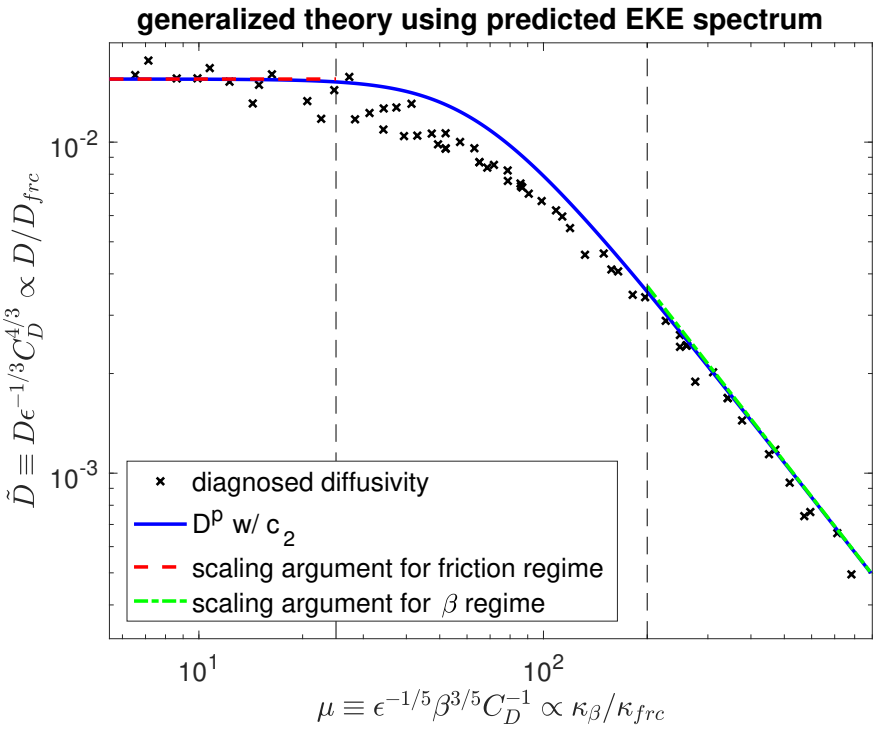

Figure 2.6: As Fig. 2.5 but showing the closed generalized theory using the Kolmogorov spectrum to predict the EKE spectrum. The scaling arguments for the friction and β regimes are also plotted in colored dashed lines.

$\tilde{D}^p$ is shown in Fig. 2.6 and successfully reproduces the smooth transition of the diffusivity across regimes. The diffusivity is slightly overestimated in the transition regime, which is contrary to the result in Fig. 2.5. The overestimate in the transition regime appears to be a result of the overestimate of the large-scale EKE by the Kolmogorov spectrum, and is thus not unexpected. One could attempt to include the effect of β in the formulation of the energy spectrum, but this would introduce at least one additional free parameter. Considering the overall success of Eq. (2.39), the benefit of such further complications is questionable.

2.5 Connecting the generalized theory to scaling arguments

In this section we will discuss the relationship between the generalized theory for the eddy diffusivity, discussed in section 2.4, and the scaling arguments discussed in section 2.3. In particular, it will be shown that the generalized theory reduces to the scaling arguments in the limits of strong friction and strong β.

In the friction limit, μ is small, so that the second term in the denominator of the integrand in Eq. (2.40) can be neglected, and we obtain the same scaling as Eq. (2.11)

$$\lim_{\mu\to 0} D \approx \frac{3\sqrt{K}}{4c_1 c_0^{4/3}} \cdot \frac{\epsilon^{1/3}}{C_D^{4/3}} \propto D_{\text{frc}}. \tag{2.41}$$

In this limit, the suppression has no effect, and the EKE spectrum (by assumption) peaks at κ_{frc}. As a result, the generalized theory reduces to the classical mixing length argument in this limit.

On the other hand, when μ is large, the scaling in the β regime is most easily retrieved by normalizing κ by κ_β, in which case Eq. (2.39) becomes

$$D^p = \frac{\sqrt{K}\epsilon^{3/5}}{c_1\beta^{4/5}} \int_{c_0/\mu}^{\infty} \frac{\mathrm{d}\mathring{\kappa}}{\mathring{\kappa}^{7/3} + \frac{c_2}{2Kc_1^2\mathring{\kappa}}}. \tag{2.42}$$

Taking the limit of large μ, we arrive at

$$\lim_{\mu\to\infty} D = \frac{\sqrt{K}\epsilon^{3/5}}{c_1\beta^{4/5}} \int_0^{\infty} \frac{\mathrm{d}\mathring{\kappa}}{\mathring{\kappa}^{7/3} + \frac{c_2}{2Kc_1^2\mathring{\kappa}}} \propto \frac{\epsilon^{3/5}}{\beta^{4/5}} \propto D_\beta. \tag{2.43}$$

The physical connection between the two theories can be seen by noting that the integrand of Eq. (2.43) (or the dimensional form in Eq. (2.39) for that matter) maximizes when the two terms in the denominator become equal, which yields

$$\mathring{\kappa} = \left(\frac{c_2}{2Kc_1^2}\right)^{3/10} \approx 0.73. \tag{2.44}$$

That is, the major contributions to the eddy diffusivity come from the eddies near the β scale, which is consistent with the classical mixing length theory. In fact, the physical reasoning is essentially the same, highlighting the importance of the wave-turbulence crossover wavenumber, below which the Rossby wave frequency exceeds the eddy turnover rate, thus rendering mixing inefficient.

The two limits have been included in Fig. 2.6 as the colored straight lines at both ends of the generalized theory. Taking the limits of the generalized theory therefore provides an alternative way to determine the non-dimensional constants in the scaling arguments for the friction and β regimes, relating them back to the Kolmogorov constant K, the non-dimensional factor c_0 in the frictional halting scale, the decorrelation constant c_1 (here taken to be 1), and (unfortunately) our fudge factor c_2. The connection between the generalized theory and the scaling argument in the transition regime instead is not obvious, as the generalized theory predicts a smooth transition from the friction to the β limit, rather than an independent intermediate power law regime.

2.6 Conclusions

This work sets out to investigate the eddy diffusivity in barotropic turbulence on a β-plane with quadratic drag. Specifically, we use a series of numerical simulations to test previously proposed scaling arguments for the eddy diffusivity in the friction regime, in the β regime, and in the transition regime. We then develop a generalized theory for the eddy diffusivity based on the propagation-suppression argument proposed by FN10. Finally, we show that the scaling arguments and the generalized theory are connected in the two limits of strong friction and strong β.

The scaling theory, which for the first time is applied to β-plane turbulence with quadratic drag, identifies 3 regimes depending on the relative importance of C_D and β. The scaling relations for the characteristic eddy velocity, mixing length, and eddy diffusivity are formulated for each regime, with the last quantity given by mixing length theory. In the strong friction limit,

the role of β can be neglected, and the eddy velocity is determined from a balance between the forcing and the energy dissipation by quadratic drag, while the mixing length is set by the frictional halting scale. In the strong β limit, on the other hand, it is the drag that is not important such that both the turbulent eddy velocity and mixing length follow from dimensional arguments. In a transitional regime, both drag and β are important: the eddy velocity remains controlled by bottom drag, while the mixing length is reasonably well approximated by the Rhines scale. The scaling arguments are tested against diagnosed diffusivities from high-resolution eddy-resolving numerical simulations, and found to successfully predict the eddy diffusivity in the respective regimes.

The generalized theory is motivated by an argument about the suppression of mixing by flow-relative eddy propagation, proposed by FN10. Their approach is here extended to the full diffusivity spectrum. The integral of the diffusivity spectrum then yields a bulk diffusivity, which generally differs from the single-wavenumber theory proposed by FN10 who only applied the argument to the energy containing wavenumber. Assuming that the non-linear decorrelation timescale is identical to the eddy turnover timescale, and that the EKE spectrum can be approximated by the Kolmogorov spectrum, we obtain a prognostic equation for the eddy diffusivity that is verified against the numerical simulations, and adequately captures the smooth transition across all parameter regimes.

The generalized theory highlights the importance of considering the entire energy spectrum. At least in the context of barotropic turbulence, the single-wavenumber approximation used by FN10 and KA14 breaks down once the suppression becomes sufficiently strong, at which point mixing is no longer dominated by the energy-containing scale. An estimate of the suppressed diffusivity considering only the energy containing scale is then likely to overestimate the suppression effect and thus underestimate the eddy diffusivity.

This work helps to clarify the connection between classical scaling theories for β-plane turbulence and the recently proposed propagation-suppression argument. Classical β-plane turbulence theory shows that β will suppress the eddy diffusivity via decreasing turbulent

eddy velocity and mixing length. Turbulent EKE is reduced due to the channeling of energy into Rossby waves and zonal jets. Similarly, the mixing length is reduced by the transition from isotropic turbulence to waves and jets at the β scale. Since the inverse energy cascade nevertheless proceeds to larger scales, this transition leads to the divergence between the energy containing scale and mixing length. Meanwhile, the generalized diffusivity theory highlights the propagation of eddies relative to the mean flow as responsible for the suppression of the diffusivity. Noting that the flow-relative phase propagation is related to the intrinsic Rossby wave phase speed, it is readily seen that the flow-relative suppression argument similarly predicts strong suppression of eddy mixing at scales beyond the wave-turbulence crossover scale. Indeed, the generalized theory is shown to reduce to the classical diffusivity scalings in the strong friction and strong β limits.

The presented work can provide a foundation for the development of eddy parameterizations in numerical ocean models. We have shown that the mixing suppression formulation has the potential to predict eddy diffusivities over a wide range of parameters, as long as the entire energy spectrum is considered. To apply the closure to meso-scale eddy fluxes in Earth's ocean, we need to predict the energy spectrum, as well as the wave dispersion relationship, which is complicated by the effects of a baroclinic background flow and bottom topography (e.g. Rhines and Bretherton, 1973; Killworth and Blundell, 1999; Wang et al., 2016). However, it is evident that flow-relative propagation of waves and eddies strongly affects mixing in the ocean (e.g. KA14). Improvements in the representation of eddy transports in coarse resolution ocean circulation models will therefore rely crucially on an adequate incorporation of these propagation effects.

Appendix 2.A Details of the numerical model

The expression for the forcing term used in our numerical model in spectral space is

$$\hat{F}^{n+1} = c\hat{F}^{n} + A \cdot \mathrm{e}^{i\hat{\theta}^{n+1}} \sqrt{1-c^2} \tag{2.45}$$

where superscript n denotes the timestep, $c = 0.99$ is the correlation coefficient, A is the forcing amplitude and is varied from case to case, i is the imaginary unit, and $\hat{\theta}$ is a random phase, which is independent for each wavenumber and timestep. The forcing is centered at wavenumber 80 or 140 (differing between simulations), with the width of the "forcing window" being 4 wavenumbers, i.e. $\kappa_f - 2 \leq \sqrt{k^2+l^2} \leq \kappa_f + 2$. Notice that for the purpose of testing scaling relationships in this paper, the total inverse energy flux ϵ is diagnosed in the simulations based on the total frictional dissipation rate. Unlike the total energy generation rate, the frictional dissipation remains a good approximation of the inverse energy cascade flux, even when energy dissipation by the grid scale filter is non-negligible.

The time integration is performed using a 3rd-order Adams-Bashforth scheme:

$$\hat{q}^{n+1} = T\left[\hat{q}^{n} + \frac{\delta t}{12}(23\dot{\hat{q}}^{n} - 16\dot{\hat{q}}^{n-1} + 5\dot{\hat{q}}^{n-2})\right] \tag{2.46}$$

where δt is the timestep and dotted quantities are time derivatives at the corresponding timesteps.

The filter T removes enstrophy and tracer variance at small scales in Eqs. (2.1) and (2.2), respectively, and takes the form

$$T = \begin{cases} \exp[-b \cdot (\kappa - \kappa_c)^p] & \text{if } \kappa > \kappa_c, \\ 1 & \text{if } \kappa \leq \kappa_c. \end{cases} \tag{2.47}$$

where $\kappa = \sqrt{k^2+l^2}$ is the total wavenumber, $b = 18$ governs the strength of the damping,

$\kappa_c = 187$ is a cut-off wavenumber, and $p = 7$ governs the sharpness of the spectral filter. The model is not de-aliased as it was found that de-aliasing has no significant effect on our results.

Appendix 2.B Solving the linearized stochastic model

In this appendix we will sketch the derivation of Eqs. (2.26) and (2.28). In spectral space we have $\hat{q} = -\kappa^2\hat{\psi}$, therefore Eq. (2.26) becomes

$$\frac{\partial \hat{q}}{\partial t} + (-\frac{ik\beta}{\kappa^2} + \gamma)\hat{q} = Q\sqrt{\gamma}r_1(t). \tag{2.48}$$

Eq. (2.48) has the general form

$$\frac{\mathrm{d}P(t)}{\mathrm{dt}} + A \cdot P(t) = R(t) \tag{2.49}$$

which (assuming that the equation has been integrated long enough for the initial conditions to be "forgotten") has the solution

$$P(t) = \int_0^\infty R(t-\tau)\mathrm{e}^{-A\tau}\mathrm{d}\tau. \tag{2.50}$$

Plugging in the appropriate constants for A and B yields

$$\hat{q}(t) = Q\sqrt{\gamma}\int_0^\infty r_1(t-t_1)\exp[(\frac{ik\beta}{\kappa^2} - \gamma)t_1]\mathrm{dt}_1 \tag{2.51}$$

and we retrieve Eq. (2.26).

Substituting the result for $\hat{\psi}$ into Eq. (2.25) and rearranging yields

$$\frac{\partial \hat{c}}{\partial t} + \eta \cdot \hat{c} = C \cdot r_2(t) + \frac{ikgQ\sqrt{\kappa}}{\kappa^2}\int_0^\infty r_1(t-t_1)\exp\left[(\frac{ik\beta}{\kappa^2} - \gamma)t_1\right]\mathrm{dt}_1 \tag{2.52}$$

which again takes the form of Eq. (2.49). Using again the general solution in Eq. (2.50), we

get Eq. (2.28).

Appendix 2.C Computing EKE and eddy tracer flux

In this section we sketch the derivation of Eqs. (2.27) and (2.29). For EKE,

$$\begin{aligned} E(k,l) &= \frac{1}{2}\overline{|\kappa\hat{\psi}|^2} \\ &= \frac{Q^2\gamma}{2\kappa^2}\int_0^\infty\int_0^\infty \delta(t_1-t_2)\exp\left[(\frac{ik\beta}{\kappa^2}-\gamma)t_1-(\frac{ik\beta}{\kappa^2}+\gamma)t_2\right]\mathrm{d}t_1\mathrm{d}t_2 \\ &= \frac{Q^2}{4\kappa^2} \end{aligned} \tag{2.53}$$

where we have used that $\overline{r_1(t-t_1)\cdot r_1^*(t-t_2)} = \delta(t_1-t_2)$.

For the eddy tracer flux we have

$$\begin{aligned} \overline{\hat{v}\cdot\hat{c}^*} &= -\frac{k^2Q^2g\gamma}{\kappa^4}\int_0^\infty\int_0^\infty\int_0^\infty \delta(t_3+t_4-t_1) \\ &\quad \exp\left[(\frac{ik\beta}{\kappa^2}-\gamma)t_1-\eta t_3-(\frac{ik\beta}{\kappa^2}+\gamma)t_4\right]\mathrm{d}t_1\mathrm{d}t_3\mathrm{d}t_4 \\ &= -\frac{k^2Q^2g}{2\kappa^4}\cdot\frac{1}{-\frac{ik\beta}{\kappa^2}+\gamma+\eta} \end{aligned} \tag{2.54}$$

where we have used that $\overline{r_1(t-t_1)\cdot r_2^*(t-t_2)} = 0$ because $r_1(t)$ and $r_2(t)$ are assumed independent. The real part of Eq. (2.54) yields Eq. (2.29).

CHAPTER 3

THE IMPACT OF TOPOGRAPHY AND EDDY PARAMETERIZATION ON THE SIMULATED SOUTHERN OCEAN CIRCULATION RESPONSE TO CHANGES IN SURFACE WIND STRESS

3.1 Introduction

The Southern Ocean plays a crucial role in Earth's climate and global ocean dynamics. It connects major ocean basins through its Antarctic Circumpolar Current (ACC) and the associated meridional overturning circulation (MOC). Both of these components are fundamentally driven by surface wind stress, which has been increasing for decades and is projected to further increase in the future (e.g. Swart and Fyfe, 2012). An important question therefore is how the ACC and MOC respond to changes in surface wind stress.

Straub (1993) proposes that the baroclinic ACC transport may remain steady despite the changes in surface wind stress, due to the role of meso-scale eddies in adjusting the isopycnal structure, a scenario that has been called "eddy saturation". An increase in surface wind stress steepens the isopycnals, which increases the baroclinic ACC transport (following the thermal wind relation), builds up available potential energy, and enhances baroclinic instability. Consequently, meso-scale eddies strengthen and tend to flatten the isopycnals, which weakens the ACC transport response. In fact, the ACC transport has been argued to have changed little despite significant surface wind stress increase during the past decades (Böning et al., 2008).

Meso-scale eddies are also crucial in the maintenance of the Southern Ocean MOC by generating an eddy-induced MOC that flattens the isopycnals and counteracts the wind-driven MOC. Hallberg and Gnanadesikan (2006) propose that when wind stress increases, the eddy-induced MOC will adjust so as to compensate for the increase in the wind-driven MOC, resulting in an insensitive residual MOC, an effect that has been called "eddy compensation" (Viebahn and Eden, 2010).

The key ingredient to both the eddy saturation and compensation arguments are meso-scale eddies, which, due to their small size, have to be parameterized in most comprehensive general circulation models (GCMs). The effect of meso-scale eddies on the density field is typically parameterized via the Gent and McWilliams (1990) (hereafter: GM) parameterization, which induces an eddy-driven overturning proportional to the isopycnal slope times the GM "diffusivity". However, models differ significantly in their choices for the GM diffusivity, which can itself be a function of the mean flow. Previous studies have shown that the ACC and MOC response to wind stress changes in ocean and climate models is often sensitive to the choice of GM diffusivity (e.g. Farneti et al., 2010; Farneti and Gent, 2011; Kuhlbrodt et al., 2012; Farneti et al., 2015; Poulsen et al., 2018). Farneti et al. (2015) compare simulations of 1958-2007 climate across a number of ocean GCMs configured with different eddy parameterizations or at eddy-permitting resolutions, and find that the degree of eddy saturation is almost perfect in all models, while the degree of eddy compensation diverges significantly across the GCMs. Particularly, they find that the degree of eddy compensation tends to be higher in the models that either use an eddy-permitting resolution without eddy parameterizations, or adopt a 3D spatial structure for the GM diffusivity; by contrast, the degree of eddy compensation is lower in the models that employ only a 2D or 1D spatial structure for the GM diffusivity. Poulsen et al. (2018) compare the transient response of the MOC to wind stress changes in two configurations of the same GCM, one with fully resolved meso-scale eddies and the other with parameterized eddies. They find that the MOC in the two configurations responds similarly to decreased wind stress but significantly differently to increased wind stress. Complex GCM simulations hence tend to suggest that eddy compensation is more pronounced in high resolution simulations or those with sophisticated eddy parameterizations. However, the results are not always consistent and interpretation is challenging due to the general complexity of the models, the potential sensitivity on simulation time and initial conditions (Sinha and Abernathey, 2016; Jansen et al., 2018), and the fact that different models typically differ in many aspects other than their representation of meso-scale eddies.

Idealized models have therefore played an important role for both testing eddy parameterizations and improving mechanistic understanding (Hallberg and Gnanadesikan, 2006; Viebahn and Eden, 2010; Abernathey et al., 2011; Allison et al., 2011; Munday et al., 2013; Morrison and Hogg, 2013; Abernathey and Cessi, 2014; Nadeau and Ferrari, 2015; Mak et al., 2018; Constantinou, 2018; Constantinou and Hogg, 2019). Yet only a few studies have compared the degree of eddy saturation and/or compensation in non-eddying simulations with state-of-the-art eddy parameterizations, against an eddy-resolving simulation in the same model configuration. Mak et al. (2018) find almost perfect eddy saturation in an idealized eddy permitting model of the Southern Ocean. They show that coarse resolution simulations using their new GEOMETRIC parameterization can reproduce this result, while simulations with a constant GM diffusivity fail to adequately capture the eddy saturation. By contrast, their coarse resolution simulations using GEOMETRIC or a constant GM diffusivity can both produce a similar degree of eddy compensation as in the eddy-permitting simulation. Viebahn and Eden (2010) instead find that coarse resolution simulations with eddy parameterizations predict a lower degree of eddy compensation than an eddy-permitting simulation. One difference between the two studies is the topography: while both studies use a model that has a reentrant channel connected to a basin in the north, the channel region in Viebahn and Eden (2010) has a flat bottom, while the model of Mak et al. (2018) includes a meridional ridge in the channel area, which blocks bottom zonal flow and generates stationary meanders.

Topography plays a crucial role in modulating the Southern Ocean circulation. It creates local hotspots of eddy kinetic energy (EKE), which are collocated with flattened isopycnals (Thompson and Naveira Garabato, 2014). Topography has also been shown to suppress the response of the ACC transport to wind stress changes through enhancing local buoyancy gradients and elongating buoyancy contours across which the eddies transport buoyancy (Abernathey and Cessi, 2014). Emphasizing the importance of barotropic dynamics, Constantinou (2018) argues that, in the presence of topography, eddy saturation can even occur in the absence of baroclinic instability. Although the effect of topography on ACC transport has thus

received significant attention, the effect on the MOC, and especially eddy compensation, has not been systematically explored.

In this work we use an idealized model setup to investigate the influence of topography on both eddy saturation and compensation, and examine in how far these processes can be reproduced in coarse resolution simulations with state-of-the-art eddy parameterizations. We show that topography significantly amplifies the degree of both eddy compensation and saturation, leading to relatively insensitive MOC & ACC transport. Moreover, the ACC and MOC responses to wind stress changes are reasonably well captured by coarse resolution simulations with a range of different eddy parameterizations if, and only if, topography is present.

3.2 Model configuration

We perform our experiments using an isopycnal configuration of the GFDL Modular Ocean Model 6 (MOM6), with 30 isopycnal layers. We employ two different topographic configurations, shown in Fig. 3.1. Both configurations share the same domain size, spanning from 65°S to 30°S in latitude and covering 60° in longitude with periodic zonal boundary conditions. The longitudinal extent is chosen to minimize computational expense while still allowing for substantial stationary meanders associated with large topography. The flat bottom configuration (left panel) is a zonally reentrant channel, similar to the one used by Abernathey et al. (2011), but with a continental slope along Antarctica. The full topography configuration (right panel) has a meridional continental barrier (mimicking Patagonia) and a sub-surface ridge encircling Drake Passage (mimicking Scotia Arc). Drake Passage is the only reentrant part, which opens between 61°S to 53°S at the surface and becomes slightly narrower at depth. We have also included a topographic slope along the southern, eastern, and western boundaries, as well as along Scotia Arc. Away from the topographic features, the sea floor is 4km deep, and Scotia Arc rises to a depth of 2.5km.

We use two horizontal resolutions: 0.1° for the eddy-resolving simulations, and 1° for the non-eddying simulations where eddy parameterizations are used. The model adopts a

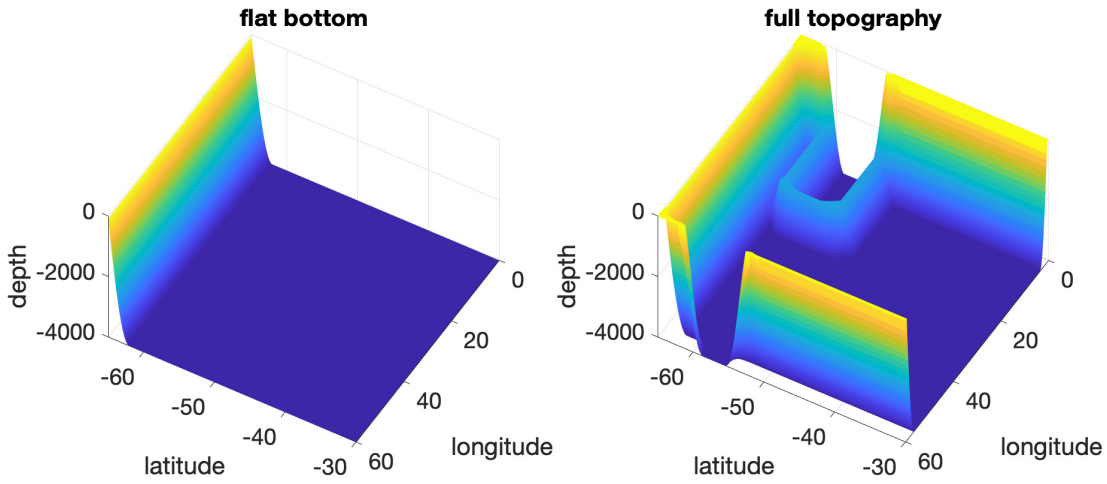

Figure 3.1: The two topography configurations used in this study. A no-flux condition is applied at the northern boundary. Where indicated, a 1° wide sponge layer is applied to restore the buoyancy profile at the northern end.

Mercator grid so its latitudinal grid spacing (in physical distance) roughly matches that of its longitudinal grid spacing. The aforementioned resolutions refer to the longitudinal increment. The latitudinal increment decreases poleward to maintain roughly square grid boxes.

The model is forced with zonally symmetric wind stress that peaks at 53°S and vanishes at the southern & northern boundaries (panel (a) of Fig. 3.2):

$$\tau(\theta) = \begin{cases} \tau_0 \cos[\frac{15}{2}(\theta + 53°)], & \theta \leq -53°; \\ \frac{1}{2}\tau_0 \left[1 + \cos(\frac{36}{5}(\theta + 53°))\right], & \theta > -53° \end{cases} \tag{3.1}$$

where θ is latitude, $\tau_0 = 0.2$ Pa is the peak wind stress in the reference case, and $\tau_0 = 0$ Pa, 0.05 Pa, 0.1 Pa, and 0.3 Pa in the wind stress sensitivity experiments.

The model's surface potential density is restored towards a target density profile (panel (b) of Fig. 3.2), with a piston velocity of 2m day^{-1}:

$$\sigma_2(\theta) = 1031.30 - 0.0954\theta\,. \tag{3.2}$$

We employ two types of buoyancy boundary conditions at the northern end of the domain to

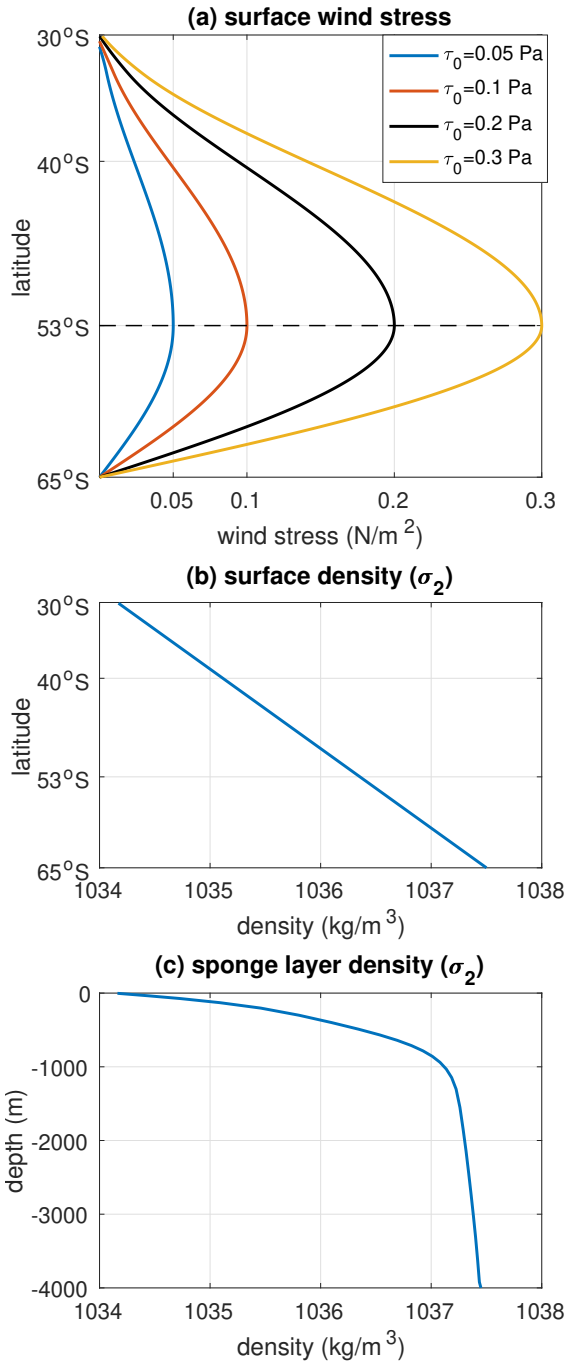

Figure 3.2: The model's boundary conditions. (a): Surface zonal wind stress profile; (b): the target surface potential density profile; (c): the target potential density profile towards which buoyancy is restored in the sponge layer (where applied - see text).

explore the responses of the MOC and ACC transport to wind stress changes. To investigate the response of the MOC, we use a "sponge layer" at the northern boundary, which represents the diabatic transformation of water masses taking place in the basin to the north of the Southern

Ocean in the real world (Abernathey et al., 2011; Morrison and Hogg, 2013). In the sponge layer, vertical stratification is restored towards a prescribed profile[1], shown in panel (c) of Fig. 3.2. The sponge layer is 1° wide latitudinally. The restoring rate is $(7\ \text{day})^{-1}$ at the very boundary and decreases linearly towards the southern edge of the sponge layer where it becomes 0. The sponge layer enables us to investigate the response of the MOC to changes in surface wind stress with the channel configuration because it allows for a non-trivial residual MOC. However, the sponge layer is not suitable to investigate the response of the ACC transport, because, together with the surface restoring condition, the two boundary conditions specify the baroclinicity in the channel to a level where there is very little room for the ACC transport to adjust. In other words, the sponge layer allows us to investigate the eddy compensation in a limit where eddy saturation is essentially enforced.

To investigate the response of the ACC transport, we adopt an adiabatic boundary condition (i.e. no sponge layer; as e.g. in Abernathey and Cessi, 2014). This allows isopycnals to freely evolve so that changes in the ACC transport in response to varying surface wind stress can be represented. By construction, this setup does not allow any non-trivial MOC to exist (except for that induced by diapycnal mixing within the Southern Ocean), and is therefore not suitable to investigate the MOC's response to wind stress changes. This setup can be used to explore eddy saturation in the limit of approximate eddy compensation. We summarize key model parameters in Table 3.2. All simulations have been integrated to a statistically steady state, for at least 250 model years.

1. This profile has been determined by running an extended version of the model (with full topography) which includes an inter-hemispheric basin with northern deep water formation to the north of the channel. This extended version of the model was run at 1° resolution with a simple eddy parameterization that has a constant GM diffusivity of $700\text{m}^2\ \text{s}^{-1}$. The detailed structure of the sponge layer does not alter the conclusions of this work.

Parameter	Value
Piston velocity for surface density restoring	2m day^{-1}
Maximum sponge layer restoring rate	(7 day)$^{-1}$
Biharmonic viscosity	0.05m s^{-1} $\times$ Δ^3 (Δ is grid spacing)
Diapycnal diffusivity	5×10^{-5}m^2 s^{-1}
Quadratic bottom drag coefficient	0.003

Table 3.1: Key model parameters

3.3 Eddy parameterizations

The eddy parameterizations we test in this work are all based on the GM framework (Gent and McWilliams, 1990; Gent et al., 1995). The GM framework parameterizes the eddy-induced streamfunction as

$$\psi_{\mathrm{GM}} = \mathbf{k} \times \kappa_{\mathrm{GM}} \mathbf{s} \tag{3.3}$$

where $\mathbf{k}$ is the vertical unit vector, κ_{GM} is the GM diffusivity, and $\mathbf{s} = \nabla_\sigma z$ is the isopycnal slope (the subscript σ denotes that the gradient is taken along an isopycnal; Vallis, 2006). The parameterized overturning circulation, ψ_{GM}, flattens the isopycnals that are tilted by the wind-driven Ekman transport, and hence releases available potential energy from the resolved flow. Notice that the GM parameterization represents the advective effect of eddies, which makes the interpretation of κ_{GM} as an eddy "diffusivity" questionable. However, for small isopycnal slopes (a good assumption outside of the mixed layer), κ_{GM} relates the horizontal component of the eddy buoyancy flux to the mean horizontal buoyancy gradient (e.g. Plumb and Ferrari, 2005). We therefore here adopt the common interpretation of κ_{GM} as a horizontal eddy buoyancy diffusivity, although we note that, in the ocean interior, a vertical eddy flux component that aligns the buoyancy flux along the isopycnal slope is implied.

The eddy parameterizations we test in this work vary only in their formulations of the GM diffusivity. The first suite of simulations use a constant GM diffusivity: 0, 100, 200, ..., 700 m^2 s^{-1}. The second eddy parameterization we test is based on Visbeck et al. (1997) and computes the GM diffusivity based on the local baroclinicity and stratification. The third

Acronym	Eddy parameterization
$\kappa_7, \kappa_6, ..., \kappa_0$	Constant GM diffusivity: 700, 600, ..., 0 ($m^2\ s^{-1}$)
Visbeck	Based on Visbeck et al. (1997)
MEKE	Meso-scale eddy kinetic energy (Jansen et al., 2015)
TMEKE	Topographic MEKE

Table 3.2: Acronyms for eddy parameterizations (see Appendix 3.A for a detailed description)

eddy parameterization is based on Jansen et al. (2015) and computes the GM diffusivity based on a prognostic equation for the meso-scale eddy kinetic energy (MEKE; see also Eden and Greatbatch, 2008). The last eddy parameterization is a modified version of the MEKE parameterization that considers the suppression of the GM diffusivity by the topographic β effect, and therefore is named TMEKE ("T" for topographic; see also Jansen et al., 2019). The GM diffusivity in the Visbeck, MEKE, and TMEKE eddy parameterizations varies temporaly and horizontally but not vertically. We have also tested vertically varying GM diffusivities, either through imposing an equivalent barotropic structure to the GM diffusivity, or by solving a vertical elliptic equation for the eddy-induced streamfunction (Ferrari et al., 2010). However, we have found that including a vertical structure in the eddy parameterization does not improve our results, and have thus not included it in the eddy parameterizations discussed in this paper. The acronyms for the various eddy parameterizations are listed in Table 3.3, and additional details are provided in Appendix 3.A.

3.4 Results

We compare different eddy parameterizations by running the same model configurations with two resolutions: a 0.1° eddy-resolving simulation, and several 1° non-eddying simulations with different eddy parameterizations. We first consider the reference setup, where we include the full topography and force the model with present-day wind stress ($\tau_0 = 0.2$ Pa), with and without the sponge layer at the northern boundary. The setup with the sponge layer is used to investigate the MOC, while the one without the sponge layer is used to investigate the

ACC transport. We then vary wind stress to test how the eddy parameterizations capture the response of the ACC transport and the MOC to wind stress changes under different topography and using different eddy parameterizations.

3.4.1 Performance of eddy parameterizations in the reference setup

In this part we test the eddy parameterizations' ability to reproduce high resolution simulations in the reference case with full topography and wind stress $\tau_0 = 0.2$ Pa. Three metrics are used to evaluate the eddy parameterizations: a) the baroclinic ACC transport in the simulations with an adiabatic northern boundary condition, b) the MOC in the simulations with a sponge layer at the northern boundary, and c) the isopycnal interface height error ε in both configurations. We find that the simulations using variable GM diffusivities generally better reproduce the ACC transport, the MOC, and the isopycnal height field of the high-resolution reference simulations, with the energy-budget based parameterization with topographic β effect (TMEKE) performing best overall.

Baroclinic ACC transport

We focus on the baroclinic component of the ACC transport, which is computed as the total zonally-averaged ACC transport minus the transport associated with the bottom geostrophic flow:

$$T_{\mathrm{ACC}} = \iint [\overline{u}_{\mathrm{bc}}]\mathrm{dydz} = \iint [\overline{u} + \frac{1}{f\rho_0}\partial_y \overline{p}(z_{\mathrm{bot}})]\mathrm{dydz}, \tag{3.4}$$

where $[\cdot]$ denotes a zonal average, $\overline{(\cdot)}$ denotes a temporal average (over 20 years in the 0.1° simulations and 50 years in the 1° simulations), u_{bc} is the baroclinic zonal velocity, u the full zonal velocity, f the Coriolis parameter, ρ_0 the reference density, and $\partial_y p(z_{\mathrm{bot}})$ is the hydrostatic pressure gradient at the sea floor (with the meridional derivative taken at fixed depth).

We find that the baroclinic ACC transport can be well reproduced in the coarse resolution

simulations with either a variable GM diffusivity or a constant GM diffusivity κ_{GM} ~400m^2 s^{-1}, as is shown in Fig. 3.3. When a constant GM diffusivity is adopted, the qualitative relation between the diffusivity and the ACC transport is as expected: because the GM diffusivity works to flatten the isopycnal slope, a larger GM diffusivity leads to smaller isopycnal slopes, which in turn results in a weaker baroclinic ACC transport.

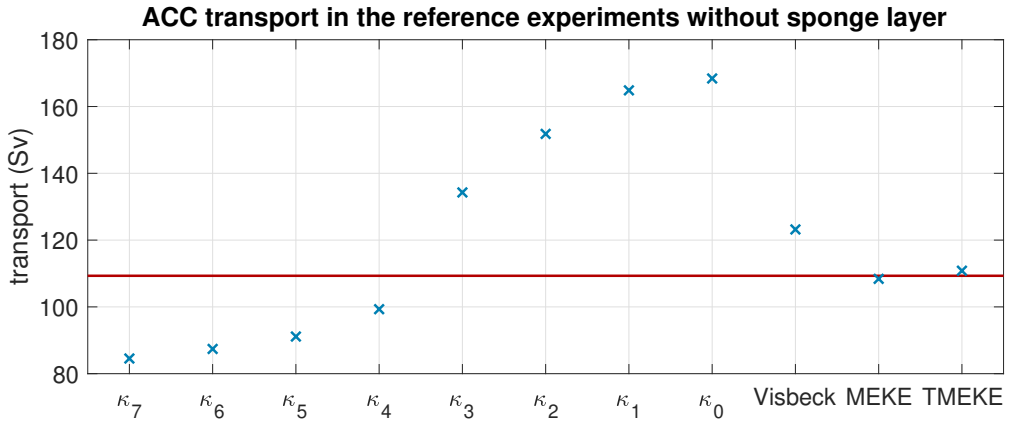

Figure 3.3: Baroclinic ACC transport using different eddy parameterizations in the reference experiments (full topography, $\tau_0 = 0.2$Pa) without northern sponge layer. The horizontal line denotes the ACC transport in the 0.1° simulation; blue crosses indicate the transport in the 1° simulations using the various eddy parameterizations denoted on the x-axis (c.f. table 3.3).

MOC

Next we compare the MOC across the simulations employing a northern sponge layer. The MOC in the 0.1° simulation is computed as

$$\psi(y,\sigma) = \oint_x \int_{\sigma_s}^{\sigma} \overline{v(x,y,\hat{\sigma}) \cdot h(x,y,\hat{\sigma})}\, \mathrm{d}\hat{\sigma}\mathrm{d}x. \tag{3.5}$$

where σ_s is the surface density and $h = -\partial z/\partial\sigma$ is the isopycnal layer thickness ($h = 0$ on isopycnals that vanish due to in- or out-cropping). In the 1° simulations the MOC is computed as

$$\psi(y,\sigma) = \oint_x \int_{\sigma_s}^{\sigma} \overline{v(x,y,\hat{\sigma}) \cdot h(x,y,\hat{\sigma}) + \mathrm{vh}_{\mathrm{GM}}(x,y,\hat{\sigma})}\, \mathrm{d}\hat{\sigma}\mathrm{d}x \tag{3.6}$$

where $\mathrm{vh_{GM}} = \partial \psi^y_{GM} / \partial \sigma$ is the parameterized eddy thickness flux. The magnitude of the upper MOC cell is defined as the maximum of ψ along the $\sigma = 1037\mathrm{kg\ m^{-3}}$ isopycnal, where the center of the upper cell resides in the high resolution simulation. The magnitude of the lower cell is defined as the minimum of ψ along the $\sigma = 1037.42\mathrm{kg\ m^{-3}}$ isopycnal. The main results in this work are insensitive to where exactly the MOC is evaluated.

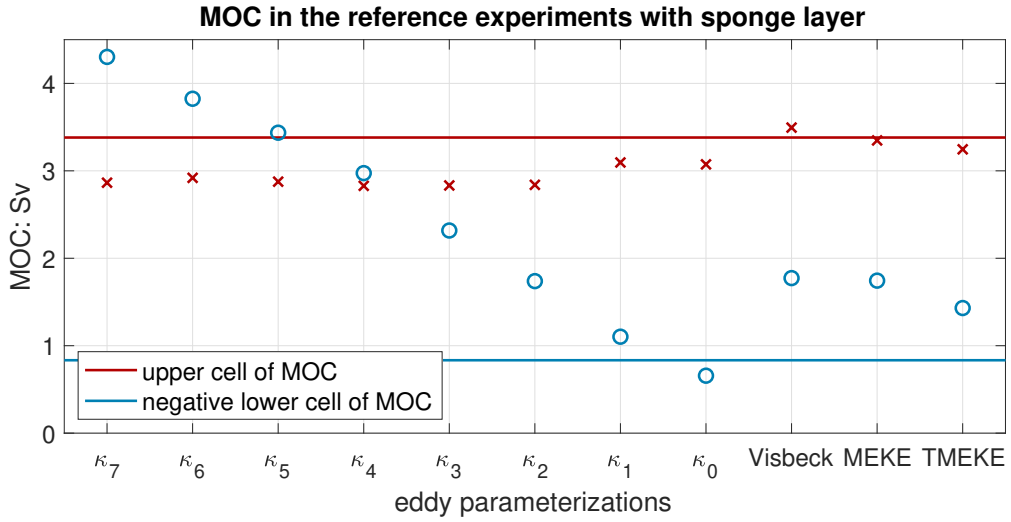

Figure 3.4: Upper and lower cell MOC magnitude with different eddy parameterizations in the reference case with sponge layer (full topography, $\tau_0 = 0.2$Pa). Horizontal lines denote results from the 0.1° reference simulation. Maroon crosses (blue open circles) denote the upper (lower) cell MOC from the 1° simulations. Notice that we are plotting the absolute values of the lower cell strength, whose streamfunction is by definition negative.

We find that the upper MOC cell is relatively well represented with either variable GM diffusivities or a small constant GM diffusivity, as is shown in Fig. 3.4. By contrast, the lower cell is generally less well represented in the non-eddying simulations, with large constant GM diffusivities in particular leading to a significant overestimate. We will focus on the upper cell in the rest of the paper.

Together with the comparison of the ACC transport, we conclude that there is no optimal value for a constant GM diffusivity: large GM diffusivities reproduce the ACC transport well but misrepresent the MOC, and vice versa for small GM diffusivities. The variable GM diffusivities, and particularly the MEKE-based parameterization with topographic β-effect (TMEKE), are able to reproduce both the ACC transport and the MOC reasonably well, although the lower

cell MOC strength remains overestimated.

Bulk isopycnal interface height error ε

As a third metric for evaluation, we consider the bulk isopycnal interface height error, defined as

$$\varepsilon \equiv \sum_{k=2}^{30} g'_k \left\langle \eta'^2_k \right\rangle, \tag{3.7}$$

where k is the isopycnal interface index, $g'_k = g(\sigma_k - \sigma_{k-1})/\rho_0$ is reduced gravity (g is the gravitational acceleration), η' is the difference in isopycnal interface height between the eddy-resolving simulation and any non-eddying simulation, and $\langle \cdot \rangle$ denotes a horizontal average over the whole domain (c.f. Jansen et al., 2019). ε quantifies the non-eddying models' ability to reproduce the density structure of the eddy-resolving simulation, with small ε indicating an accurate representation.

We find that the simulations using the TMEKE parameterization have the smallest isopycnal interface height error ε in both cases - with and without the sponge layer, as shown in Fig. 3.5. Comparing the two panels in Fig. 3.5 we find again that there is no optimal value for the constant GM diffusivity, κ_{GM}: while an intermediate GM diffusivity leads to a smaller error in the simulations without the sponge layer, it actually results in a larger error in the simulations with the sponge layer. We also notice that the overall amplitude of the isopycnal interface height error is smaller in the simulations with a sponge layer, as the density structure is more tightly constraint by the boundary conditions.

In the rest of this paper, we will focus on four formulations of the GM diffusivity that provide reasonably good results in the reference configuration: two values of constant κ_{GM} (κ_4 and κ_7), the Visbeck scheme, and the topographic MEKE parameterization (TMEKE).

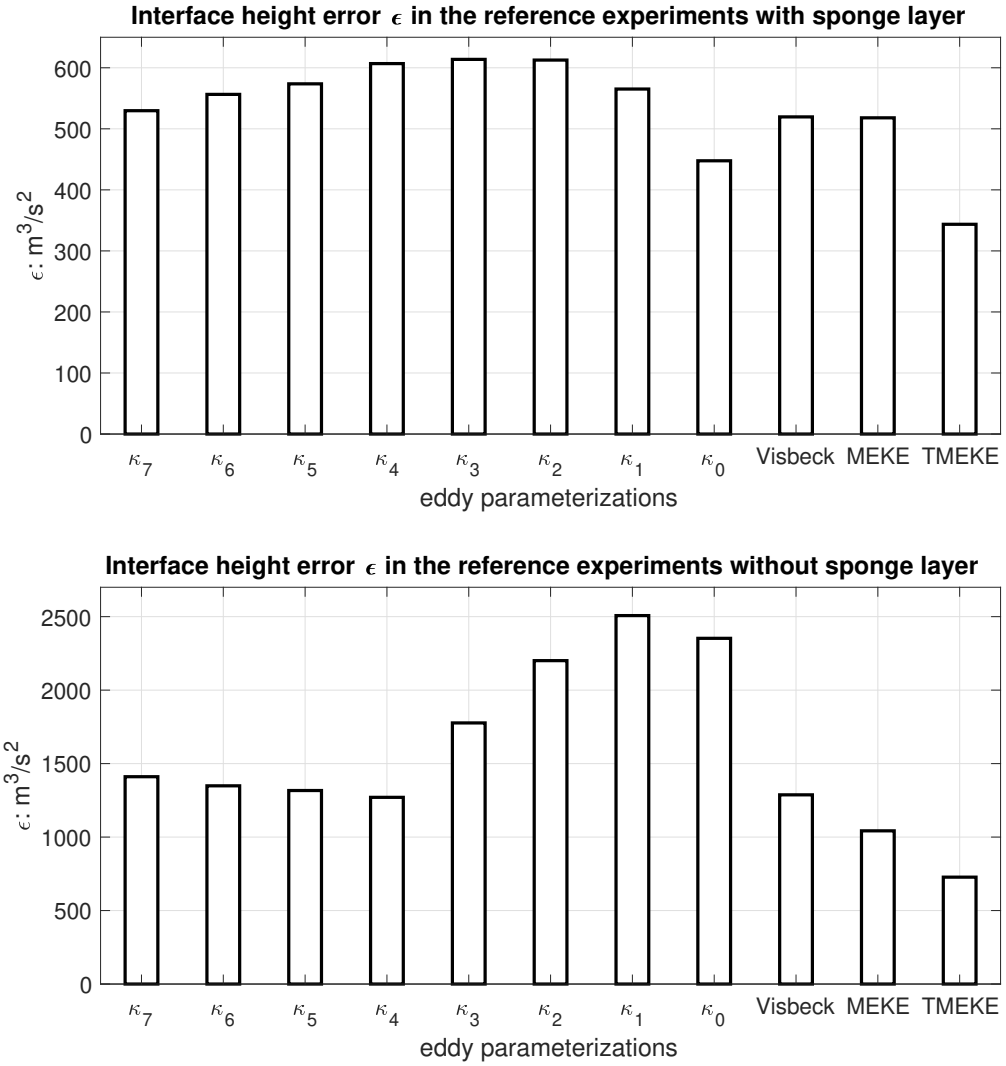

Figure 3.5: Isopycnal interface height error ε in the reference case: $\tau_0 = 0.2$ Pa, with full topography, with (top) and without (bottom) the sponge layer. (Notice the different y-axes in the two panels.)

3.4.2 The sensitivity of ACC transport to wind stress changes

In this section we focus on the response of the baroclinic ACC transport to changes in surface wind stress. To allow for an easier comparison to the established theories, we start with results from the flat bottom channel simulations, before proceeding to the full topography setup. We will show that the ACC transport sensitivity is significantly overestimated by the coarse resolution simulations in the flat bottom setup, because the parameterizations underestimate the sensitivity of the transient eddy diffusivity. By contrast, in the presence of topography, the sen-

sitivity of the ACC transport is only slightly overestimated by the coarse resolution simulations, as stationary eddies play a dominant role.

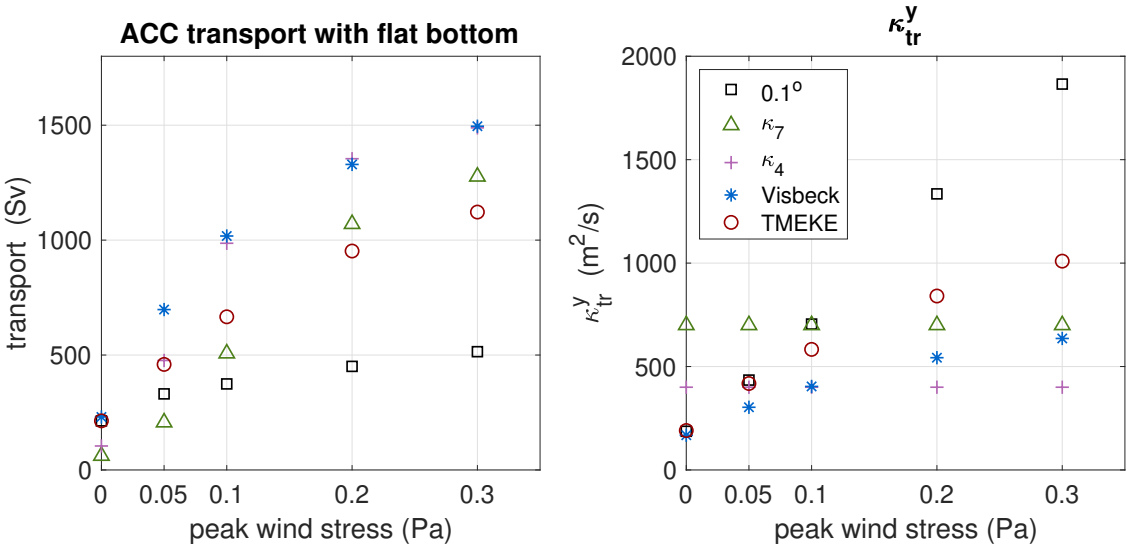

Figure 3.6: The response of baroclinic ACC transport (left) and meridional transient GM diffusivity (right) to surface wind stress changes in the flat bottom setup without sponge layer.

In the flat bottom simulations, all eddy parameterizations lead to a significant overestimate of the ACC transport response to wind stress changes, especially when a constant κ_{GM} is employed (Fig. 3.6). This result is expected for constant or insufficiently sensitive κ_{GM} because eddy fluxes will be increasingly inefficient at flattening the isopycnals as wind stress increases, resulting in a larger baroclinic ACC transport (c.f. Munday et al., 2013; Mak et al., 2018). To test the hypothesis that the overestimate of the ACC transport sensitivity results from an underestimate of the sensitivity of the eddy diffusivity, we compare the prescribed or predicted GM diffusivities to the resolved meridional eddy buoyancy diffusivity in the high resolution simulations (c.f. Viebahn and Eden, 2010). The domain averaged meridional transient eddy buoyancy diffusivity κ^y_{tr}, from the 0.1° simulations is estimated as

$$\kappa^y_{\mathrm{tr}} = -\frac{\{[\overline{v'b'}]\cdot[\partial_y \overline{b}]\}}{\{[\partial_y \overline{b}]^2\}} \tag{3.8}$$

where $\{\cdot\}$ denotes a volumetric domain average, $(\cdot)'$ denotes a departure from the temporal av-

erage, v is the meridional velocity, and $b = -g(\rho - \rho_0)/\rho_0$ is the buoyancy [2]. Correspondingly, κ^y_{tr} in the 1° simulations with a variable GM diffusivity is computed as

$$\kappa^y_{\text{tr}} = -\frac{\{[-\overline{\kappa_{\text{GM}} \partial_y b}] \cdot [\partial_y \overline{b}]\}}{\{[\partial_y \overline{b}]^2\}} \tag{3.9}$$

where κ_{GM} denotes the GM diffusivity, which is here assumed to represent the effect of transient eddies. (We confirmed that resolved transient eddies are negligible in the coarse resolution simulations.) The motivation for the specific averaging in Eqs. (3.8) and (3.9) is documented in Appendix 3.B.

The sensitivity of κ^y_{tr} to wind stress changes qualitatively explains the discrepancy of the ACC response across simulations (compare the left & right panels of Fig. 3.6). By definition, κ^y_{tr} remains constant in the κ_4 and κ_7 simulations, and these consequently have the most sensitive ACC transport response. Focusing on the 3 groups of simulations that either resolves eddies (0.1°) or have implemented a variable κ_{GM} (Visbeck & TMEKE), we further observe an inverse relationship between the sensitivities of κ^y_{tr} and ACC transport: the weakest ACC response among the three is obtained in the eddy-resolving simulation, which is associated with the most sensitive κ^y_{tr} response, while the strongest ACC response is obtained with the Visbeck scheme, which shows the lowest sensitivity in κ^y_{tr}. These observations support the hypothesis that an underestimate of the GM diffusivity sensitivity will lead to an overestimate of the sensitivity of the baroclinic ACC transport.

Another noteworthy result in Fig. 3.6 is that among all the 5 suites of simulations, the trend of the baroclinic ACC transport always saturates as wind stress increases: i.e. the response of the ACC transport to wind stress is sub-linear (which is also seen in the constant κ_{GM} simulations of Mak et al. (2018) - their Fig. 1). This sub-linear tendency is not consistent with simple

2. Notice that although our numerical simulations employ isopycnal coordinates, Eq. (3.8) is defined using z-coordinate diagnostics, which are provided by MOM6 via run-time coordinate mapping. A z-coordinate formulation has been favored to avoid ambiguities in the definition of eddy fluxes and GM transport in the presence of isopycnal outcrops and non-zero vertically integrated eddy volume flux (Khani et al., 2019).

scaling arguments, which suggest that in the adiabatic limit:

$$T_{\mathrm{ACC}} \sim -\frac{\Delta b L_y^2 \tau^2}{\rho_0^2 f^3 \kappa_{\mathrm{tr}}^{y\,2}}, \tag{3.10}$$

where Δb is the meridional buoyancy contrast across the channel, L_y is the latitudinal width of the channel, τ is the domain averaged surface wind stress, and f is a characteristic value for the Coriolis parameter in the ACC (see Appendix 3.D for the derivation of Eq. (3.10)). For constant κ_{GM} and hence constant κ_{tr}^{y} (i.e. the κ_7 & κ_4 cases), the ACC transport is thus expected to increase with the square of the wind stress, which is clearly inconsistent with the results of Fig. 3.6.

We argue that, at least in the constant κ_{GM} cases, the saturating trend of the baroclinic ACC transport at high winds is not due to the intensified meso-scale eddies but arises from a simple geometric constraint on the baroclinic transport. Specifically, the scaling argument in Eq. (3.10) starts to break down once isopycnals in the ACC start intersecting with the bottom of the ocean, at which point the sensitivity of the baroclinic transport to further wind stress increase starts to decline. Eventually, the transport will approach a theoretical limit, which is achieved when all isopycnals become vertical and the meridional buoyancy gradient becomes equal to the prescribed surface gradient throughout the depth of the ocean. A toy model that captures the effect of isopycnals intersecting with the sea floor is discussed in Appendix 3.E, and yields qualitatively similar results as seen in Fig. 3.6.

ACC transport response with full topography

In the presence of topography, the simulations with parameterized eddies (especially with variable κ_{GM}) only relatively slightly overestimate the sensitivity of the ACC transport to wind stress changes, when compared to the eddy-resolving simulations (panel (a) of Fig. 3.7). Moreover, the overestimate is not always due to an underestimate of the parameterized transient eddy diffusivity, κ_{tr}^{y}. Comparing panels (a) and (b) in Fig. 3.7 we find, for example, that κ_{tr}^{y} is

slightly more sensitive to wind stress changes with TMEKE than in the high resolution simulations, yet the ACC transport is also more sensitive in the simulations using TMEKE.

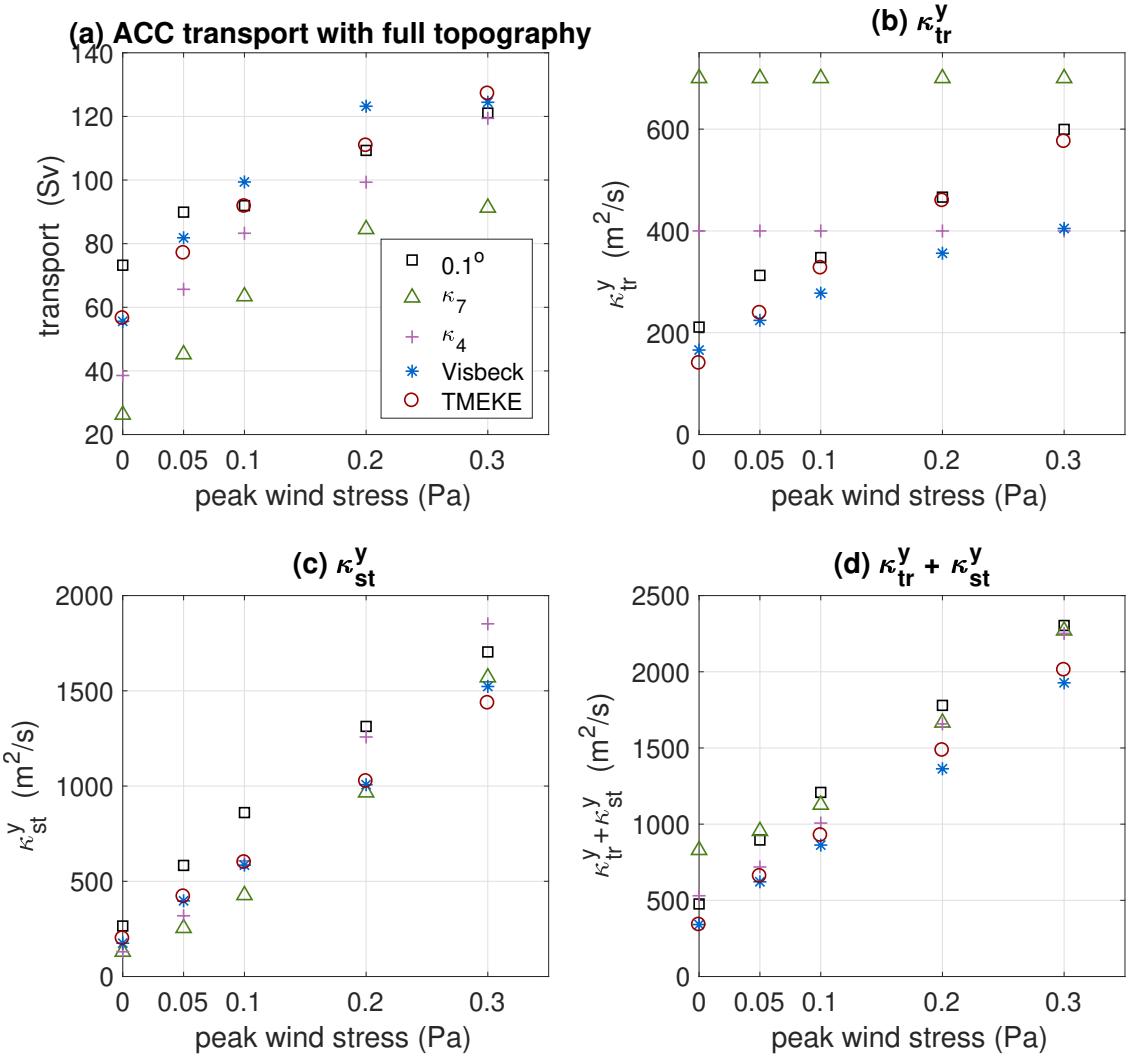

Figure 3.7: The response of (a) baroclinic ACC transport, (b) transient GM diffusivity, (c) stationary eddy buoyancy diffusivity, and (d) combined total eddy buoyancy diffusivity to changes in surface wind stress in the simulations with full topography and no sponge layer.

The key to understanding the sensitivity of ACC transport to wind stress changes in the simulations with topography is the role of standing eddies. To capture this influence we compute a mean stationary eddy buoyancy diffusivity, analogously to the transient eddy diffusivity as

$$\kappa^y_{\mathrm{st}} = -\frac{\{[\overline{v}^*\overline{b}^*]\cdot[\partial_y\overline{b}]\}}{\{[\partial_y\overline{b}]^2\}} \tag{3.11}$$

where $()^*$ denotes a departure from the zonal mean.

The magnitude and sensitivity of the stationary diffusivity is much higher than that of the transient diffusivity (panel (b) vs. (c) of Fig. 3.7), supporting the conclusion that, in the presence of topography, it is insufficient to consider only transient eddies to understand the ACC transport response to wind stress changes. Moreover, the sensitivity of κ^y_{st} to wind stress changes appears to compensate to some degree for the diverging sensitivities in the parameterized κ^y_{tr}, such that the combined eddy diffusivities are relatively similar across simulations configured with different eddy parameterizations and resolutions. The adequate representation of the combined diffusivity in the coarse resolution simulations explains their ability to capture the ACC transport sensitivity reasonably well. The simulations with the relatively large constant GM coefficient, κ_7, remain as somewhat of an outlier, as their ACC transport falls outside of the spread of the other simulations, even though the combined diffusivity falls within the range of the others, at least at strong wind stress. Nevertheless, we conclude that it is crucial to take into account the full set of "eddies", including both transient and stationary components, to understand the sensitivity of the ACC transport. Our results moreover suggest that even simulations with constant κ_{GM} are potentially able to reasonably represent the ACC transport under varying wind stress, as long as topographic features and the associated standing eddies can be resolved adequately.

An alternative approach to account for standing meanders, that has been taken in some previous studies, is to apply a zonal average along streamlines or time-mean buoyancy contours (e.g. Karsten and Marshall, 2002; Abernathey and Cessi, 2014). In this framework, the standing meanders, by construction, do not appear explicitly, but their effect is to enhance cross-contour transport through the stretching of buoyancy contours and associated sharpening of the local gradients (c.f. Nakamura, 1996, 2001; Abernathey and Cessi, 2014). Based on this idea, we derive an effective diffusivity diagnostic in Appendix 3.C that directly illustrates the effect of standing meanders via contour stretching. The stretching effect not only increases with wind stress, but also partially compensates for differences in the transient eddy diffusivity.

Such compensation may be expected as a large transient eddy buoyancy diffusivity will inhibit the formation of sharp meanders and vice versa.

3.4.3 The sensitivity of the MOC to wind stress changes

In this section we focus on the response of the MOC to changes in surface wind stress. We will first analyze how topography affects the MOC response to wind stress changes in the eddy-resolving simulations, before considering the representation of MOC changes with parameterized eddies. We show that in the flat bottom setup, eddy compensation is relatively weak and the MOC response is almost perfectly reproduced by coarse resolution simulations with eddy parameterizations, but this result arises from a peculiar compensation between errors in the responses of the eddy diffusivity and isopycnal slope. Adding topography significantly suppresses the MOC response to wind stress changes, just as found for the ACC transport, and the sensitivities of MOC, isopycnal slopes, and eddy diffusivity are all reasonably well represented by our coarse resolution simulations.

MOC response in eddy-resolving simulations

Topography again significantly suppresses the response of the MOC to surface wind changes, leading to a much smaller sensitivity than in the flat bottom channel (Fig. 3.8). Compared to the theoretical maximum Ekman transport, some eddy compensation (i.e. a reduced residual MOC response compared to the Ekman-driven MOC) is observed even in the absence of topography, but the degree of compensation becomes significantly more pronounced in the presence of topography. Therefore, topography appears to significantly reduce the response of the MOC to changes in surface wind stress, through the effect of stationary eddies.

This dominant role of stationary eddies is confirmed by decomposing the residual MOC streamfunction into zonal & temporal mean flow (hereafter: mean flow), stationary eddy, and transient eddy components (Fig. 3.9). The residual MOC, mapped into depth-space, is

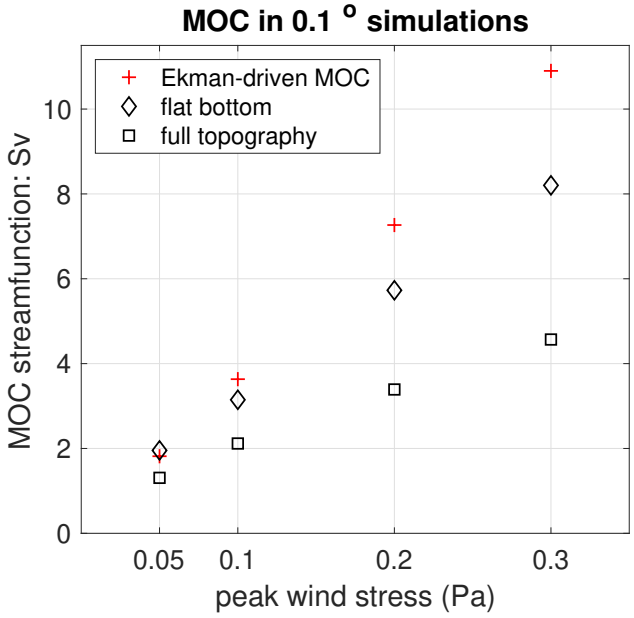

Figure 3.8: The response of the upper cell MOC to changes in surface wind stress, in the 0.1° simulations with sponge layer.

computed as

$$\psi(y,z) \equiv \psi(y,\sigma(y,z)) = \oint_x \int_{\sigma_s}^{\sigma(y,z)} \overline{v(x,y,\hat{\sigma}) \cdot h(x,y,\hat{\sigma})}\, \mathrm{d}\hat{\sigma}\mathrm{d}x. \tag{3.12}$$

where $\sigma(y,z)$ is the isopycnal with mean depth z, i.e. the inverse of $[\overline{z}(y,\sigma)]$ (e.g. Young, 2012) and σ_s is the minimum potential density at the surface.

We then decompose Eq. (3.12) into a temporal mean and a transient component. The temporal mean component is

$$\overline{\psi}(y,z) \equiv \oint_x \int_{\sigma_s}^{\sigma(y,z)} \overline{v}(x,y,\hat{\sigma}) \cdot \overline{h}(x,y,\hat{\sigma})\, \mathrm{d}\hat{\sigma}\mathrm{d}x, \tag{3.13}$$

and the transient component is

$$\psi_{\mathrm{tr}}(y,z) \equiv \psi - \overline{\psi} = \oint_x \int_{\sigma_s}^{\sigma(y,z)} \overline{v'(x,y,\hat{\sigma}) \cdot h'(x,y,\hat{\sigma})}\, \mathrm{d}\hat{\sigma}\mathrm{d}x. \tag{3.14}$$

The temporal mean MOC $\overline{\psi}$ is further decomposed into an Eulerian zonal mean and a

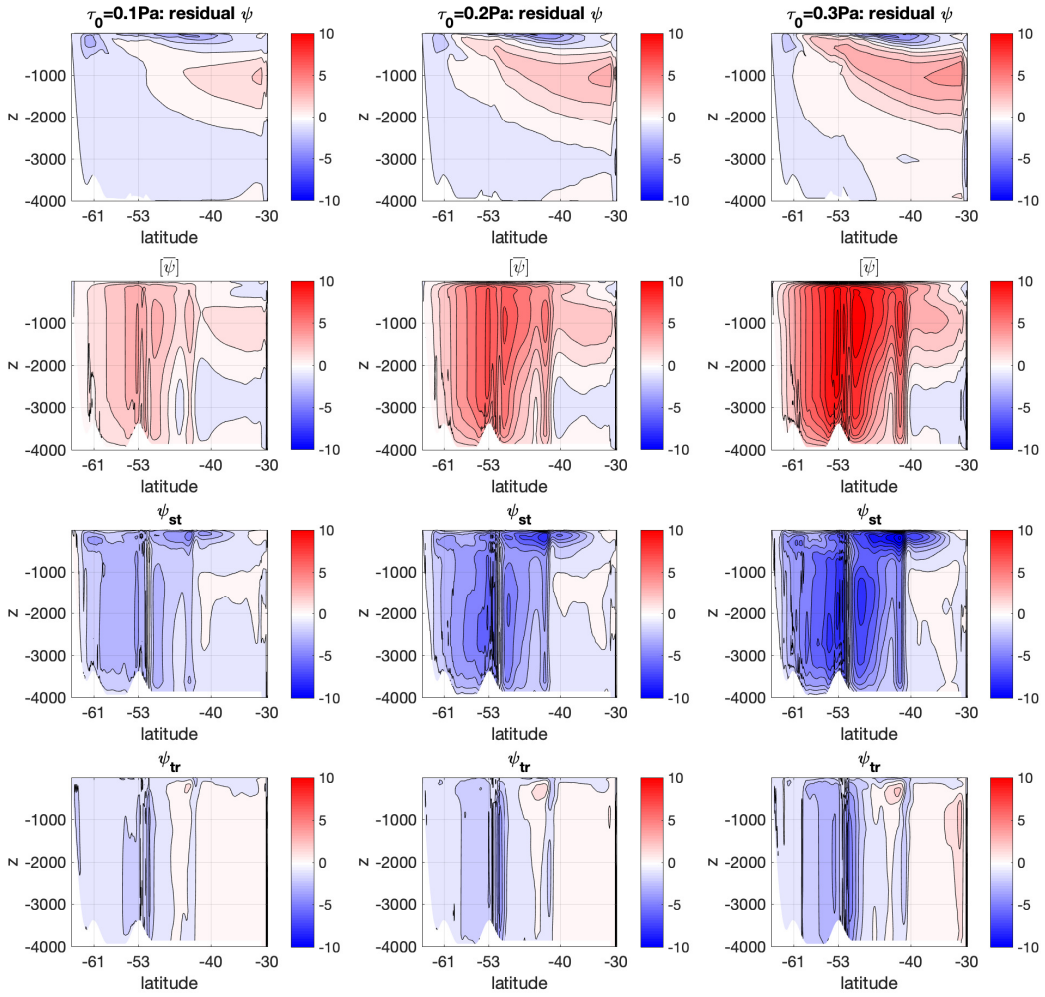

Figure 3.9: The response of MOC components to changes in surface wind stress in 0.1° simulations with full topography and northern sponge layer. Each column shows the MOC components for one value of wind stress (left: $\tau_0 = 0.1$Pa; center: τ_0=0.2Pa; right: $\tau_0 = 0.3$Pa). The rows from top to bottom correspond to: residual MOC ψ, zonal & temporal mean flow $[\overline{\psi}]$, stationary eddies ψ_{st}, and transient eddies ψ_{tr}. The contour interval is 1 Sv.

stationary eddy component. The Eulerian zonal mean part is defined based on an average at fixed depth, such that:

$$[\overline{\psi}](y,z) \equiv \oint_x \int_{z_s}^{z} \overline{v}(x,y,\hat{z})\, \mathrm{d}\hat{z}\mathrm{d}x, \tag{3.15}$$

where z_s is sea surface height. [3]

Last, the stationary eddy component ψ_{st} is

$$\psi_{\mathrm{st}}(y,z) \equiv \overline{\psi} - [\overline{\psi}]. \tag{3.16}$$

The dominant role of stationary eddies in counterbalancing the response of the wind-driven mean flow component to wind stress changes is clearly demonstrated in Fig. 3.9. While the transient eddies also intensify with wind stress, thus contributing to eddy compensation, their role is significantly smaller than that of the stationary eddies.

MOC response with parameterized eddies in the flat bottom channel

In the flat bottom channel, we find, somewhat surprisingly, that the coarse resolution simulations with all eddy parameterizations almost perfectly reproduce the response of the MOC to wind stress changes (panel (a) of Fig. 3.10). However, it turns out that this perfect representation is caused by a compensating effect between the responses of the transient eddy diffusivity and isopycnal slopes, neither of which is correctly represented in the coarse resolution simulations, but together they provide the correct response of the residual MOC.

This compensating effect can be understood via the residual MOC framework proposed by Marshall and Radko (2003), where the MOC is approximated as the sum of the wind-driven and transient eddy-induced components:

$$\psi \approx [\overline{\psi}] + \psi_{\mathrm{tr}} \approx -\frac{\tau}{\rho_0 f} + \kappa^y_{\mathrm{tr}}\, s \tag{3.17}$$

where $s = -\partial_y \overline{b} / \partial_z \overline{b}$ is the isopycnal slope. The response of ψ to (small) wind stress changes

3. One could alternatively also define the time and zonal mean component based on isopycnal averages, as done e.g. in Bishop et al. (2016). However, using isopycnal averaging will lead to a systematic eddy Ekman transport component (directed opposite to the net Ekman transport), because the Ekman transport is distributed over at least one isopycnal layer such that the Ekman velocity in that layer is inversely correlated with the layer thickness. We therefore here choose to isolate the Eulerian mean component as it better captures the wind-driven Ekman transport contribution. However, our main results are not sensitive to this choice.

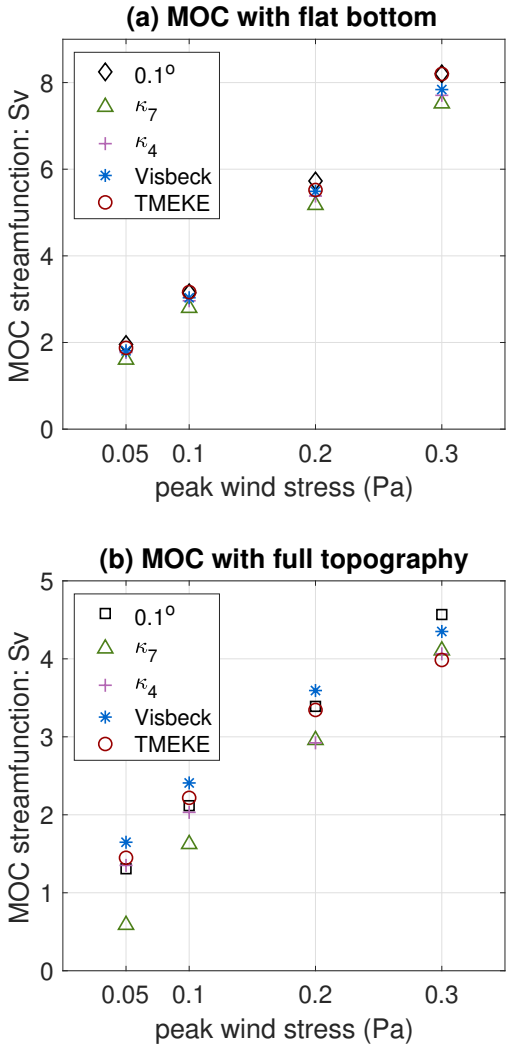

Figure 3.10: The response of the upper cell MOC to changes in surface wind stress in the 0.1° and 1° simulations with sponge layer, using (a) the flat bottom setup and (b) the full topography setup.

can then be approximated as

$$\partial_\tau \psi \approx -\frac{1}{\rho_0 f} + \partial_\tau \kappa^y_{\mathrm{tr}} \cdot s + \kappa^y_{\mathrm{tr}} \cdot \partial_\tau s. \tag{3.18}$$

As is shown in panel (a) of Fig. 3.11, the sensitivity of κ^y_{tr} to wind stress changes is underestimated in all parameterized simulations. Instead, the response of the isopycnal slopes is overestimated by the parameterized simulations (panels (b)-(f)). The simulations with constant GM diffusivity (κ_4 & κ_7) show the largest response in isopycnal slopes — developing a

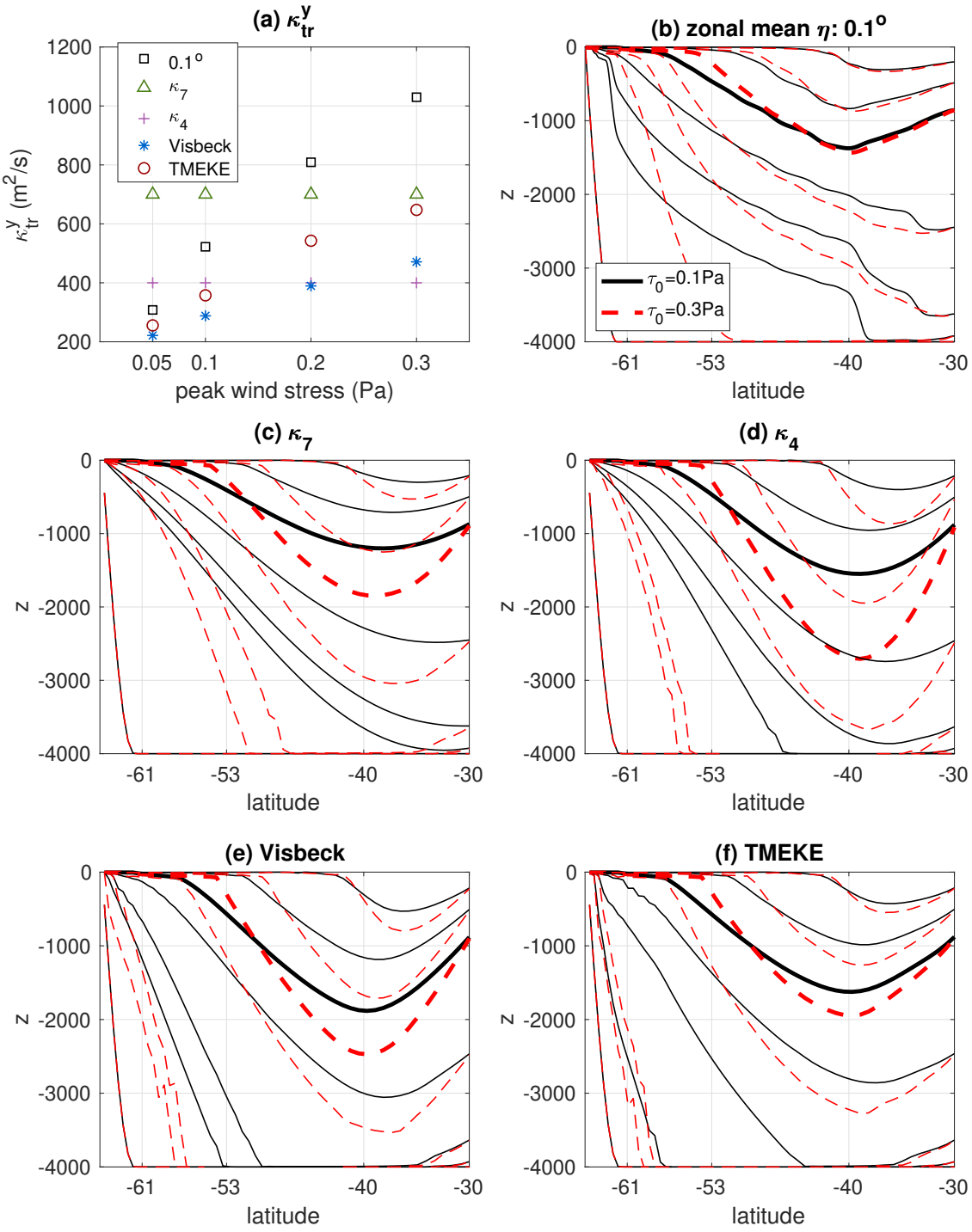

Figure 3.11: panel (a): Domain averaged meridional transient GM diffusivity as a function of wind stress from various simulations in the flat bottom setup with sponge layer at the northern boundary. panels (b)-(f): zonal mean isopycnal structure under wind stress $\tau_0 = 0.1$Pa (black solid lines) and $\tau_0 = 0.3$Pa (red dashed lines). Bold lines denote the $\sigma = 1037$ kg m^{-3} isopycnal, along which the upper MOC cell strength in Fig. 3.10 is evaluated.

pronounced V-shape in the isopycnal structure at strong winds. In the 0.1° simulation, where the eddy diffusivity is most sensitive to wind stress changes, the isopycnal slopes instead change relatively little, except in the abyssal ocean and at the highest latitudes. The simulations using Visbeck or TMEKE parameterizations show intermediate sensitivities in both κ^y_{tr} and isopycnal slopes. Why this almost perfect compensation between the sensitivities of κ^y_{tr} and isopycnal slopes exists, unfortunately, remains not clear to us, although the strong constraint imposed by the sponge layer appears likely to affect this result.

The compensating effect illustrated in Fig. 3.11 is reminiscent of the results shown in Viebahn and Eden (2010, their Fig. 5), whose eddy-permitting simulations produce the same amplitude of residual MOC response at different resolutions, due to a similar compensating effect. However, different from our result, Viebahn and Eden (2010) do not find the same compensation effect in their non-eddying simulations with parameterized eddies. Whatever the specific reason for the almost perfect error compensation in our simulations is, it is clear that the simulations with parameterized eddies do not adequately capture the response of the flat-bottom channel to wind stress changes.

MOC response with topography

When topography is included, the MOC response is reasonably well represented by the coarse resolution simulations (panel (b) of Fig. 3.10), and, unlike in the flat bottom simulations, the adequate MOC response does not arise from compensating errors. Instead, the sensitivities of both the total eddy diffusivity (i.e. $\kappa^y_{\mathrm{tr}}+\kappa^y_{\mathrm{st}}$) and isopycnal slope are relatively well captured in all coarse resolution simulations, as is illustrated in Fig. 3.12. The sensitivity of the total eddy diffusivity to changes in the wind stress is again strongly modulated by the effect of standing meanders (not shown) which reduces the sensitivity to the representation of transient eddies. The isopycnal structure is comparatively insensitive to wind stress changes in all simulations, indicating that any compensation is dominantly caused by the increase in the total eddy diffusivity with wind stress.

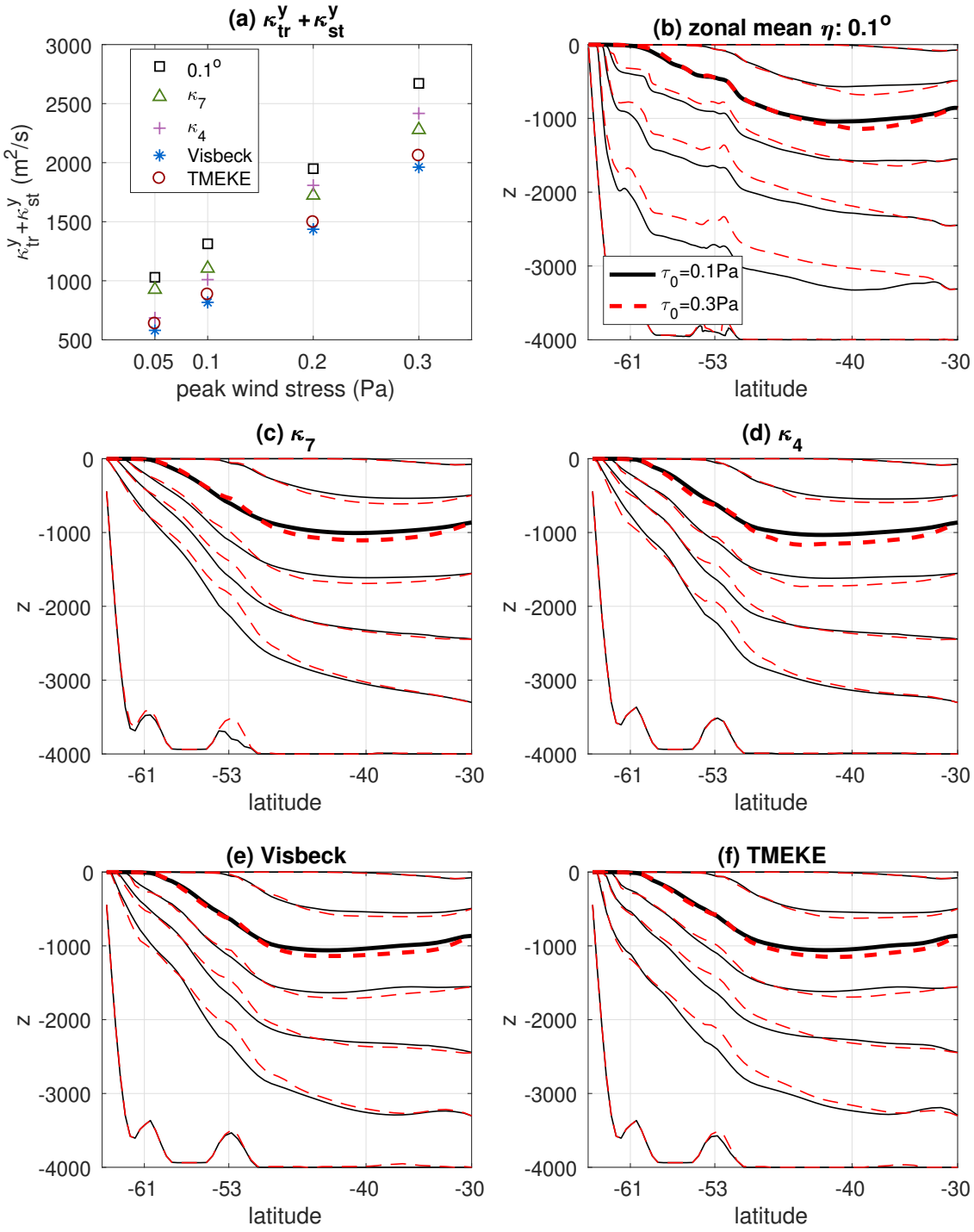

Figure 3.12: As Fig. 3.11 but for the simulations with topography. Also notice that panel (a) shows the combined stationary plus transient eddy buoyancy diffusivity, $\kappa^y_{\rm tr}+\kappa^y_{\rm st}$.

3.5 Discussion

In this study we employ four versions of an idealized channel model to study the response of Southern Ocean circulation to changes in surface wind stress. The idealized setup allows us to perform a large suite of equilibrated simulations under varying wind stresses and resolutions, but naturally also comes with a number of limitations.

Perhaps the most significant limitation of our study is the need for a northern boundary condition. To investigate the response of the ACC transport to wind stress changes we use an adiabatic northern boundary condition, which allows isopycnals to adjust freely at the northern boundary. By construction, this boundary condition only allows a very weak residual MOC, balanced by diffusion within the Southern Ocean, and hence amounts to assuming almost perfect eddy compensation: any increase in the wind-driven MOC needs to be almost completely compensated by the response in the eddy-induced MOC. However, when a basin is included to the north of the channel, previous studies (e.g. Gnanadesikan, 1999; Nikurashin and Vallis, 2012) suggest that any changes in the depth of the isopycnals in the basin should lead to a response in the rate of northern deep water formation and hence a change in the residual MOC in the Southern Ocean, which would exclude the possibility of perfect eddy compensation without perfect eddy saturation.

To study the MOC response to wind stress changes we adopt a sponge layer at the northern boundary, where the buoyancy is restored to a reference profile. The restoring crudely mimics water mass transformation processes that occur in the basins north of the Southern Ocean, and it is crucial to maintain a non-trivial residual MOC. However, the sponge layer essentially prohibits any substantial change of the stratification at the northern boundary, even as wind stress changes significantly. The circulation simulated with the sponge layer configuration may be a reasonable approximation for the short time-scale response of the real ocean, before the stratification in the basins has time to adjust. By contrast, this model configuration is probably unable to address the question of how the real MOC responds to wind stress changes in its final, equilibrium state. An alternative approach is to implement an enhanced diapycnal

mixing at the northern boundary, as adopted e.g. by Hogg (2010). However, this approach will generally only induce a counterclockwise MOC that is more similar to the abyssal cell. To quantitatively gauge the role of stratification adjustments in the basin on different time-scales, a direct comparison to inter-hemispheric model simulations is needed, which is part of ongoing work.

Our results may also depend on the specifics of the topography, which has previously been shown to affect the response of the ACC transport to surface wind stress changes (Nadeau et al., 2013). In the current study, our topography is smooth enough to be reasonably well resolved, even in our coarse resolution simulations. As a result we may expect that standing meanders excited by the topography can also be resolved reasonably well. Yet in the real ocean, topography spans a wide spectrum of spatial scales, and hence the ability of coarse resolution models to capture the effects of stationary eddies is likely to be more significantly impaired. How this difference impacts the conclusions of the current work needs to be addressed in the future.

Our results for the sensitivity of the ACC transport to wind stress changes differ from those of Mak et al. (2018), who find almost perfect eddy saturation in their eddy-permitting simulations. The perfect eddy saturation is also largely captured by their coarse resolution simulations configured with the GEOMETRIC eddy parameterization, but is not reproduced with a constant GM diffusivity. The difference between their and our results may be related to multiple differences in the model configurations, but one distinction that is highlighted by the theory behind the GEOMETRIC parameterization lies in the form of the bottom drag: while bottom friction is represented via a linear drag in their model setup, our model adopts a quadratic drag. Perfect eddy saturation arises with the GEOMETRIC parameterization if and only if the eddy energy dissipation is assumed to follow a linear drag law (Marshall et al., 2017).

Our results for the ACC transport sensitivity with topography are broadly consistent with those of Farneti et al. (2015). However, our results for the MOC response with topography seem to stand in contrast with those of Farneti et al. (2015) and Poulsen et al. (2018). Particularly,

Farneti et al. (2015) find that GCMs that either are eddy-permitting or have implemented a κ_{GM} with 3D spatial structure tend to have a significantly higher degree of eddy compensation than the models whose κ_{GM} is constant or employs a 2D spatial structure. Yet our Fig. 3.10 shows that both a constant κ_{GM} (the κ_4 case) and a 2D varying κ_{GM} (Visbeck, TMEKE) are able to reproduce a similar degree of eddy compensation as the eddy-resolving simulations, due to the effect of stationary eddies, which allow a realistic representation of the total (stationary plus transient) eddy diffusivity (Fig. 3.12). One obvious difference in our study is the idealized model configuration, in particular the use of a sponge layer to restore the stratification at the northern boundary, as well as the relatively smooth simplified topography (as discussed above). Perhaps even more importantly, the simulations in Poulsen et al. (2018) are only integrated for 17 years, and the GCMs in Farneti et al. (2015) are forced with wind stress changes over a 60-year period, which leads to a strongly diabatic non-equilibrium MOC response pattern. The MOC changes in our fully equilibrated simulations instead are largely adiabatic in the interior, which adds a significant constraint on the MOC response. The time-dependent response of the ACC and MOC to wind stress changes will be addressed in a follow-up study.

3.6 Conclusions

The surface wind stress over the Southern Ocean has been increasing significantly for decades, yet the response of the Southern Ocean circulation to the wind stress change has not been fully understood. In this work we have used four versions of idealized models of the Southern Ocean to investigate the circulation response to changes in surface wind stress. We have explored the role of topography in modulating this response and tested several state-of-the-art eddy parameterizations to analyze in how far coarse resolution simulations with parameterized eddies can reproduce the response, with and without topography. Our main finding is that some degree of both eddy saturation and compensation exist in our model, even in the absence of topography. However, topography significantly increases the degree of eddy saturation and compensation, by inducing strong stationary eddies that substantially amplify the

effect of the transient eddies. The coarse resolution simulations with parameterized eddies are able to reproduce the circulation response reasonably well in the presence of topography. Although state-of-the art eddy parameterizations with variable GM diffusivity generally perform better, the ACC and MOC responses to wind stress changes are surprisingly well captured even when using a constant GM diffusivity. We attribute this result to the key role played by standing meanders, which dominate the meridional buoyancy flux. In the absence of topography, however, the simulations with parameterized eddies struggle to represent an accurate ACC transport response. The MOC response is reproduced correctly, but only due to compensating errors in the responses of the eddy diffusivity and isopycnal slopes.

Our results highlight the importance of topography in modulating the response of the Southern Ocean circulation to changes in surface wind stress, which deserves more attention in future development and testing of eddy parameterizations. In the meantime, our results provide hope that GCMs with realistic topography are less sensitive to the choice of meso-scale eddy parameterizations than suggested by idealized flat bottom models and theories.

Appendix 3.A Eddy parameterizations

3.A.1 Visbeck scheme

The Visbeck scheme used in our model is based on Visbeck et al. (1997). It is implemented in MOM6 as

$$\kappa_{\mathrm{GM}} = \alpha l^2 \langle S \cdot N \rangle \tag{3.19}$$

where $\alpha = 0.015$ is an empirical non-dimensional coefficient, chosen as in Visbeck et al. (1997); $l = 100$km in our setup, which allows us to roughly match the ACC transport and the upper cell MOC of the 0.1° simulations in the reference case; S is the isopycnal slope, N is the Brunt-Väisälä frequency, and $\langle \cdot \rangle$ denotes a vertical average.

3.A.2 MEKE

The MEKE scheme is based on Jansen et al. (2015), and uses a prognostic equation for the vertically integrated sub-grid meso-scale eddy kinetic energy (MEKE; their Eq. (1)):

$$\partial_t E = \dot{E}_{\mathrm{GM}} - \dot{E}_{\mathrm{fric}} - \nabla \cdot T \tag{3.20}$$

where E is MEKE, $\dot{E}_{\mathrm{GM}}$ is the large-scale energy loss associated with the GM parameterization, $\dot{E}_{\mathrm{fric}}$ is the frictional dissipation of MEKE, and T is the horizontal transport of MEKE, here parameterized via a diffusion of MEKE with a diffusivity $\kappa_{\mathrm{MEKE}} = 1000\mathrm{m\ s}^{-2}$.

The meso-scale kinetic energy E is then combined with the mixing length l_M to form the GM diffusivity

$$\kappa_{\mathrm{GM}} = l_M \sqrt{\gamma_t^2 U_e^2} \tag{3.21}$$

where $U_e = \sqrt{2E}$, $l_M = \alpha / (L_e^{-1} + L_R^{-1} + L_\Delta^{-1})$ ($\alpha = 0.12$ has been optimized based on the reference case; $L_e = U_e / (|S|N)$ is the Eady scale, $L_R = \sqrt{U_e/\beta}$ is the Rhines scale, and L_Δ is the grid spacing), and $\gamma_t^2 = \max[(1 + 50 L_d / L_f)^{-1/4},\ 1 \times 10^{-4}]$ is an estimate for the ratio of

barotropic to total EKE (with L_d the Rossby radius of deformation, $L_f = H/C_D$ the frictional halting scale, H the ocean depth, and $C_D = 0.003$ the quadratic drag coefficient). Additional details are provided in Jansen et al. (2015).

3.A.3 Topographic MEKE

The topographic MEKE formulation is similar to MEKE but considers the suppression of the GM diffusivity by the topographic β effect. Specifically, the Rhines Scale L_R is computed using a topographically modified barotropic potential vorticity gradient:

$$\beta^* = \sqrt{(\partial_x f - \frac{f}{H}\partial_x H)^2 + (\partial_y f - \frac{f}{H}\partial_y H)^2}. \tag{3.22}$$

Appendix 3.B Domain averaged meridional transient and stationary GM diffusivity

The effective domain-averaged GM diffusivity in Eq. (3.8) is computed by minimizing the RMS error of the implied meridional eddy buoyancy flux. We aim to approximate the zonally averaged meridional transient eddy buoyancy flux $[\overline{v'b'}]$ in the 0.1° simulations with a representative transient eddy diffusivity κ^y_{tr} as

$$[\overline{v'b'}] = -\kappa^y_{\text{tr}}[\partial_y \overline{b}] + \delta, \tag{3.23}$$

where δ is the residual. Our goal is to find the κ^y_{tr} that minimizes the domain-averaged δ^2:

$$\{\delta^2\} = \{([\overline{v'b'}] + \kappa^y_{\text{tr}}[\partial_y \overline{b}])^2\} = \{[\overline{v'b'}]^2\} + 2\kappa^y_{\text{tr}}\{[\overline{v'b'}] \cdot [\partial_y \overline{b}]\} + {\kappa^y_{\text{tr}}}^2\{[\partial_y \overline{b}]^2\}. \tag{3.24}$$

Let $\partial_{\kappa^y_{\text{tr}}}\{\delta^2\} = 0$ and we retrieve Eq. (3.8).

Similarly, for the 1 deg simulations, Eq. (3.23) is replaced by

$$-[\overline{\kappa_{\mathrm{GM}}\partial_y b}] = -\kappa^y_{\mathrm{tr}}[\partial_y \overline{b}] + \delta, \tag{3.25}$$

and following the same procedure we retrieve Eq. (3.9).

The derivation of Eq. (3.11) is almost identical to Eq. (3.8), except we replace $[\overline{v'b'}]$ in Eq. (3.23) by $[\overline{v}^*\overline{b}^*]$.

Appendix 3.C Interpreting the effect of standing eddies via stretching of mean contours

In Eqs. (3.8), (3.9), and (3.11), the total eddy buoyancy flux across any latitude circle is defined in terms of the sum of a transient and a stationary component

$$F_y = L_x\left[\overline{v}^*\overline{b}^* + \overline{v'b'}\right] = -L_x(\kappa^y_{\mathrm{st}} + \kappa^y_{\mathrm{tr}})\left[\partial_y \overline{b}\right], \tag{3.26}$$

where L_x is the zonal length of the domain at this latitude.

An alternative streamwise mean perspective has also been taken by previous studies, where the zonal average is taken along temporarily averaged streamlines or buoyancy contours (Karsten and Marshall, 2002; Abernathey and Cessi, 2014). In this case, the standing eddy flux vanishes by construction, and the transport across a mean buoyancy contour $\bar{b} = b_0$ is

$$F_{b_0} \equiv \int_{\overline{b}=b_0} \overline{v'_n b'}\mathrm{ds} \equiv \int_{\overline{b}=b_0} \overline{\mathbf{u}'b'}\cdot\frac{\nabla_z\overline{b}}{|\nabla_z\overline{b}|}\mathrm{ds} = -\int_{\overline{b}=b_0} K_{\mathrm{tr}}|\nabla_z\overline{b}|\mathrm{ds}, \tag{3.27}$$

where $v_n \equiv \mathbf{u}\cdot\nabla_z\overline{b}/|\nabla_z\overline{b}|$ is the normal velocity across the buoyancy contour, ∇_z denotes the horizontal gradient (at constant z) and we defined a local (cross-contour) transient eddy buoyancy diffusivity as

$$K_{\mathrm{tr}} \equiv -\frac{\overline{\mathbf{u}'b'}\cdot\nabla_z\overline{b}}{|\nabla_z\overline{b}|^2}. \tag{3.28}$$

Following Nakamura (1996), the cross-contour flux in Eq. (3.27) can be expressed as

$$F_{b_0} = -\int_{\overline{b}=b_0} K_{\rm tr}|\nabla_z \overline{b}|\mathrm{ds} = -\frac{\partial \mathscr{A}(K_{\rm tr}|\nabla_z \overline{b}|^2)}{\partial b_0} = -\left\langle K_{\rm tr}|\nabla_z \overline{b}|^2 \right\rangle \frac{\partial A}{\partial b_0}, \tag{3.29}$$

where

$$\mathscr{A}(\cdot) \equiv \iint_{\overline{b}\le b_0} (\cdot)\mathrm{dA} \tag{3.30}$$

denotes an integral over the area delimited by the mean buoyancy contour $\bar{b} = b_0$, $A = \mathscr{A}(1)$, and $\langle(\cdot)\rangle \equiv \partial_A \mathscr{A}(\cdot)$ defines an average along the mean buoyancy contour. With an effective latitude, $Y(b_0)$, defined such that $L_x \partial_{b_0} Y = \partial_{b_0} A$ (Nakamura and Zhu, 2010), we get

$$F_{b_0} = -L_x K_{\rm eff} \frac{\partial b_0}{\partial Y}, \tag{3.31}$$

where

$$K_{\rm eff} \equiv \frac{\left\langle K_{\rm tr}|\nabla_z \overline{b}|^2 \right\rangle}{|\partial_Y b_0|^2}. \tag{3.32}$$

Eqs. (3.31) and (3.32) illustrate that standing meanders increase the effective meridional buoyancy diffusivity via a stretching of buoyancy contours, which sharpens the local gradients. This effect is analog to the amplification of mixing by eddy-induced contour stretching discussed by Nakamura (1996), except we are here considering only the stretching effect of standing meanders, with the transient eddy diffusivity replacing micro-scale diffusion.

Assuming that $F_y \approx F_{b_0}$ and $|\partial_Y b_0|^2 \approx [\partial_y \bar{b}]^2$, comparison of Eqs. (3.26) and (3.31) shows that $K_{\rm eff} \approx \kappa^y_{\rm st} + \kappa^y_{\rm tr}$. Assuming further that, on average, $\left\langle K_{\rm tr}|\nabla_z \overline{b}|^2 \right\rangle \approx \left[K_{\rm tr}|\nabla_z \overline{b}|^2\right]$, the effective diffusivity can be approximated as

$$K_{\rm eff} \approx \frac{[K_{\rm tr}|\nabla_z \overline{b}|^2]}{[\partial_y \bar{b}]^2}. \tag{3.33}$$

Following the same argument as in Appendix 3.B, we can define a domain-averaged (cross-

contour) transient buoyancy diffusivity as

$$K_{\mathrm{tr}}^{d} \equiv \frac{\left\{K_{\mathrm{tr}} |\nabla_z \overline{b}|^2\right\}}{\left\{|\nabla_z \overline{b}|^2\right\}} \tag{3.34}$$

and a domain averaged effective diffusivity as

$$K_{\mathrm{eff}}^{d} \equiv \frac{\left\{K_{\mathrm{tr}} |\nabla_z \overline{b}|^2\right\}}{\left\{[\partial_y \overline{b}]^2\right\}} = K_{\mathrm{tr}}^{d} \frac{\left\{|\nabla_z \overline{b}|^2\right\}}{\left\{[\partial_y \overline{b}]^2\right\}} \,. \tag{3.35}$$

As shown in panel (b) of Fig. 3.13, the effective diffusivity K_{eff}^{d} is qualitatively similar to the combined (stationary plus transient) diffusivity shown in panel (d) of Fig. 3.7. As illustrated in panel (c), the effective diffusivity K_{eff} is significantly amplified by the stretching effect, especially in the 0.1° simulations, where the stationary meanders are relatively strong. Moreover, for any given wind stress, the stretching effect tends to be stronger in simulations that have a small transient diffusivity and vice versa, therefore compensating to some degree (albeit not completely) for differences in the transient diffusivity. This compensating effect may be expected, as a large diffusivity tends to smooth standing meanders, and it is somewhat similar to the insensitivity of Nakamura's effective diffusivity to the magnitude of micro-scale diffusion (although true insensitivity cannot be expected unless the stretching factor is much larger than one, which is not the case here).

Appendix 3.D A simple scaling for the baroclinic ACC transport in an adiabatic, flat-bottom channel

In an adiabatic limit, the residual circulation has to vanish and Eq. (3.17) reduces to

$$\kappa_{\mathrm{tr}}^{y} \, s = \frac{\tau}{\rho_0 f}, \tag{3.36}$$

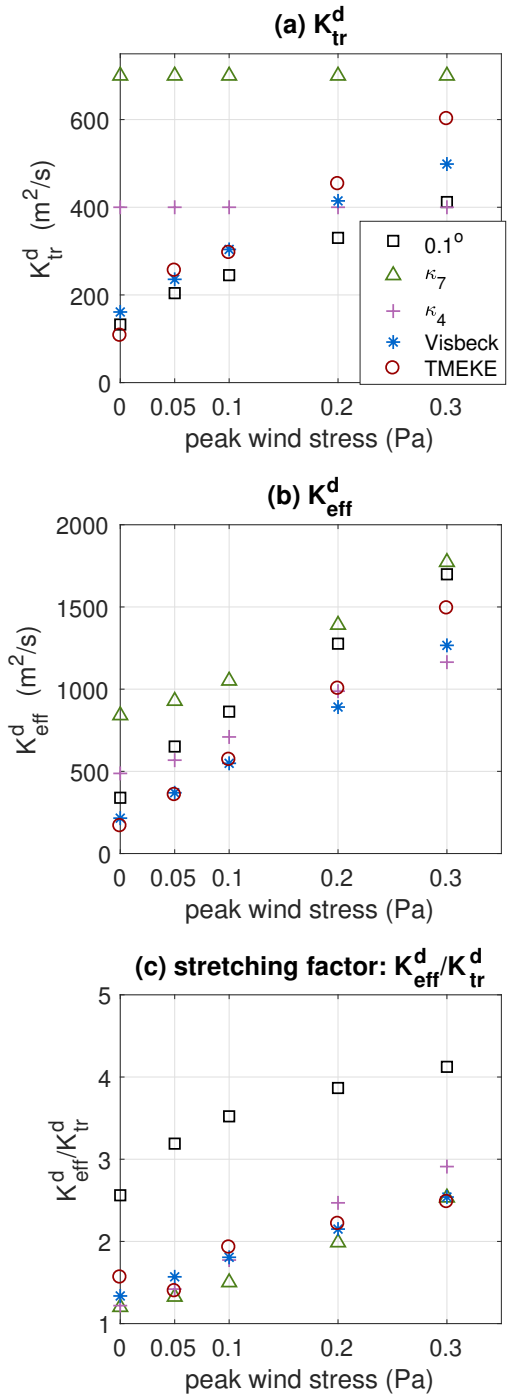

Figure 3.13: (a): Transient GM diffusivity K^d_{tr} as a function of wind stress, in the simulations with full topography and no sponge layer; (b): Effective diffusivity K^d_{eff} as a function of wind stress in the same simulations. (c): The stretching factor, $K^d_{\text{eff}}/K^d_{\text{tr}}$.

where $s \sim -h_0/L_y$, with h_0 the depth of the densest isopycnal at the northern boundary and L_y the width of the channel (see panel(a) of Fig. 3.14 for a schematic), and τ is the wind

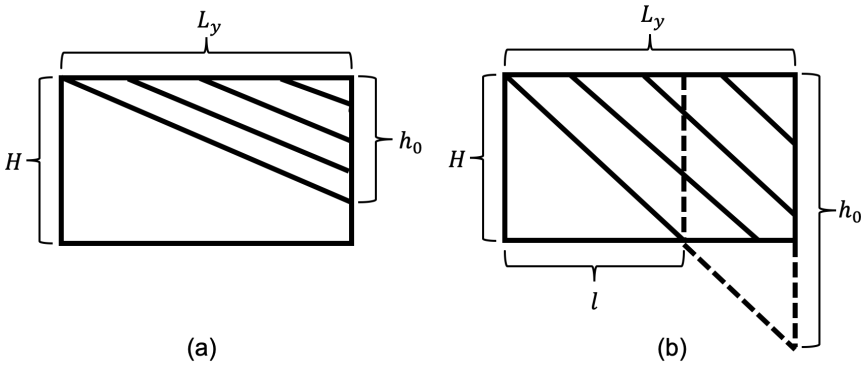

Figure 3.14: Schematics for the ACC toy model. In each panel, south is on the left. (a) $|s| \leq H/L_y$: no incropping occurs. (b) $|s| > H/L_y$: incropping occurs.

stress. Therefore, h_0 scales as

$$h_0 \sim -\frac{\tau L_y}{\rho_0 f \kappa_{\mathrm{tr}}^y}. \tag{3.37}$$

Assuming that the baroclinic ACC flow follows the thermal wind relation, we obtain a scaling for the baroclinic zonal velocity as

$$u \sim -\frac{h_0 \Delta b}{f L_y}. \tag{3.38}$$

Integrating Eq. (3.38) and using Eq. (3.37) yields the scaling in Eq. (3.10):

$$T_{\mathrm{ACC}} \sim u h_0 L_y \sim -\frac{\Delta b L_y^2 \tau^2}{\rho_0^2 f^3 \kappa_{\mathrm{tr}}^{y\,2}}. \tag{3.39}$$

Appendix 3.E A toy model for the baroclinic ACC transport in a channel with finite depth

To understand the effect of isopycnal incrops on the baroclinic ACC transport at strong wind stress, we construct a simple toy model, assuming:

(1) a zonally symmetric and flat bottomed channel, with a prescribed constant surface buoyancy gradient;

(2) isopycnal slopes are constant with depth and latitude;

(3) variations in the Coriolis parameter are negligible;

(4) the residual MOC, balanced by diapycnal mixing within the channel, can be approximated as $\psi \approx -\kappa_d / s$, where κ_d is the diapycnal diffusivity (Ito and Marshall, 2008).

Under these assumptions, Eq. (3.17) can be written as

$$\kappa_d \frac{L_y}{h_0} = \frac{\tau}{\rho_0 f} + \kappa_{\mathrm{tr}}^y \frac{h_0}{L_y} \tag{3.40}$$

where $\kappa_d = 5 \times 10^{-5} \mathrm{m}^2\ \mathrm{s}^{-1}$, $h_0 = -sL_y$ is the depth of the densest isopycnal at the northern boundary, $\rho_0 = 1037 \mathrm{kg\ m}^{-3}$, and $f = -1 \times 10^{-4} \mathrm{s}^{-1}$. Solving Eq. (3.40) for h_0 we find

$$h_0 = \left(\frac{-\tau}{2\rho_0 f \kappa_{\mathrm{tr}}^y} + \sqrt{\left(\frac{-\tau}{2\rho_0 f \kappa_{\mathrm{tr}}^y} \right)^2 + \frac{\kappa_d}{\kappa_{\mathrm{tr}}^y}} \right) L_y. \tag{3.41}$$

Notice that once the densest isopycnal begins to incrop with the sea floor (right panel), h_0 becomes a hypothetical depth, which is the depth of this isopycnal at the northern boundary if the ocean were infinitely deep (panel(b) in Fig. 3.14). In this case, we use l to denote the distance between the southern boundary and the incropping location of this densest isopycnal (with $l = L_y$ if no incropping occurs):

$$l = \min\left(\frac{H}{h_0} L_y,\ L_y \right). \tag{3.42}$$

Meanwhile, the thermal wind relation, $\partial_z u_{\mathrm{bc}} = -\frac{1}{f} \partial_y b$, provides the baroclinic zonal velocity as

$$u_{\mathrm{bc}}(y,z) = -\frac{1}{f} \int_{-h(y)}^{z} \partial_y b\ \mathrm{d}z = -\frac{\Delta b}{f L_y} \left(h(y) + z \right) \tag{3.43}$$

where $h(y) = \min\left(h_0 y / L_y,\ H \right)$ is the depth of the densest isopycnal interface, below which the stratification and the baroclinic zonal flow both vanish. Using that $h(y) = h_0 y / L_y$ for

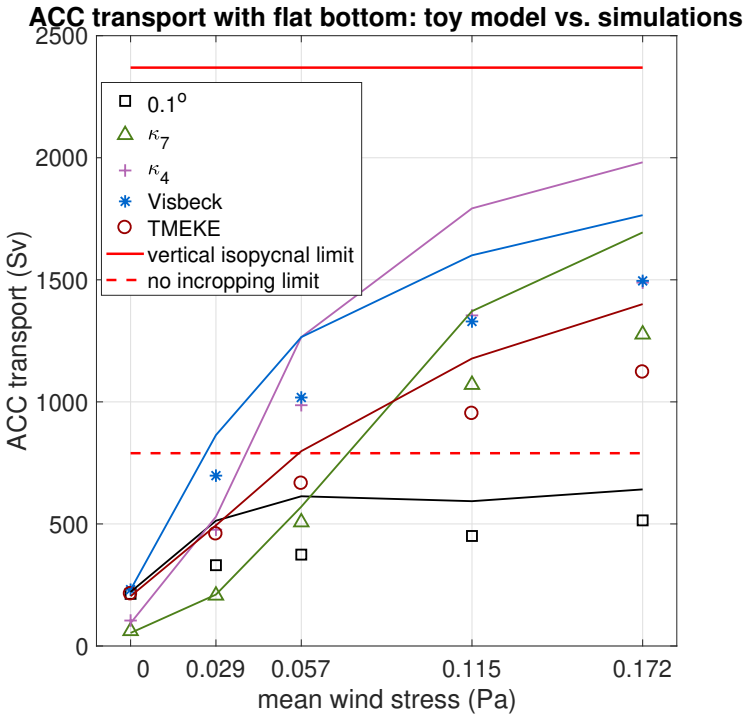

Figure 3.15: The baroclinic ACC transport from the simulations (markers) and from the toy model (polylines). Markers and polylines of the same color denote the same eddy parameterization. The solid red line denotes the largest possible baroclinic ACC transport, achieved when all isopycnals become vertical (i.e. $l = 0$, $h_0 \to \infty$); the dashed red line denotes the largest possible transport without any incropping (i.e. $l = L_y$, $h_0 = H$). Notice that the x-axis here denotes the domain averaged wind stress τ, which is a more adequate measure of the effective wind stress in Eq. (E2) than the peak wind stress τ_0.

$y < l$ and $h(y) = H$ for $y \geq l$, we can compute the baroclinic ACC transport as

$$\begin{aligned} T_{\mathrm{ACC}} &= \int_0^{L_y} \int_{-h(y)}^{0} u_{\mathrm{bc}}(y,z)\mathrm{d}z\mathrm{d}y \\ &= -\frac{\Delta b}{f L_y} \int_0^{L_y} \frac{h(y)^2}{2}\mathrm{d}y \\ &= -\frac{\Delta b}{2 f L_y} \left(\int_0^{l} \frac{h_0^2}{L_y^2} y^2 \mathrm{d}y + \int_l^{L_y} H^2 \mathrm{d}y \right) \\ &= -\frac{\Delta b h_0^2}{6 f L_y^3} \cdot l^3 - \frac{\Delta b H^2}{2 f L_y} \cdot (L_y - l) \end{aligned} \tag{3.44}$$

where h_0 is given by Eq. (3.41) and l is given by Eq. (3.42).

The toy model qualitatively captures the response of the ACC transport to wind stress

changes in our simulations (Fig. 3.15). Importantly, it reproduces the sub-linear trend of the transport with wind stress in the simulations with parameterized eddies, including those that adopt a constant κ^y_{tr}. The sub-linear trend appears once the ACC transport exceeds the dashed red line, which denotes the largest ACC transport before isopycnals start to incrop ($h_0 = H$). The results show that it is primarily the incropping of isopycnals, rather than the response of meso-scale eddies, that leads to the saturating trend of the ACC transport in the coarse resolution simulations with flat bottom and parameterized eddies. By contrast, in the high resolution simulations, the critical value of ACC transport is never reached, indicating that little incropping occurs even at strong wind stress, and the saturating trend of the ACC transport is indeed caused by meso-scale eddies.

CHAPTER 4

TIME-DEPENDENT RESPONSE OF THE GLOBAL OCEAN CIRCULATION TO CHANGES IN SOUTHERN OCEAN SURFACE WIND STRESS

4.1 Introduction

Surface wind stress is a most important driving force for the global ocean circulation. Therefore, given the increasing trend of surface wind stress over the Southern Ocean during the recent decades (e.g. Swart and Fyfe, 2012), it is important to understand the response of both the Southern Ocean and global large-scale ocean circulations to this wind stress increase.

Observational and theoretical progress has been made on the local response of Southern Ocean circulation to the wind stress increase. In general, on timescales longer than 1 year, the Antarctic Circumpolar Current (ACC) transport seems to remain relatively unaffected (e.g. Straub, 1993; Böning et al., 2008; Munday et al., 2013), while the Southern Ocean meridional overturning circulation (SOMOC) shows a mild increase (e.g. Hallberg and Gnanadesikan, 2006; Viebahn and Eden, 2010; Abernathey et al., 2011).

In chapter 3 we analyzed the equilibrium response of the ACC transport and the SOMOC to changes in surface wind stress using an idealized channel model, as considered in several previous studies (e.g. Abernathey et al., 2011; Abernathey and Cessi, 2014; Nadeau and Ferrari, 2015; Constantinou, 2018; Mak et al., 2018). The reason for choosing a channel model is because it computationally allows the meso-scale eddies to be fully resolved due to the channel's small domain. However, one potential issue with the channel configuration is that we have to explicitly specify its northern boundary condition. Specifically, to investigate the response of the ACC transport, in the channel model we used an adiabatic northern boundary condition (see also Abernathey and Cessi, 2014). This allows the isopycnals to freely evolve but precludes a residual MOC, which implies that the eddy-driven MOC has to adjust such that it always balances the wind-driven MOC. Meanwhile, to explore the response of the SOMOC, in the channel model we used a sponge layer at the northern boundary to restore the

stratification (see also e.g. Abernathey et al., 2011). This allows the existence of a non-trivial residual MOC, but together with the restoring surface buoyancy condition it largely constrains the adjustment of the isopycnal structure in the channel. Therefore, there is no perfect choice of northern boundary condition to study the ACC transport and the SOMOC simultaneously in a channel model.

To overcome this boundary condition issue we need an inter-hemispheric model that includes a basin to the north of the channel, which permits explicit water mass transformations and hence a non-trivial residual MOC, while retaining the flexibility for the isopycnals to adjust. An inter-hemispheric model can represent the interaction between the Southern Ocean and other basins, which is crucial for the circulations in both places (e.g. McDermott, 1996; Nikurashin and Vallis, 2011; Close and Naveira Garabato, 2012). For example, Gnanadesikan (1999, hereafter G99) proposes an elegant conceptual model, which shows that the SOMOC helps to determine the global pycnocline depth, thus strongly affecting the global ocean stratification and circulation. This result is also supported by high-resolution numerical simulations (e.g. Wolfe and Cessi, 2010).

While much work has been done to understand the equilibrium response of the global ocean circulation to wind stress changes, significantly less has focused on the theoretical understanding of the time-dependent response. Jones et al. (2011, hereafter J11), Allison et al. (2011), and Samelson (2011) have proposed similar theories for the time-dependent response of the global pycnocline depth to changes in various factors, including the Southern Ocean surface wind stress. However, these theories all predict a multi-decadal adjustment timescale, which is significantly shorter than found by their and others' simulations (e.g. Jansen et al., 2018).

In this chapter we use an inter-hemispheric model ("the shoebox") to study both the time-dependent and the equilibrium response of the large-scale ocean circulation to changes in Southern Ocean surface wind stress. We first compare with the equilibrium results to those from the channel model simulations and discuss the impact of having the basin. We also compare the results with the G99 theory and point out its limitations, particularly with respect to

the representation of low latitude upwelling. We then investigate the time-dependent response of the global ocean circulation to sudden Southern Ocean wind stress changes. By comparing the results with the theory of J11, we find that the equilibrium scaling theories, which are used to relate transport in different model regions to the global pycnocline depth, do not hold throughout the adjustment process, which leads to the failure of the J11 theory in predicting a correct adjustment timescale. We argue that most of the drawbacks of the G99 and J11 theories can ultimately be attributed to the fact that the deep ocean stratification and its adjustment cannot be adequately captured by a single pycnocline depth.

4.2 Theories

4.2.1 Equilibrium pycnocline depth

Gnanadesikan (1999, hereafter G99) proposes an elegant two-layer model for the global pycnocline depth D, which is the model's upper layer depth (Fig. 4.1). The model considers the Southern Ocean upwelling T_s (the SOMOC), the low latitude upwelling T_u, and the northern sinking T_n (the AMOC):

$$T_s + T_u - T_n = 0. \tag{4.1}$$

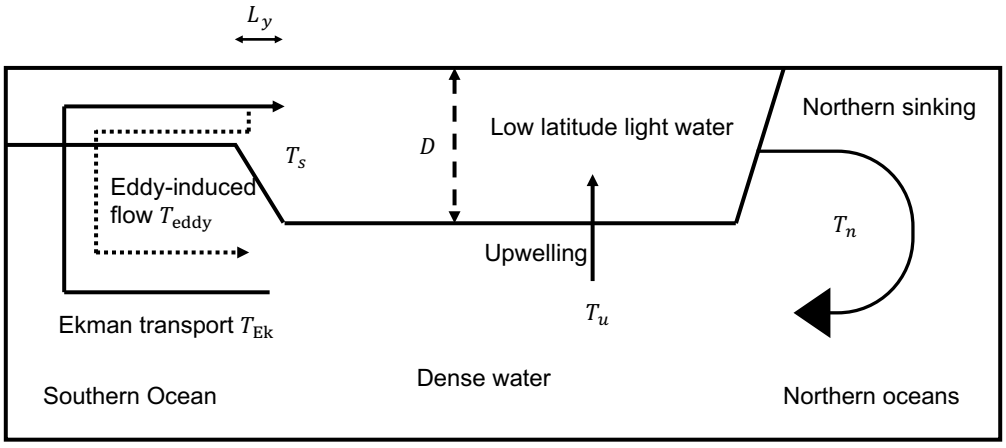

Figure 4.1: Schematic of the model by G99 (reproduced from G99).

Specifically, the Southern Ocean transport is

$$T_s \equiv T_{\mathrm{Ek}} - T_{\mathrm{eddy}}, \tag{4.2}$$

where

$$T_{\mathrm{Ek}} = \frac{\tau}{\rho |f|} L_x \tag{4.3}$$

is the wind-driven SOMOC: τ is the wind stress over the Southern Ocean, L_x the zonal extent of the ACC, ρ the density, and f the Coriolis parameter; and

$$T_{\mathrm{eddy}} = K \frac{D}{L_y} L_x \tag{4.4}$$

is the eddy-induced SOMOC, where L_y is the meridional extent of the ACC and K the effective diffusivity. The effective diffusivity is represented as

$$K = \kappa_0 \left(\frac{D}{D_0} \right)^{n-1}, \tag{4.5}$$

where κ_0 is the reference diffusivity, D_0 the reference pycnocline depth, and n a positive integer. The general form of the diffusivity in Eq. (4.5) follows J11. If $n = 1$ we retrieve the original formulation in G99 and if $n = 2$ we get an eddy parameterization similar to Visbeck et al. (1997), where the diffusivity is proportional to the isopycnal slope.

The low latitude upwelling T_u, in equilibrium, is determined by the balance between downward buoyancy diffusion and upward water mass advection

$$\partial_z \left(\kappa_v \frac{\partial b}{\partial z} \right) = w \frac{\partial b}{\partial z}, \tag{4.6}$$

where κ_v is the diapycnal diffusivity, b the buoyancy, and w the vertical velocity. Assuming that κ_v is a constant and using the scalings $w \sim T_u/A$ (A being the area of the upwelling) and

$\mathrm{d}/\mathrm{d}z \sim 1/D$ we have

$$T_u = \frac{\kappa_v A}{D}. \tag{4.7}$$

The northern sinking takes the form of

$$T_n = \frac{c g'}{f} D^2, \tag{4.8}$$

where c is a constant of proportionality and g' the reduced gravity. Notice that we have replaced the original βL_y term from G99 by f in Eq. (4.8), where β is the meridional gradient of Coriolis parameter and L_y the meridional extent across which the pycnocline shoals in the northern hemisphere. Eq. (4.8) arises from the thermal wind relation and the assumption that the northern sinking can be related to a zonal geostrophic transport in the north of the basin (see also Nikurashin and Vallis, 2012). Mathematically Eq. (4.8) is equivalent to the original formulation in G99, as long as the parameter c is re-tuned accordingly[1].

Last, to test the theory we also diagnose D from the numerical simulations, where D is computed, following G99, as

$$D = \frac{\int_{z=-H}^{0} \Delta\sigma_2 z \mathrm{d}z}{\int_{z=-H}^{0} \Delta\sigma_2 \mathrm{d}z}, \tag{4.9}$$

where $H = 4000$ m is the depth of sea floor and $\Delta\sigma_2 \equiv \sigma_2(z) - \sigma_2(\max)$, with σ_2 being the potential density referenced to $z = -2000$ m. In practice, Eq. (4.9) is computed as the average between 30°S and 30°N, where the isopycnals are largely flat. The values of the model parameters are summarized in Table 4.1, and the procedure used to determine the parameters is documented in Appendix 4.A.

4.2.2 Adjustment timescale of pycnocline depth

Several theories have been proposed to predict the adjustment timescale of pycnocline depth (J11; Allison et al., 2011; Samelson, 2011). Here we follow the formulation of J11, but we

1. See Appendix 4.A for how c is determined.

Parameter	Value	Parameter	Value
L_x	4×10^6m	L_y	1.5×10^6 m
ρ	1035 kg m^{-3}	f	1.16×10^{-4}s^{-1}
κ_0	3000 m^2 s^{-1}	D_0	794 m
κ_v	5×10^{-5} m^{2}s^{-1}	A	6.41×10^{13} m^2
g'	0.01 m s^{-2}	c	0.16

Table 4.1: Values of parameters used in our solution of the G99 model

note that all three papers suggest essentially the same scaling theory.

J11 generalizes the G99 theory by including a tendency term on the R.H.S. of Eq. (4.1), such that

$$A\frac{\mathrm{d}D}{\mathrm{dt}} = T_s + T_u - T_n. \tag{4.10}$$

Linearizing Eq. (4.10) about the equilibrium solution, such that $D(t) \equiv D_{\mathrm{eq}} + D'(t)$, where $|D'(t)| \ll |D_{\mathrm{eq}}|$ is assumed, we get the e-folding adjustment timescale for $D'(t)$ (see Appendix 4.B for the derivation)

$$t_0 = \frac{AD_{\mathrm{eq}}}{T_{\mathrm{u,eq}} + 2T_{\mathrm{n,eq}} + nT_{\mathrm{eddy,eq}}}, \tag{4.11}$$

where the subscript "eq" denotes the equilibrium solution.

4.3 Model setup

We use an idealized inter-hemispheric model to test how adding a basin may modify the conclusions from chapter 3, and to study the time-dependent response of the global ocean circulation to changes in Southern Ocean surface westerlies. We refer to this new model as the "shoebox" (Fig. 4.2). The shoebox is simply an extension of the channel we used in chapter 3, by adding a flat-bottomed basin to its north such that its northern boundary is located at 65°N, instead of 30°S. Continental slope is also added to the eastern/western/northern boundaries of the basin part, as is consistent with the channel configuration. Readers are referred to chapter 3 for a detailed description of the channel part's geometry.

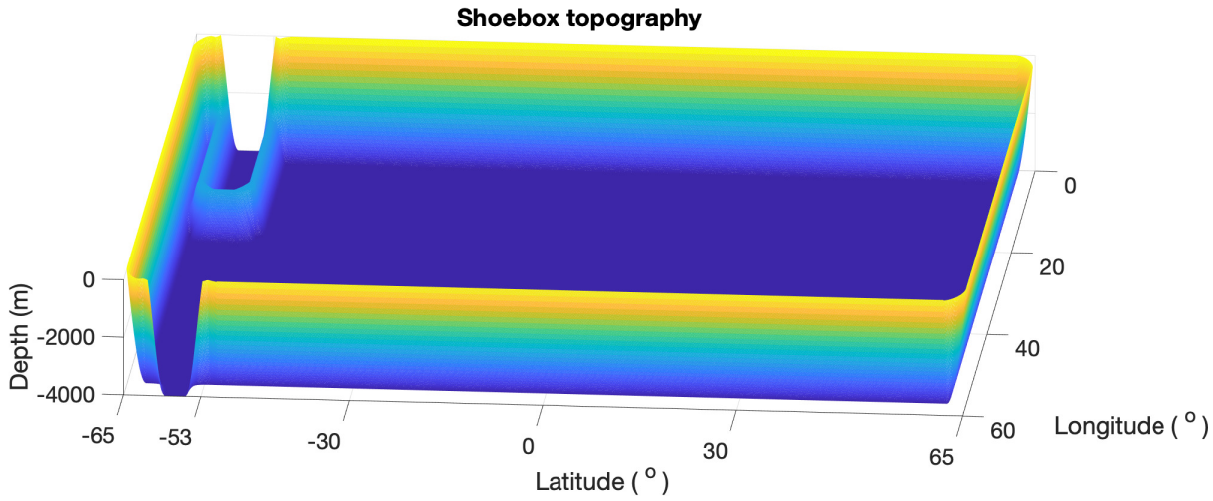

Figure 4.2: 3D view of the shoebox topography.

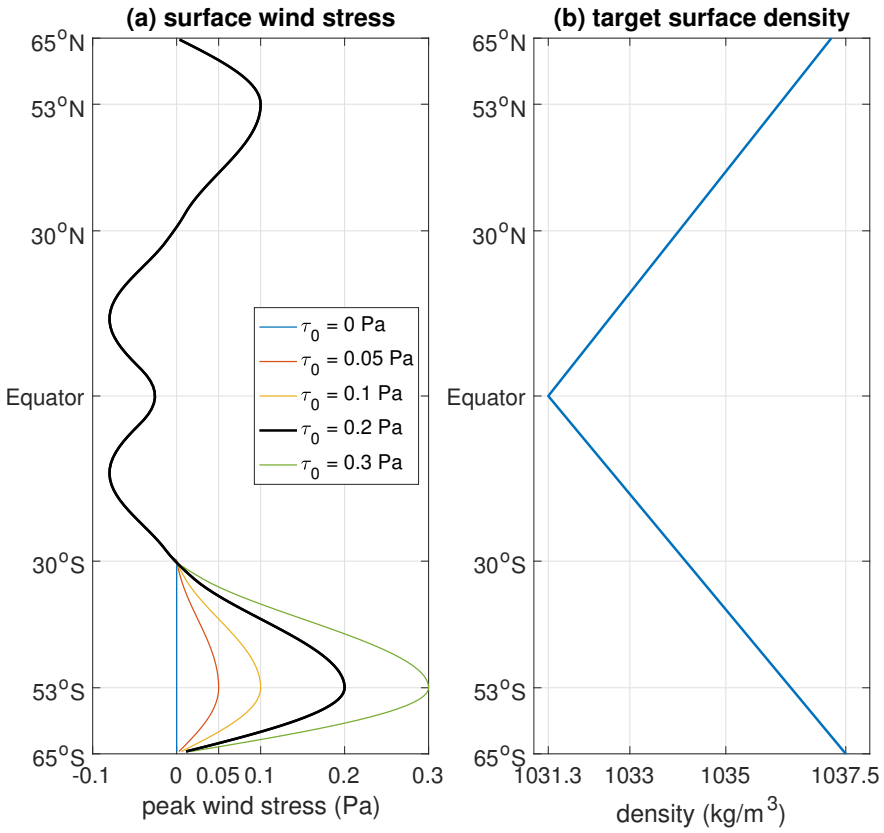

Figure 4.3: (a) Surface zonal wind stress profile. Black curve denotes the reference case. All 5 cases share the same wind stress profile north of 30^oS. (b) Target density profile for surface restoring.

Similar to the channel, the shoebox is forced at the surface by zonally symmetric eastward wind stress, which is also meridionally symmetric around the equator between 30°S and 30°N

(Panel (a) of Fig. 4.3). The surface density is restored towards an idealized profile (Panel (b) of Fig. 4.3). The densest water in the northern hemisphere is lighter than that in the southern hemisphere, to ensure Antarctic Bottom Water (AABW) forms in the southern hemisphere.

For the wind stress experiments, we first force the model with reference wind stress (Southern Ocean peak wind stress $\tau_0 = 0.2$ Pa; the thick black curve in Panel (a) of Fig. 4.3) and integrate the model to full equilibrium. We then change the Southern Ocean wind stress profile in one timestep and continue the simulation until the model equilibrates again. Both the spin-up and adjustment processes take thousands of years to complete, making the shoebox computationally too expensive to run at an eddy-permitting resolution ($1/4^\circ$ or finer). Moreover, in chapter 3 we have shown that state-of-the art eddy parameterizations are adequate in producing a similar circulation field as in the $1/10^\circ$ eddy-resolving configuration of the channel. Therefore, we choose to configure the shoebox at 1^o resolution. The Topographically modified Meso-scale Eddy Kinetic Energy (TMEKE) eddy parameterization (Jansen et al., 2019) is implemented in the shoebox, following what is documented in Appendix 3.A.2 & 3.A.3, with the only exception being that Eq. (3.21) is replaced by

$$\kappa_{GM} = l_M \sqrt{\gamma_t^2 U_e^2} + 100, \tag{4.12}$$

that is, an extra background diffusivity of 100 $\mathrm{m}^2\ \mathrm{s}^{-1}$ has been added, to reduce unrealistic variability in the basin, where κ_{GM} is otherwise too small.

We have also performed the identical simulations but with a different eddy parameterization, proposed by Visbeck et al. (1997, see Appendix 3.A.1 of chapter 3), which yields qualitatively similar results as obtained by using TMEKE. Therefore, we only show the results using TMEKE in the current chapter. The model parameters are summarized in Table 3.1.

4.4 Results

In this section we first analyze the equilibrium response of circulation to changes in Southern Ocean wind stress and compare with the results from the channel simulations and the G99 theory. We then analyze the time-dependent response of the global ocean circulation and compare with the J11 model. We show that the evolution of the SOMOC, the AMOC, and the pycnocline depth differ significantly from each other, which is inconsistent with the J11 model.

4.4.1 Equilibrium response

SOMOC

The shoebox produces a SOMOC of 0.22 Sv at 53°S under the reference wind stress of 0.2 Pa (Fig. 4.4), broadly consistent with Lumpkin and Speer (2007)[2]. The SOMOC in the shoebox is relatively insensitive to wind stress changes, increasing only ∼3.5 Sv over a wind stress range from 0 to 0.3 Pa, compared to a 10.1 Sv increase of the wind-driven MOC, consistent with the "eddy compensation" theory (Hallberg and Gnanadesikan, 2006; Viebahn and Eden, 2010). The insensitivity is caused by the sensitive responses of both the stationary and transient eddies, which are comparable in magnitude.

The shoebox and the channel share a similar SOMOC, suggesting that the channel is able to reproduce the SOMOC response with the help of the sponge layer. Slight differences remain in both the magnitude and the sensitivity of the SOMOC, dominated by the difference in the stationary eddies when the wind is weak and by the difference in the transient eddies when the wind is strong. These differences are attributed to the use of the sponge layer in the channel, which restores the stratification in the channel model towards fixed zonally symmetric stratification. In the shoebox where no such restoration occurs, the isopycnals and hence the MOC have more flexibility to adjust, resulting in more sensitive stationary and transient eddy

2. Notice that our domain is only 60° wide longitudinally, so the 0.22 Sv transport would translate into a 1.32 Sv transport for a 360° domain.

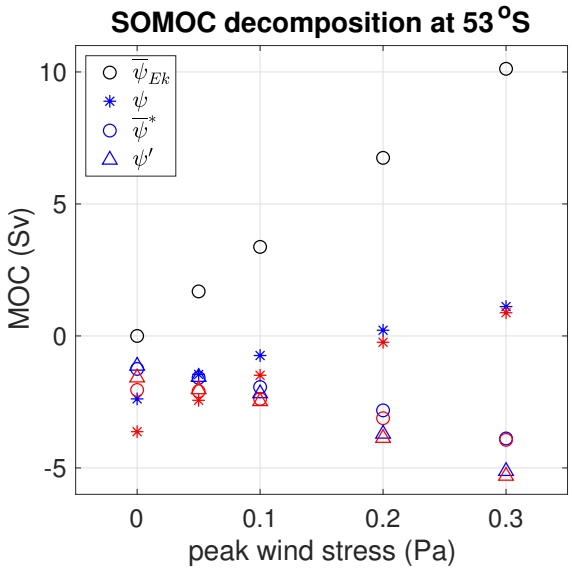

Figure 4.4: SOMOC decomposition at 53°S, where the wind stress maximizes. $\overline{\psi}_{Ek}$ denotes the Ekman transport, ψ the residual MOC, ψ^* the (resolved) stationary eddies, and ψ' the parameterized transient eddies. Blue color denotes the shoebox simulations, and red color the channel simulations with sponge layer.

responses.

ACC

The shoebox ocean has a baroclinic ACC transport of 155 Sv under the reference wind stress of 0.2 Pa (Fig. 4.5), broadly consistent with the observations (e.g. Donohue et al., 2016). The simulated ACC transport is again relatively insensitive to the wind stress changes, increasing by only 47 Sv across a wind stress range from 0 to 0.3 Pa, qualitatively consistent with the "eddy saturation" theory (Straub, 1993) and other numerical studies (e.g. Munday et al., 2013; Morrison and Hogg, 2013; Farneti et al., 2015). As a comparison, the channel has significantly underestimated the magnitude of the ACC transport, while producing a higher sensitivity, particularly in terms of relative changes.

The underestimate of the ACC transport by the channel model is consistent with the fact that isopycnals in the abyssal ocean are too flat (Fig. 4.6). The flat isopycnals are in turn caused by the channel's adiabatic northern boundary condition, which presumes a complete

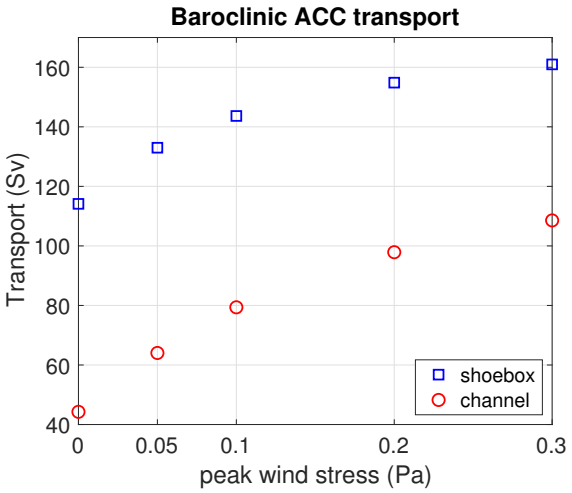

Figure 4.5: Response of the baroclinic ACC transport to wind stress changes, simulated by the shoebox and the channel.

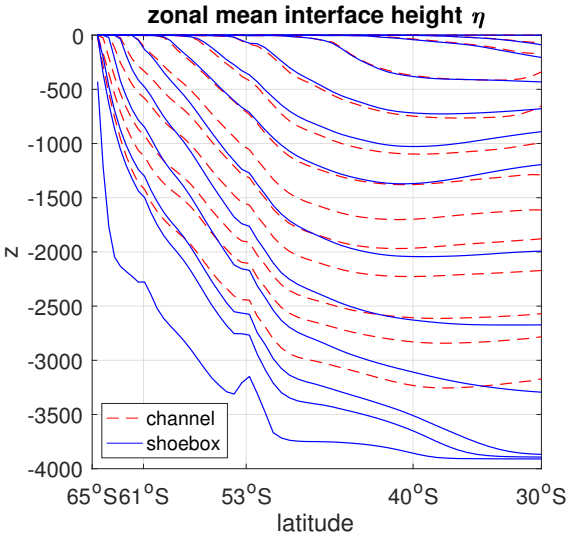

Figure 4.6: Zonal mean isopycnal interface height from the shoebox and the channel, under the reference wind stress $\tau_0 = 0.2$ Pa. To improve the presentation, only a subset of the model's isopycnal layers are plotted.

eddy compensation (Hallberg and Gnanadesikan, 2006; Viebahn and Eden, 2010); that is, the eddy-induced MOC always adjusts such that it cancels any change in the wind-driven MOC, maintaining a trivial residual MOC (except for the weak residual MOC driven by the diapycnal diffusion, as shown by Panel (b) of Fig. 4.7). This is not an issue for the upper ocean because the residual circulation from the shoebox is already very weak at the Drake Passage latitudes (53°S to 61°S); it is, however, an issue for the abyssal ocean, where the residual MOC is much weaker

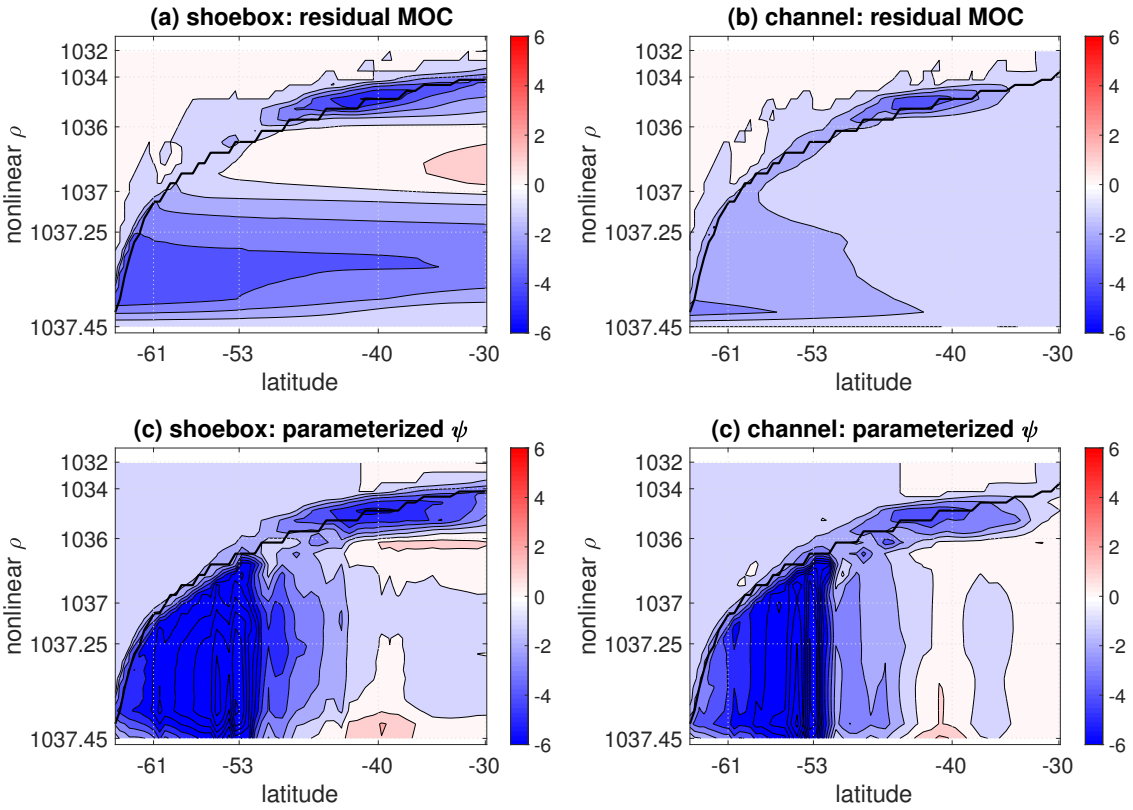

Figure 4.7: The residual MOC from the shoebox (a) and the channel (b), and the eddy-induced MOC (including both the stationary and transient eddies) from the shoebox (c) and the channel (d), under the reference wind stress $\tau_0 = 0.2$ Pa. The thick black curve denotes the bottom of the surface layer. Notice that the vertical coordinate is non-linear in σ_2. The contour interval is 1 Sv.

(in terms of absolute magnitude) in the channel than in the shoebox. The weaker abyssal MOC is realized via a weaker eddy-induced MOC. Since the eddy-transport increases with the isopycnal slope, the weaker eddy transport in the channel model requires a reduced isopycnal slope. The perfect eddy compensation also explains why the channel model overestimates the sensitivity of the ACC transport: since its eddy-induced MOC always adjusts to compensate the changes in the wind-driven MOC, its isopycnal slope, and hence the ACC transport, must be more sensitive than in the shoebox model. These results suggest, although the qualitative results found in the channel simulations appear to carry over to the global shoebox model, the quantitative results are affected by the artificial northern boundary conditions.

Comparing with the equilibrium theory of G99

The equilibrium theory of G99 (Eq. (4.1)) does a reasonably good job in predicting the pycnocline depth, yielding $D \approx 700$ m under the reference wind stress of $\tau_0 = 0.2$ Pa, compared to 800 m from the shoebox simulation (Fig. 4.8). However, the theory systematically underestimates the pycnocline depth under all wind stresses considered, while it also overestimates the response of pycnocline depth to wind stress changes. These biases are especially significant when a typical value of n is used, such as $n = 1$ (constant K) or $n = 2$ (roughly consistent with Visbeck et al. (1997) or TMEKE).

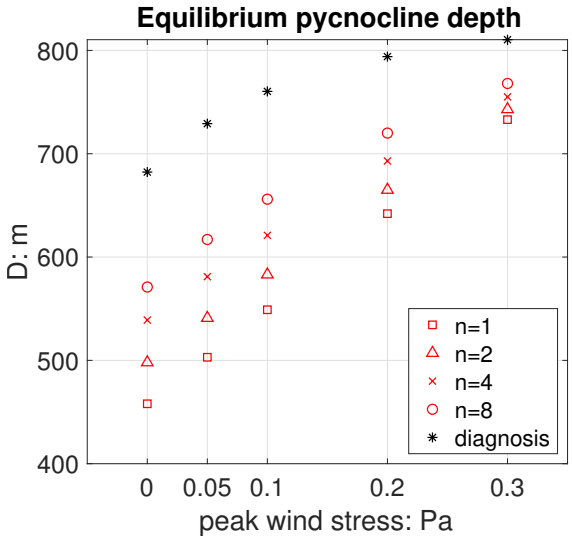

Figure 4.8: The equilibrium pycnocline depth D solved from Eq. (4.1). Also plotted is the diagnosed low latitude (averaged between 30°S $\sim$ 30°N) pycnocline depth from the shoebox simulations.

The mismatch is mainly caused by the G99 model's inaccuracy in capturing the low latitude upwelling T_u (Eq. (4.7)). Specifically, Eq. (4.7) significantly underestimates the magnitude of the upwelling, which becomes even worse when the diagnosed D_{eq} from the shoebox simulations is used to evaluate T_u (Panel (a) of Fig. 4.9). Eq. (4.7) also overestimates the sensitivity of T_u to wind stress changes (also Panel(a)). These results suggest that Eq. (4.7) is not representative of T_u: most likely it is that the pycnocline depth D is not a good measurement for the characteristic curvature of the stratification profile, which controls the advective-diffusive

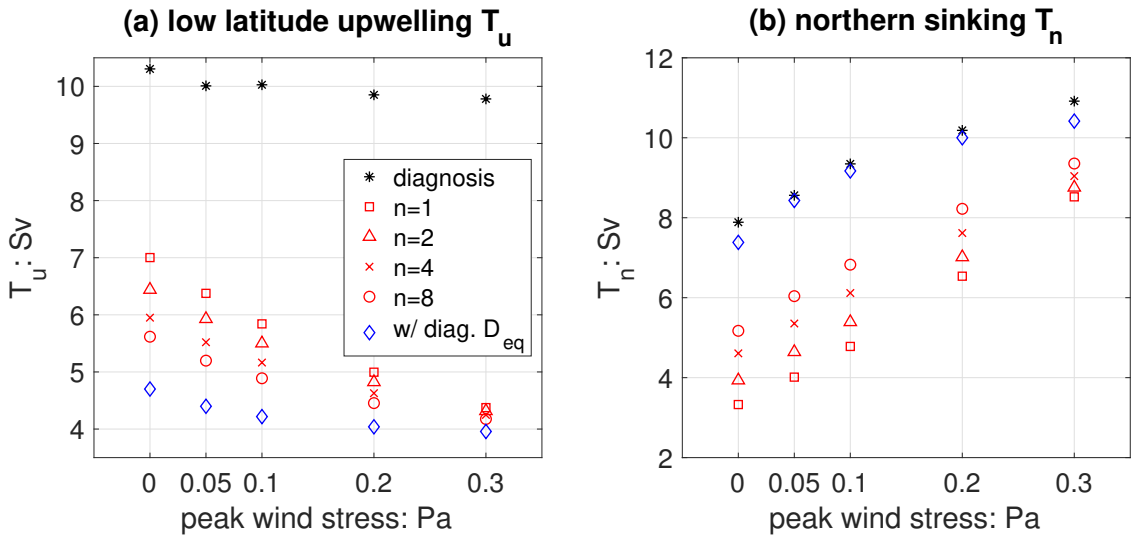

Figure 4.9: (a) Low latitude upwelling T_u, computed using Eq. (4.7), with D_{eq} predicted by Eq. (4.1) (red) and diagnosed from the shoebox simulations (blue). The upwelling area A is the model's surface area between 53°S (where T_s is evaluated) and 45°N (where T_n is evaluated). We also show the diagnosed upwelling $T_u = T_n$ (45°N)-T_s (53°S). (b) Northern sinking/AMOC, computed using Eq. (4.8), with D_{eq} predicted by Eq. (4.1) (red) and diagnosed from the shoebox simulations (blue). We also show the diagnosed AMOC at 45°N.

balance used to derive the scaling. To let the theoretical results approach the simulations, we need a significantly smaller and less sensitive depth scale, which better characterizes the isopycnals of the upper ocean, whose depth is much less sensitive to the wind stress changes than the abyssal isopycnals (Fig. 4.10). If we replace Eq. (4.7) by

$$T_u = \frac{\kappa_v A}{bD}, \tag{4.13}$$

that is, by adding a constant of proportionality $b = 0.41$ in front of D, we are able to match the theory with the simulated T_u and D much better (Fig. 4.11), although the sensitivity of T_u to wind stress changes is still overestimated.

As a contrast, Eq. (4.8) captures the equilibrium dependence of northern sinking T_n on the pycnocline depth D accurately (Panel (b) of Fig. 4.9). Comparing with the above discussion, we argue that the circulation in different regions cannot be adequately captured by a single depth scale D, which is why the G99 model fails to accurately predict the pycnocline depth and

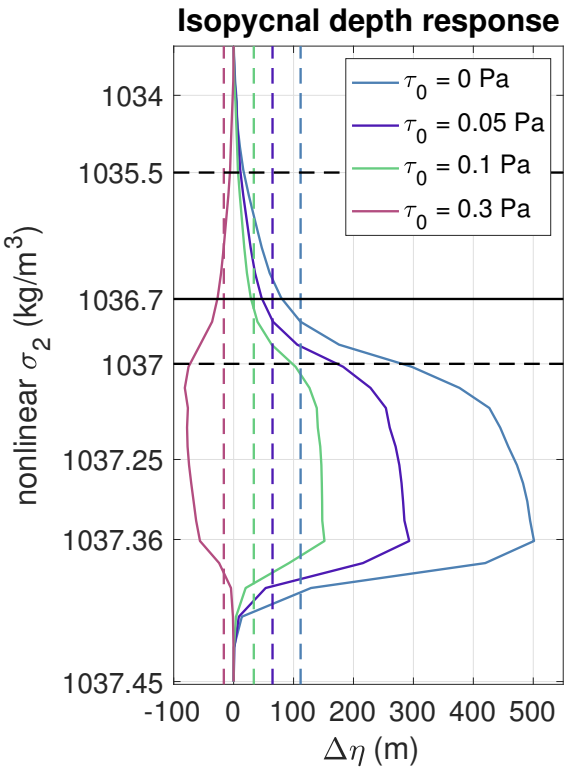

Figure 4.10: Equilibrium response of isopycnal depth under different wind stresses. All values are anomalies relative to the equilibrated reference simulation ($\tau_0 = 0.2$ Pa), which also served as the initial condition. Equilibrium response of pycnocline depth, averaged between 30°S and 30°N, are plotted as dashed vertical lines. Positive values denote shallowing of isopycnals. Thick, solid horizontal line denotes the depth of the AMOC/SOMOC center; dashed horizontal lines denote the upper/lower boundary of the AMOC/SOMOC.

its response to wind stress changes.

4.4.2 Time-dependent response

In this section we analyze the time-dependent response of several important large-scale ocean circulation features. We show that the pycnocline depth D shares a similar adjustment timescale as the baroclinic ACC transport, but the two do not evolve concurrently. We then show that both the SOMOC and the AMOC adjust much faster than the pycnocline depth or the ACC transport, suggesting different dynamics in play. We argue that the reason why the J11 model fails to predict the correct adjustment timescale for the pycnocline depth is that the equilibrium relations between the pycnocline depth and T_s, T_u, & T_n (Eqs. (4.2)(4.7)(4.8)) do not apply to

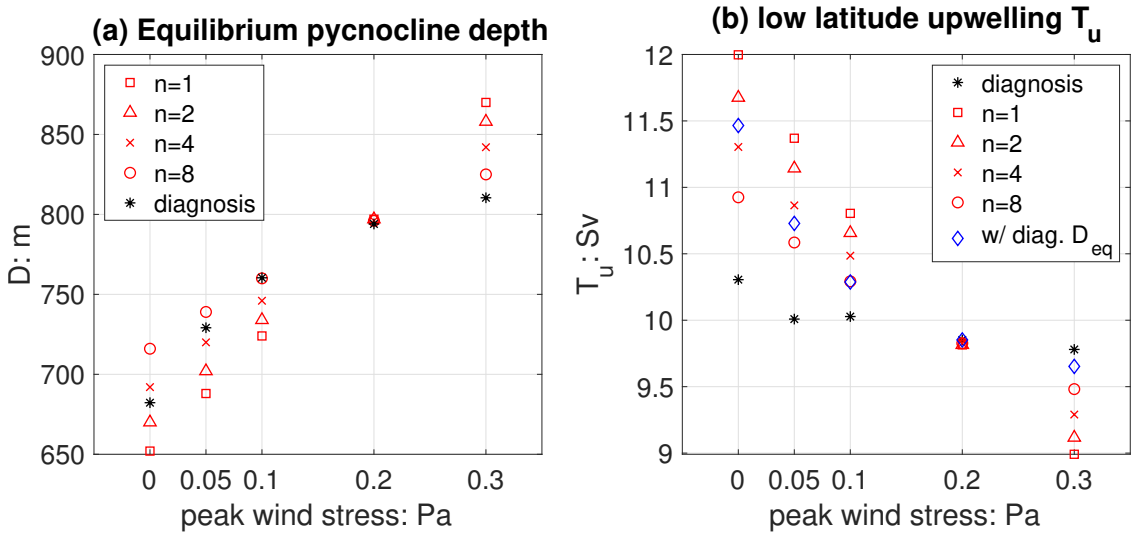

Figure 4.11: (a) Similar to Fig. 4.8 but T_u is computed according to Eq. (4.13), instead of Eq. (4.7), when solving Eq. (4.1). (b) Similar to Panel (a) of Fig. 4.9 but T_u is computed as Eq. (4.13).

the time-dependent adjustment process. In fact, the evolution of the ACC transport and MOC are governed by the adjustment of ocean stratification at different depths, which cannot be related directly to the evolution of a single pycnocline depth, D.

The temporal adjustment of the low latitude pycnocline depth D follows an exponential curve almost perfectly, with e-folding timescale on the order of centuries, and needs as long as several millennia to fully equilibrate (Fig. 4.12). The ACC transport adjustment shares a similar e-folding timescale, although the evolution is less well captured by a single exponential curve (Fig. 4.13). In fact, it seems two timescales dominate the ACC response: a short timescale over the first ∼50 years, and a multi-centennial timescale that dominates the later phase of response and can be accurately captured by an exponential curve (Fig. 4.14). The double-timescale adjustment of the ACC transport suggests that the ACC transport and pycnocline depth do not occur concurrently, as further illustrated in Fig. 4.15, which shows the temporal relation between the ACC transport and the pycnocline depth. Clearly, the scaling that $T_{\mathrm{ACC}} \sim D^2$ does not hold throughout the adjustment process, although it does capture the equilibrium relation rather accurately. The multi-decadal adjustment of the ACC transport appears to be related to the fast response of the upper ocean stratification (see Fig. 4.16), which is not adequately

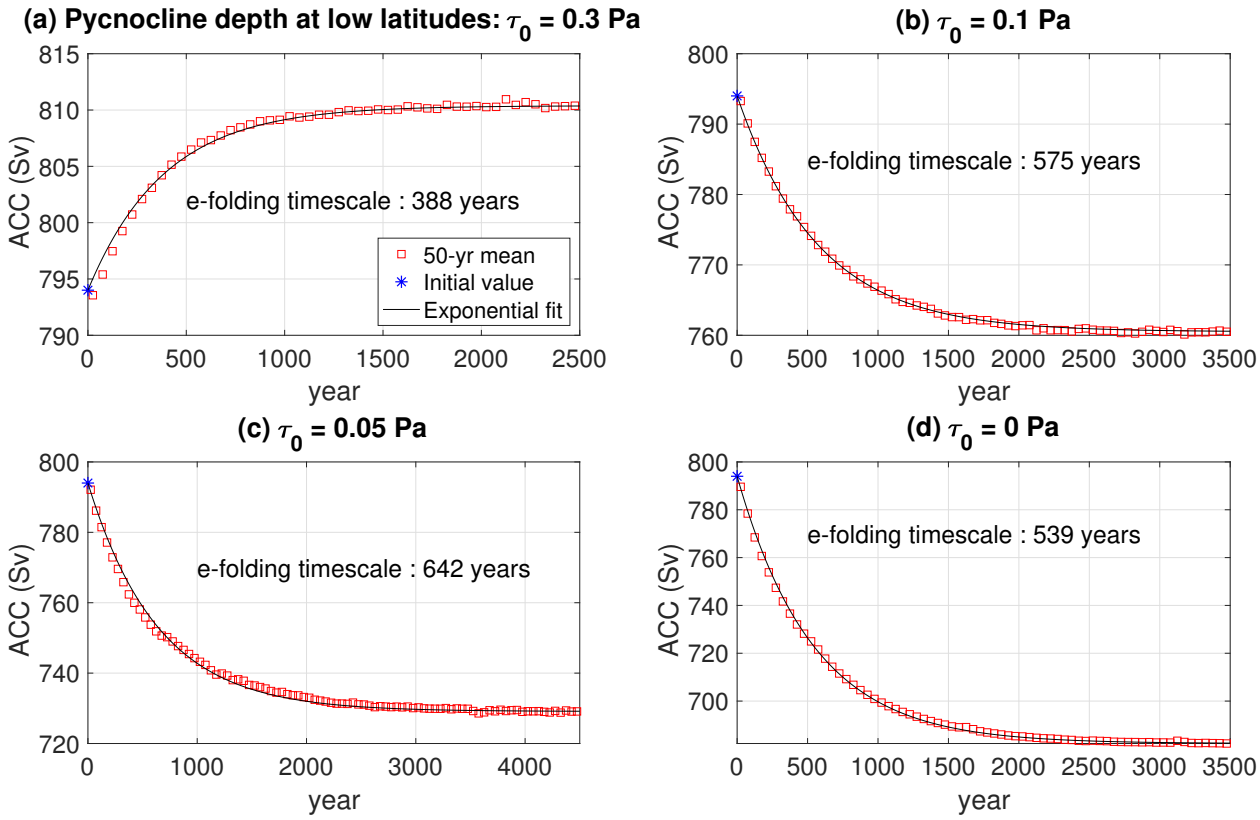

Figure 4.12: Time-dependent response of the low latitude pycnocline depth D, averaged between 30°S and 30°N, and between 5°E and 55°E, to avoid topography. A best-fit exponential curve is superimposed, with the corresponding e-folding timescale given in each panel.

reflected in the response of D, which is largely determined by the deep ocean stratification.

Both the magnitude of the SOMOC and AMOC adjust much faster than the pycnocline depth and ACC transport (Figs. 4.17, 4.18). In fact, the bulk response of the SOMOC takes place in about 50 years, and the AMOC response takes a bit longer but still less than 200 years. This quick response indicates that the adjustment mechanism of the SOMOC and AMOC differs fundamentally from that of the pycnocline depth. The scaling of T_n (Eq. (4.8)) does not capture the temporal relation of the AMOC and pycnocline depth during the adjustment process, although it is skillful in capturing the equilibrium relation between the two (Fig. 4.19).

It appears that the adjustment timescale of MOC's magnitude is consistent with the adjustment timescale of the isopycnal depth at the center of the MOC. The isopycnal depth at the center of the AMOC (σ_2=1036.7 kg m^{-3}) reaches its equilibrium value in about 100 years

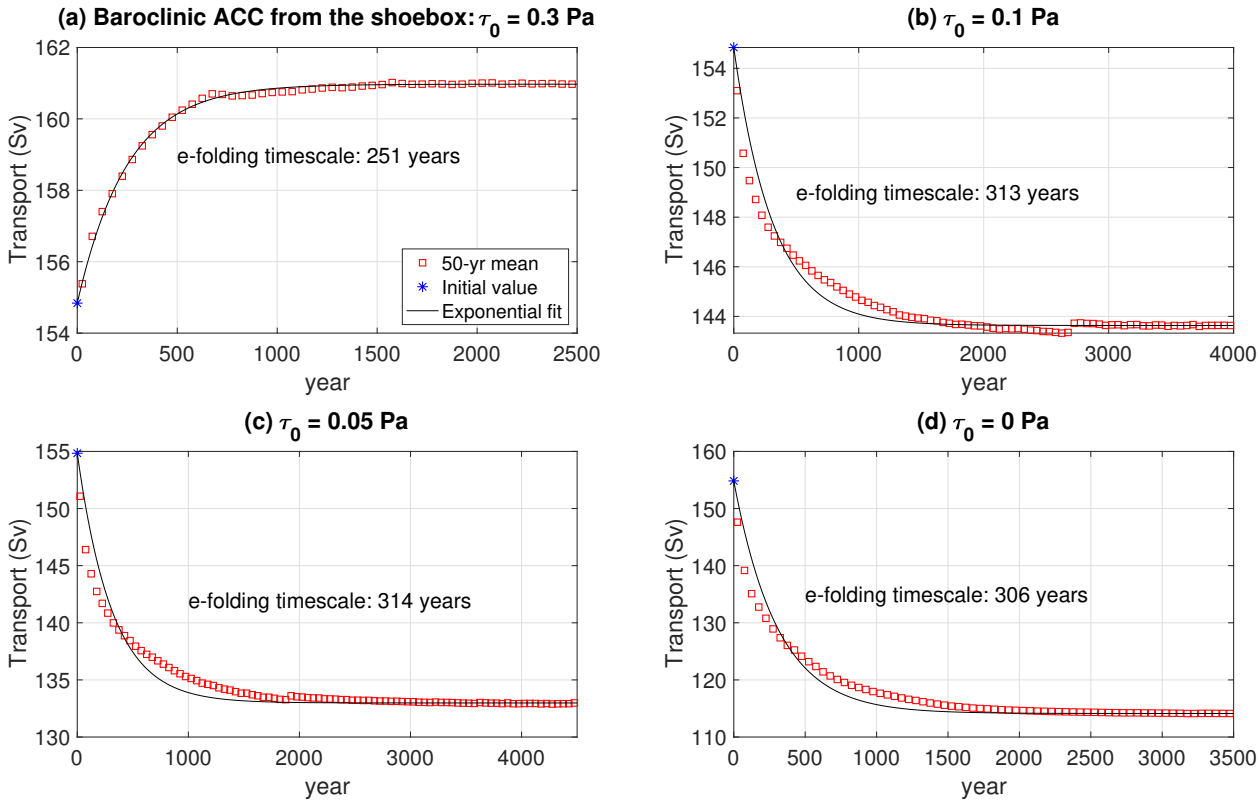

Figure 4.13: Similar to Fig. 4.12 but for the response of the ACC transport.

(Fig. 4.16). It is the slow adjustment of the abyssal layers, those denser than the lower boundary of the AMOC ($\sigma_2 = 1037$ kg m^{-3}), that contribute significantly to the slow adjustment of the pycnocline depth, the latter being a bulk measurement of the stratification across the whole water column. But the AMOC seems not to be affected much by these deep ocean isopycnals. The distinction between the upper ocean adjustment (which dominates MOC strength) and abyssal adjustment (which dominates the diagnosed pycnocline depth) appears to explain why Eq. (4.8) breaks down throughout the time-dependent adjustment process.

It is now helpful to take a look back at one important hypothesis we made for the channel model in chapter 3. When studying the response of the SOMOC in the channel, we applied a sponge layer, and postulated that using a sponge only captures the transient (decadal or shorter timescale) response. According to the results shown above, this hypothesis seems not to hold. In fact, the SOMOC adjusts so fast that only in the 2nd decade after the wind stress change, its magnitude is already very close to its final, equilibrium magnitude (Fig. 4.17). In other

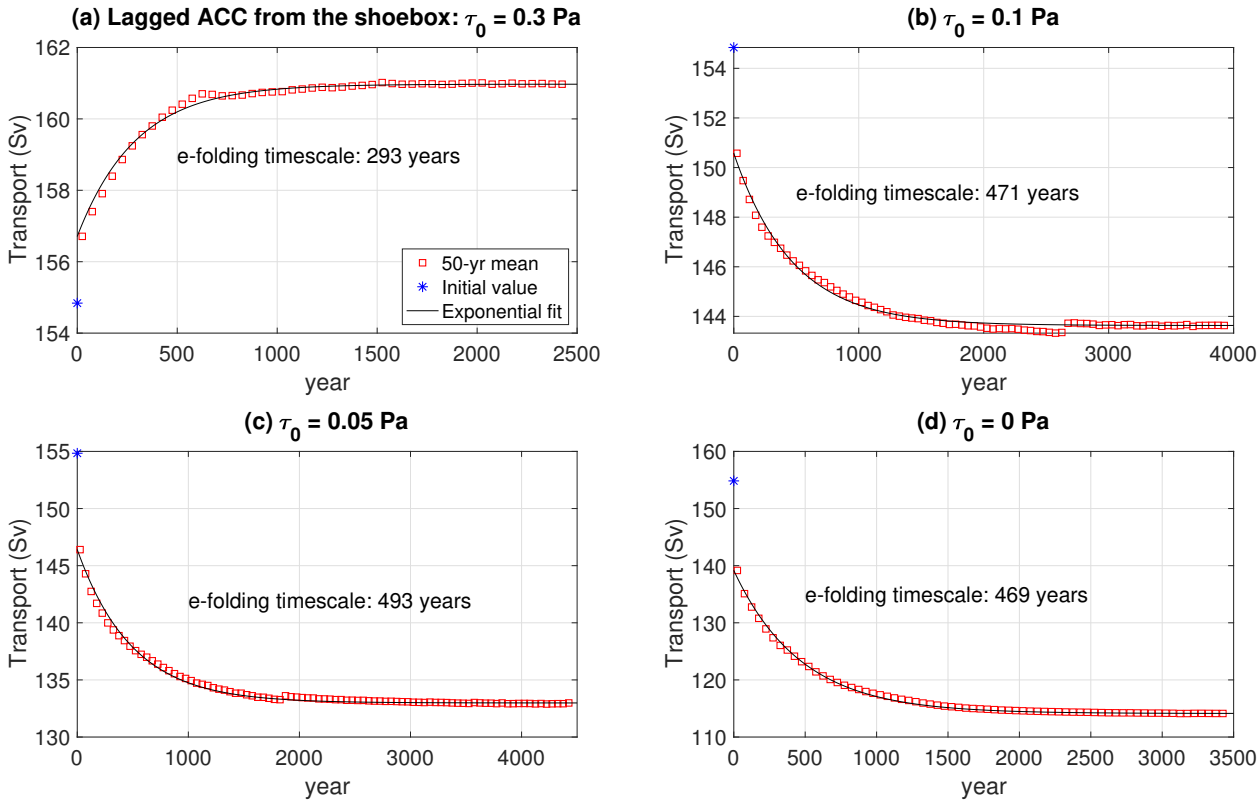

Figure 4.14: Similar to Fig. 4.13 but the exponential curve is fitted only to the data 50 years after the wind stress change. Refer to the text for more details.

words, the SOMOC's "transient" response is already very similar to its equilibrium response. Therefore, the hypothesis fails, in that the channel model can reasonably capture the SOMOC response to the wind stress changes on both decadal and equilibrium time-scales.

Comparing with the time-dependent theory of J11

The theory of J11 (Eq. (4.11)) predicts a multi-decadal adjustment timescale for the pycnocline depth (red marks in Fig. 4.20), much shorter than the multi-centennial timescale diagnosed from the shoebox simulations (Fig. 4.12). This result is not improved by replacing the predicted D_{eq} with the diagnosed D_{eq} (blue marks in Fig. 4.20). In fact, even if we compute Eq. (4.11) using all diagnosed quantities of D_{eq}, T_u, T_{eddy}, and T_n, we still only get a multi-decadal adjustment timescale (black marks in Fig. 4.20). We argue that this is because the equilibrium relations between the pycnocline depth and T_{eddy}, T_u, & T_n do not apply to the time-dependent

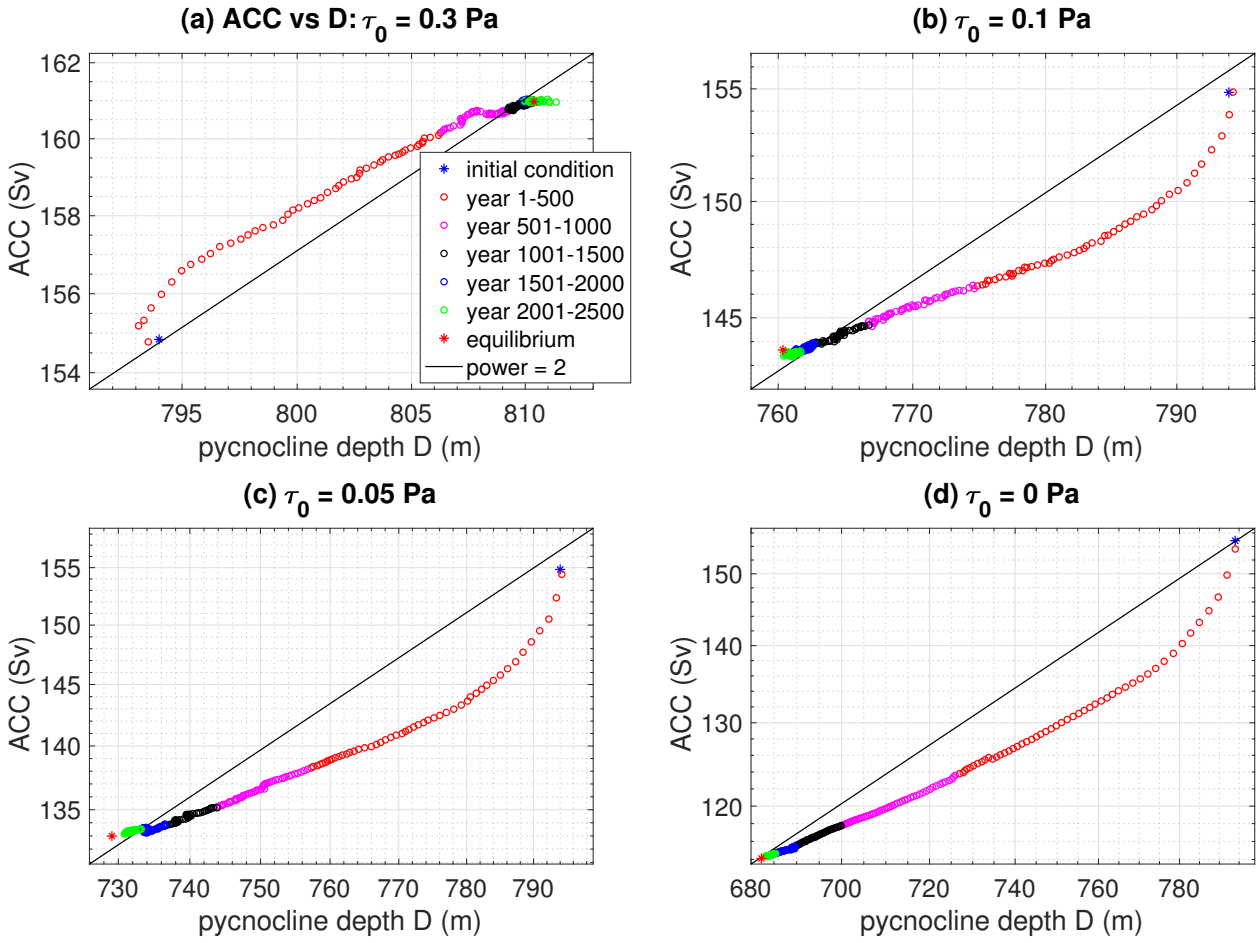

Figure 4.15: Time-dependent response (averaged every 10 years) of the baroclinic ACC transport vs. the low latitude pycnocline depth D, on a log-log scale. Data points are colored according to the time period after the wind stress change. The power dependence of $T_{\mathrm{ACC}} \sim D^2$ is added as a reference.

adjustment process. In particular, the adjustment of T_u and T_n relies more on the stratification change in the upper ocean, which adjusts much faster than D. To develop a more accurate theory for the time-dependent response of ocean circulations we need to consider these depth-dependent relations.

4.5 Conclusions

In this work we have used an inter-hemispheric "shoebox" ocean model to study the time-dependent response of the large-scale ocean circulation to changes in Southern Ocean surface

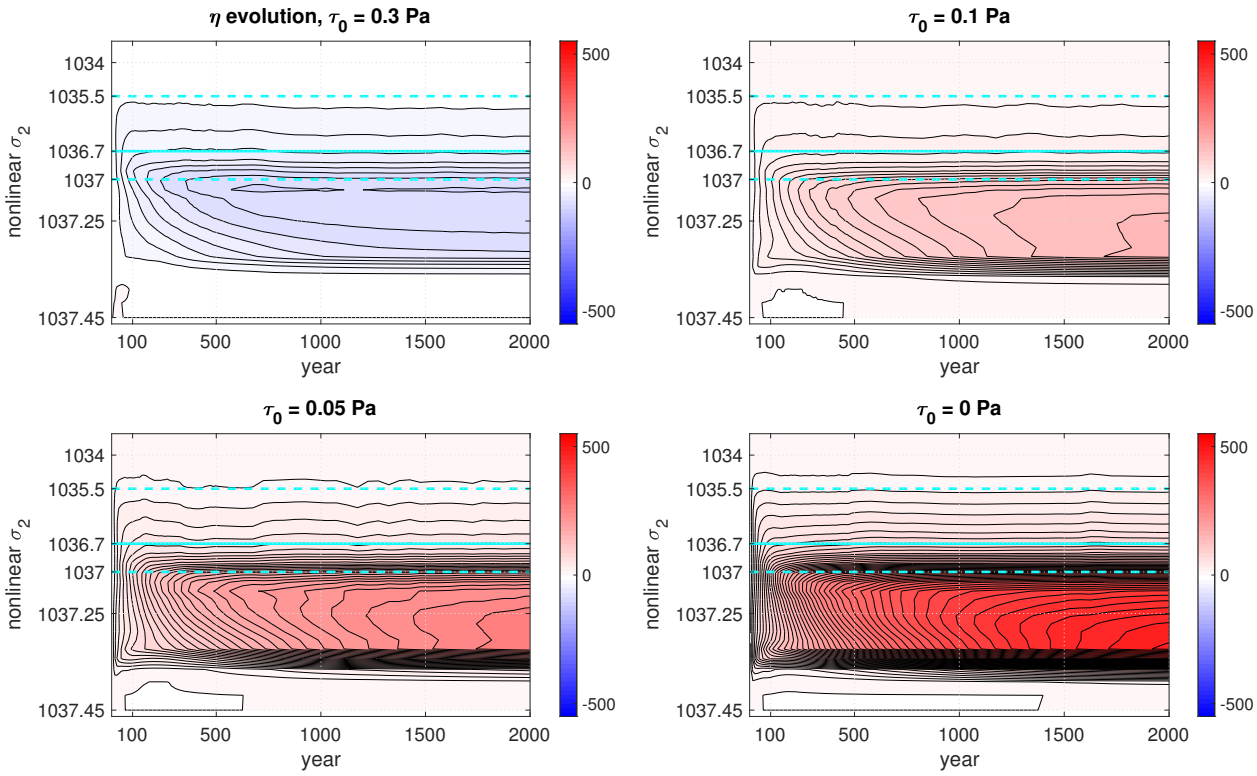

Figure 4.16: Hovmöeller diagram of the isopycnal interface height anomaly, averaged between 30°S and 30°N. The isopycnal at the center of the AMOC is indicated by the solid cyan line; the isopycnals at the upper and lower boundaries of the AMOC are indicated by the dashed cyan lines. Negative values denote a deepening of the isopycnals. The calculation is based on 10-year averages for the first 500 years, after which 50-year averages are used. The contour interval is 10 m.

wind tress. We first investigated the equilibrium response of the SOMOC, the ACC transport, and the global pycnocline depth to the wind stress changes, and compared with the results from two channel model setups (one with an adiabatic northern boundary condition and one with a sponge layer) as well as the G99 theory. We find the channel with the sponge and the shoebox ocean share a similarly insensitive response of the SOMOC, suggesting that using a sponge layer to simulate the SOMOC in a channel model is effective. We also find that, compared to the shoebox ocean, the adiabatic channel has a much weaker yet more sensitive ACC transport, due to its adiabatic northern boundary condition that presumes a complete eddy compensation. By comparing the shoebox simulations with the G99 theory, we find that the theory underestimates the magnitude but overestimates the sensitivity of the pycnocline

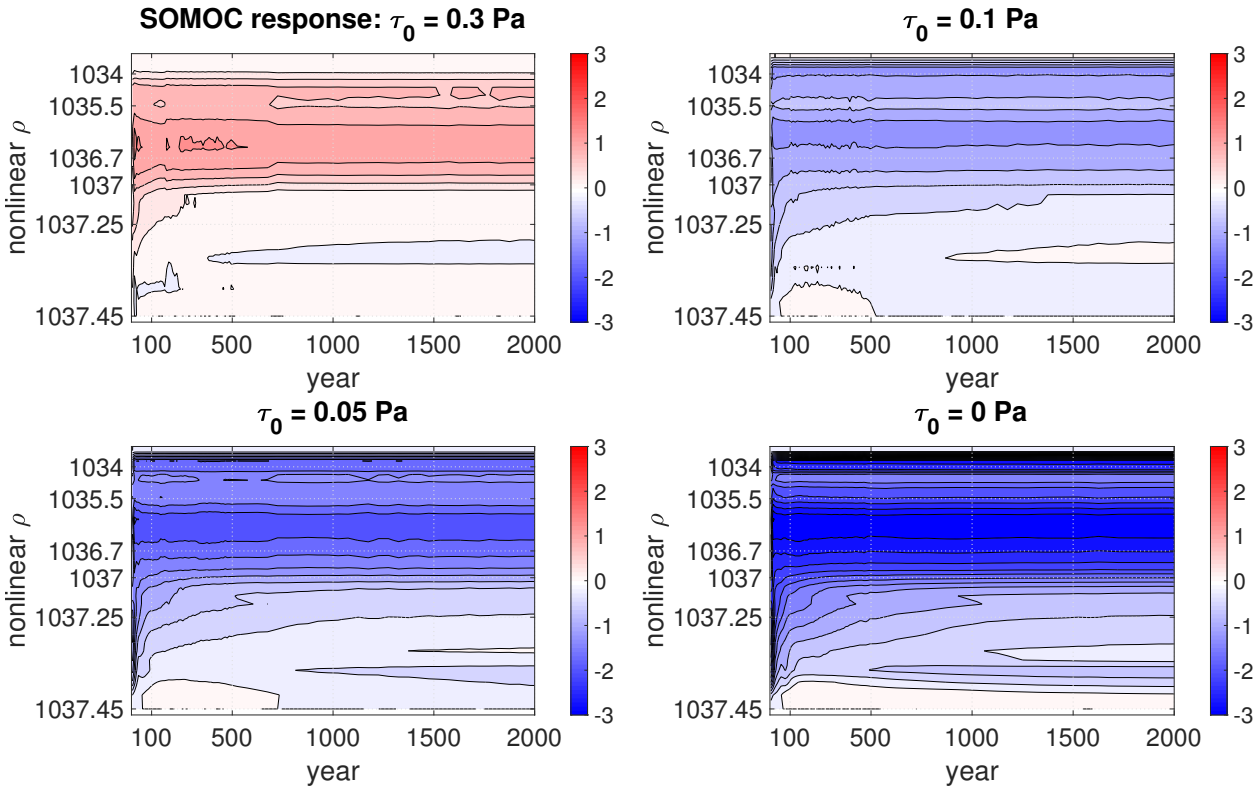

Figure 4.17: Hovmöeller diagram of the SOMOC anomaly, evaluated at 30°S. The anomalies are computed as relative to the equilibrated reference simulation with $\tau_0 = 0.2$ Pa, which served as the initial condition. The calculation is based on 10-year averages for the first 500 years, after which 50-year averages are used. The contour interval is 0.25 Sv.

depth, because the pycnocline depth is not a good proxy for the depth scale of either the low latitude upwelling or the Southern Ocean eddy-induced transport. A smaller and less sensitive depth scale fits better with the upwelling, while a larger and more sensitive depth scale is needed to match the eddy transport.

We then investigated the time-dependent response of the global pycnocline depth, the ACC, and the MOC. We find a multi-centennial e-folding adjustment timescale for the pycnocline depth and the ACC transport, and a multi-decadal timescale for the MOC. We argue that the difference is because the magnitude of the MOC seems to only depend on the upper ocean stratification, while the responses of the pycnocline depth and the ACC transport also involve the adjustment of deep ocean stratification. The different adjustment timescales cannot be captured by existing two-layer theoretical models that include only one depth scale. Last, we find

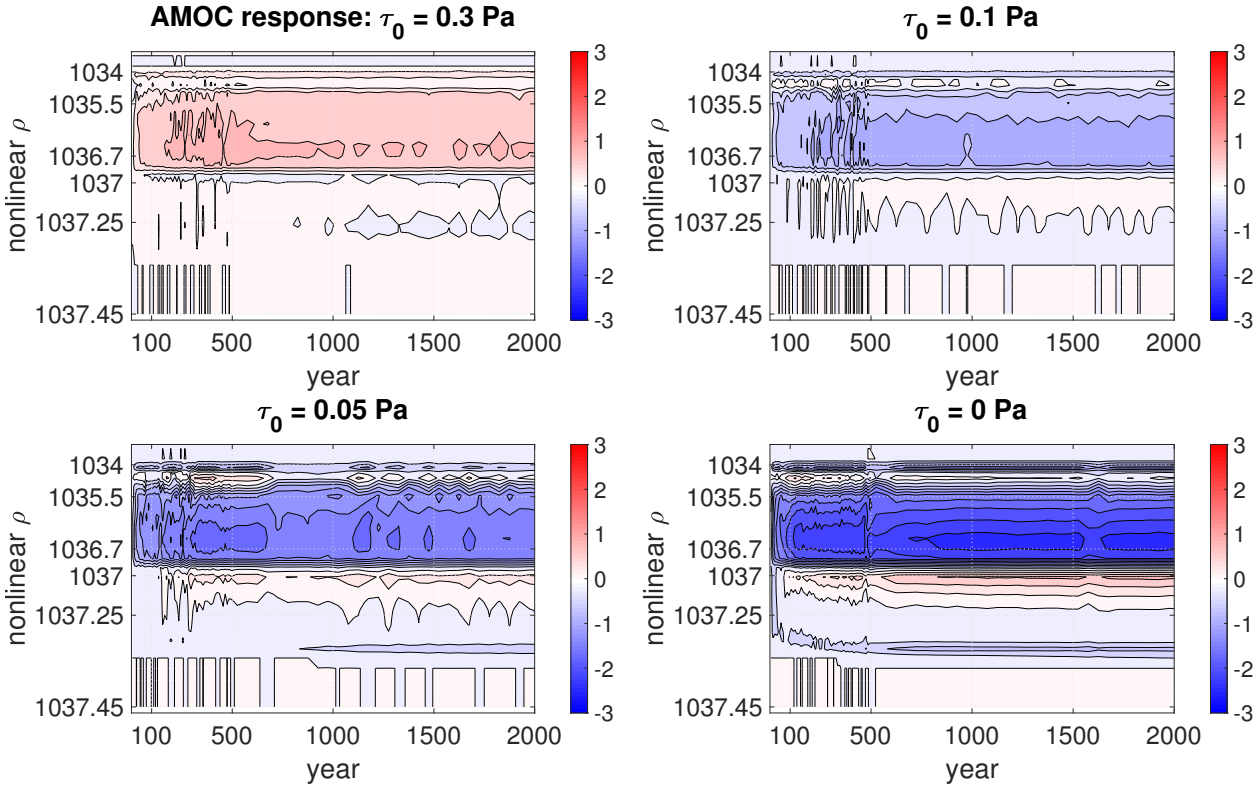

Figure 4.18: Same as Fig. 4.17 but for the AMOC, evaluated at 45°N.

that the time-dependent relations between the pycnocline depth and the ACC/SOMOC/AMOC differ from their equilibrium relations, because the adjustment of the ACC/SOMOC/AMOC depends on the adjustment of the stratification at different depths, which occurs at different timescales. These findings suggest that to understand the time-dependent adjustment of the large-scale ocean circulations, we need to consider the effect of the depth-dependent change in the stratification, which may provide an avenue to improve the existing theories.

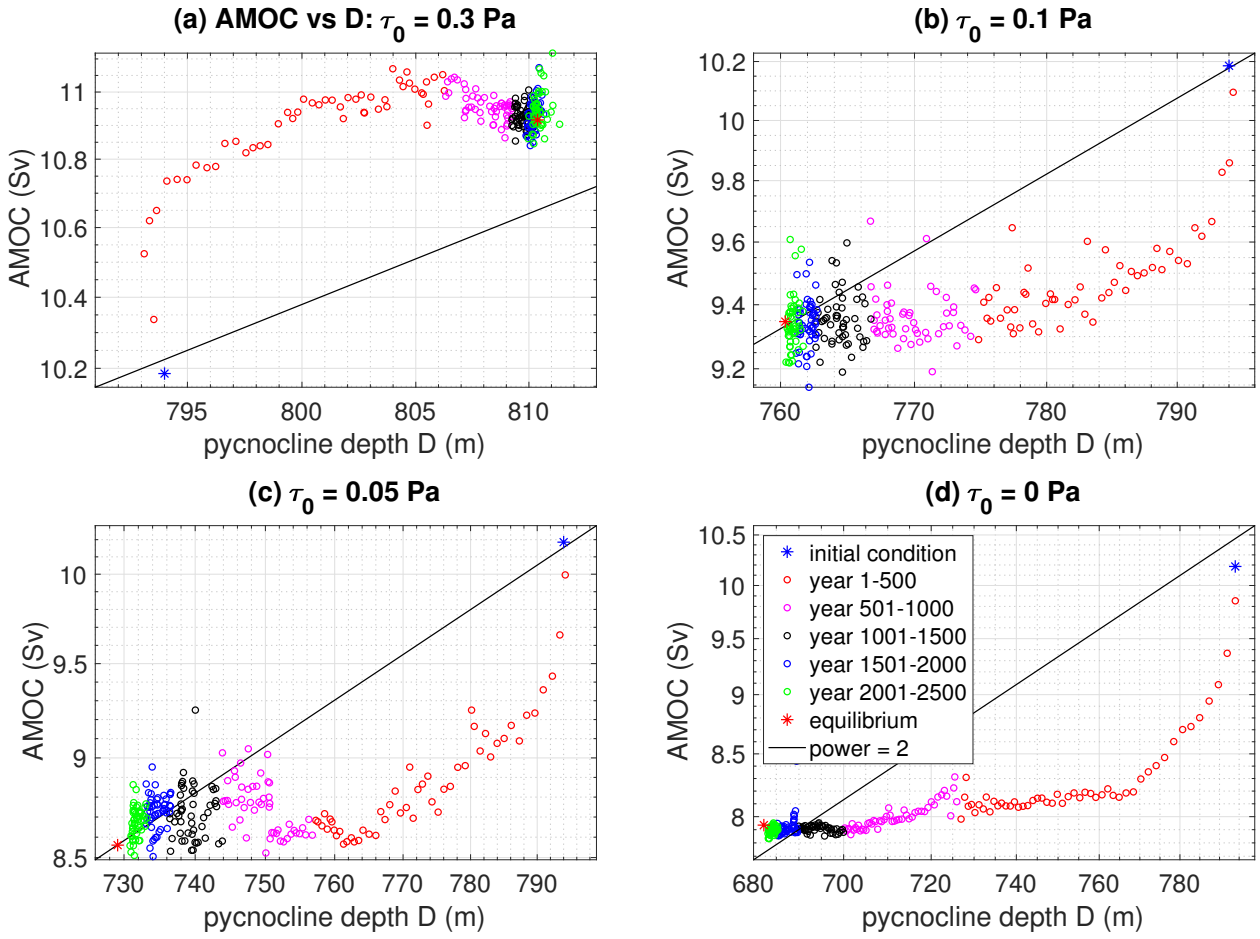

Figure 4.19: Similar to Fig. 4.15 but between the AMOC (at 45°N) and the pycnocline depth.

Appendix 4.A Tuning G99 model parameters

There are three parameters in the model of G99 that need to be determined: the coefficient c (Eq. (4.8)), the reference diffusivity κ_0, and the reference pycnocline depth D_0 (both appear in Eq. (4.4)). $c = 0.16$ is easily determined by matching Eq. (4.8) with the diagnosed AMOC at 45°N from the shoebox simulation under the reference wind stress of $\tau_0 = 0.2$ Pa, which is 10 Sv.

It is less straightforward to determine κ_0 and D_0, since we only have one equality (matching Eq. (4.4) with the diagnosed eddy-induced MOC) but two free parameters. Our strategy is to choose D_0 such that it matches the shoebox simulation at the reference wind stress, i.e. $D_0 = D_{\text{eq}}|_{\tau_0=0.2\text{Pa}}$. With this, we find that $\kappa_0 = 3000$ m^{2}s^{-1} yields the best fit with the diag-

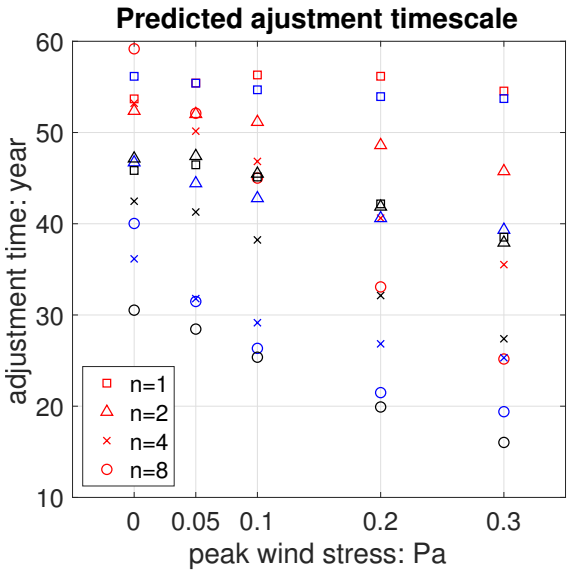

Figure 4.20: Predicted adjustment timescale using Eq. (4.11). Red marks denote the timescale computed using the predicted D_{eq}, by solving Eq. (4.1); blue marks denote the timescale computed using the diagnosed D_{eq} from the shoebox simulations; black marks denote the timescale computed using the diagnosed D_{eq}, T_{eddy}, T_u, and T_n from the shoebox simulations.

nosed T_{eddy} from the shoebox simulations. This value is somewhat larger than the diagnosed stationary + transient diffusivity (i.e. $\kappa^y_{\text{tr}} + \kappa^y_{\text{st}}$; see chapter 3) of 2092 $\text{m}^2\ \text{s}^{-1}$ averaged over the Southern Ocean domain under the reference wind stress.

Appendix 4.B The adjustment timescale for the pycnocline depth in J11 theory

Assuming that D deviates only slightly from D_{eq} at any time t throughout the adjustment process, we write $D(t) = D_{\mathrm{eq}} + D'(t)$ and substitute into Eq. (4.10) to have

$$\begin{aligned}
A\frac{\mathrm{d}D'}{\mathrm{dt}} &= \frac{\tau L_x}{\rho|f|} - \frac{L_x\kappa_0}{L_y D_0^{n-1}}(D_{\mathrm{eq}}+D')^n + \frac{\kappa_v A}{D_{\mathrm{eq}}+D'} - \frac{Cg'}{f}(D_{\mathrm{eq}}+D')^2 \\
&= T_{\mathrm{Ek,eq}} - T_{\mathrm{eddy,eq}}(1+\frac{D'}{D_{\mathrm{eq}}})^n + T_{\mathrm{u,eq}}(1+\frac{D'}{D_{\mathrm{eq}}})^{-1} - T_{\mathrm{n,eq}}(1+\frac{D'}{D_{\mathrm{eq}}})^2 \\
&\approx T_{\mathrm{Ek,eq}} - T_{\mathrm{eddy,eq}}(1+\frac{nD'}{D_{\mathrm{eq}}}) + T_{\mathrm{u,eq}}(1-\frac{D'}{D_{\mathrm{eq}}}) - T_{\mathrm{n,eq}}(1+\frac{2D'}{D_{\mathrm{eq}}}) \\
&= \left(T_{\mathrm{Ek,eq}} - T_{\mathrm{eddy,eq}} + T_{\mathrm{u,eq}} - T_{\mathrm{n,eq}}\right) - \left(nT_{\mathrm{eddy,eq}} + T_{\mathrm{u,eq}} + 2T_{\mathrm{n,eq}}\right)\frac{D'}{D_{\mathrm{eq}}} \\
&= -\left(nT_{\mathrm{eddy,eq}} + T_{\mathrm{u,eq}} + 2T_{\mathrm{n,eq}}\right)\frac{D'}{D_{\mathrm{eq}}}, \qquad (4.14)
\end{aligned}$$

where we have applied Eq. (4.1) and discarded the higher order terms. Eq. (4.14) can be rewritten as

$$\frac{\mathrm{d}D'}{\mathrm{dt}} = -\frac{T_{\mathrm{u,eq}} + 2T_{\mathrm{n,eq}} + nT_{\mathrm{eddy,eq}}}{AD_{\mathrm{eq}}}\,D', \qquad (4.15)$$

whose solution is

$$D'(t) = D'(t=0)\exp\left[-t\cdot\frac{T_{\mathrm{u,eq}} + 2T_{\mathrm{n,eq}} + nT_{\mathrm{eddy,eq}}}{AD_{\mathrm{eq}}}\right], \qquad (4.16)$$

which gives the e-folding adjustment timescale of Eq. (4.11).

CHAPTER 5

CONCLUSIONS

Geostrophic turbulent eddies are crucial in Earth's oceans for transporting and mixing physical properties and chemical/biological tracers. They are ubiquitous in Earth's oceans but are particularly active and important in the Southern Ocean. The Southern Ocean circulation is also fundamentally driven by surface wind stress, which has been increasing for decades. The intertwined impact by the eddies and wind stress makes it difficult to fully understand the Southern Ocean circulation, which also significantly interacts with other oceans on Earth.

In this dissertation we first present a new theory for the meso-scale eddy diffusivity by studying mixing in barotropic β-plane turbulence, which helps us better understand meso-scale eddy transport in Earth's oceans. We then test several state-of-the-art eddy parameterizations in idealized channel models, by investigating the equilibrium response of Southern Ocean circulation to changes in surface wind stress. We also analyze how topography modifies this response, and how well the parameterizations capture this modification. Finally, we use an idealized inter-hemispheric model to study both the equilibrium and time-dependent responses of the global ocean circulation to the changes in Southern Ocean wind stress, and compare the results with the channel model simulations as well as previous theories.

Our main findings and takeaways are,

- Barotropic β-plane turbulence with a quadratic bottom drag can be divided into 3 regimes, depending on the relative importance of β versus bottom friction: a β regime, a friction regime, and a transition regime in between. Depending on the regime, it is β, bottom friction, or both β and friction that constrain the eddy diffusivity, and thereby turbulent mixing.

- An approximate solution for the eddy diffusivity in barotropic β-plane turbulence can be analytically found by treating the non-linear eddy-eddy interactions as a stochastic forcing and a linear damping. The solution compares accurately with eddy-resolving

simulations, and echoes with previous findings that Rossby waves suppress turbulent mixing by their relative motions to the mean flow. The theory unifies previous arguments and reduces to the known scaling relations in the appropriate limit regimes.

- In an idealized flat bottom channel model for the Southern Ocean, compared to eddy-resolving simulations, coarse resolution simulations using state-of-the-art eddy parameterizations significantly overestimate the response of ACC transport to surface wind stress changes, due to an underestimate of the transient eddy diffusivity; the SOMOC response is reasonably well reproduced by the coarse resolution simulations.

- When topography is included in the channel model, it significantly suppresses the responses of the ACC transport and SOMOC to wind stress changes. This suppression is well reproduced by coarse resolution simulations, resulting from an appropriate representation of the stationary eddies, which dominate over the transient eddies. Stationary eddies enhance turbulent mixing by elongating contours of mixing and sharpening the gradients across contours of mixing.

- Due to the key role played by resolvable standing meanders, coarse resolution GCMs with eddy parameterizations (even simple ones such as a constant GM diffusivity) may be able to capture the equilibrium Southern Ocean response to wind stress changes much better than indicated by studies using more idealized flat bottom models.

- Idealized channel models with an adiabatic northern boundary condition underestimate the magnitude of the ACC transport while overestimating its response to surface wind stress changes, even when topography is included and the eddies are faithfully represented. This inaccuracy is due to the use of the adiabatic northern boundary condition, which presumes a complete eddy compensation. Idealized channel models with a restoring northern boundary condition reproduce a realistic SOMOC response.

- The theory for the global pycnocline depth by Gnanadesikan (1999) underestimates

the pycnocline depth while overestimating its sensitivity to Southern Ocean wind stress changes, because the theory does not accurately describe low latitude upwelling.

- The pycnocline depth and the ACC transport need several millennia to fully equilibrate, while the magnitude of the MOC adjusts in only a few centuries. The difference is because the adjustment of the MOC only depends on the upper ocean stratification, while the pycnocline depth and the ACC transport are also sensitive to the deep ocean stratification, which adjusts more slowly. The different adjustment timescales cannot be captured by existing two-layer theoretical models that include only one depth scale.

- The equilibrium relations between the pycnocline depth and the ACC and MOC break down during the transient adjustment process, because the ACC and MOC depend on the adjustment of ocean stratification at different depths, which occur at different timescales. This depth-dependency explains why previous theories predict a too short adjustment timescale for the pycnocline depth. An improved theory will need to consider the depth-dependence of deep ocean stratification adjustment.

The results of this thesis are expected to contribute to improved global ocean and climate simulations and increased confidence in climate projections. The theoretical work in chapter 2 will inform future developments of improved ocean eddy parameterizations, and the direct testing of state-of-the-art eddy parameterizations in chapter 3 will inform parameterization choices for global climate models. Improved eddy parameterizations will help GCMs to better project future climate, reconstruct past climate, and explore climates of other planets. The results of chapter 3 and 4 facilitate comparisons between global ocean GCMs and various idealized models, by highlighting the role of topography, boundary conditions in regional models, and time- & depth-dependence of circulation responses, thereby explaining apparent discrepancies between previous studies and increasing our confidence in climate model projections.

REFERENCES

Abernathey, R., and P. Cessi, 2014: Topographic enhancement of eddy efficiency in baroclinic equilibration. *J. Phys. Oceanogr.*, **44 (8)**, 2107–2126, doi:10.1175/JPO-D-14-0014.1.

Abernathey, R., J. Marshall, and D. Ferreira, 2011: The dependence of southern ocean meridional overturning on wind stress. *J. Phys. Oceanogr.*, **41 (12)**, 2261–2278, doi:10.1175/JPO-D-11-023.1.

Allison, L., H. Johnson, and D. Marshall, 2011: Spin-up and adjustment of the antarctic circumpolar current and global pycnocline. *J. Mar. Res.*, **69**, 167–189, doi:10.1357/002224011798765330.

Bishop, S. P., P. R. Gent, F. O. Bryan, A. F. Thompson, M. C. Long, and R. Abernathey, 2016: Southern ocean overturning compensation in an eddy-resolving climate simulation. *J. Phys. Oceanogr.*, **46 (5)**, 1575–1592, doi:10.1175/JPO-D-15-0177.1.

Böning, C., A. Dispert, M. Visbeck, S. Rintoul, and F. Schwarzkopf, 2008: The response of the antarctic circumpolar current to recent climate change. *Nat. Geosci.*, **1**, doi:10.1038/ngeo362.

Chen, R., S. T. Gille, J. L. McClean, G. R. Flierl, and A. Griesel, 2015: A multiwavenumber theory for eddy diffusivities and its application to the southeast pacific (dimes) region. *J. Phys. Oceanogr.*, **45 (7)**, 1877–1896, doi:10.1175/JPO-D-14-0229.1.

Close, S. E., and A. C. Naveira Garabato, 2012: Baroclinic adjustment in drake passage driven by tropical pacific forcing. *Geophysical Research Letters*, **39 (19)**, doi:10.1029/2012GL053402.

Constantinou, N. C., 2018: A barotropic model of eddy saturation. *J. Phys. Oceanogr.*, **48 (2)**, 397–411, doi:10.1175/JPO-D-17-0182.1.

Constantinou, N. C., and A. M. Hogg, 2019: Eddy saturation of the southern ocean: A baroclinic versus barotropic perspective. *Geophys. Res. Lett.*, **46 (21)**, 12 202–12 212, doi:10.1029/2019GL084117.

Donohue, K. A., K. L. Tracey, D. R. Watts, M. P. Chidichimo, and T. K. Chereskin, 2016: Mean antarctic circumpolar current transport measured in drake passage. *Geophysical Research Letters*, **43 (22)**, 11,760–11,767, doi:10.1002/2016GL070319.

Downes, S. M., and A. M. Hogg, 2013: Southern ocean circulation and eddy compensation in cmip5 models. *J. Climate*, **26 (18)**, 7198–7220, doi:10.1175/JCLI-D-12-00504.1.

Eden, C., and R. J. Greatbatch, 2008: Towards a mesoscale eddy closure. *Ocean Model.*, **20 (3)**, 223 – 239, doi:https://doi.org/10.1016/j.ocemod.2007.09.002.

Egbert, G. D., R. D. Ray, and B. G. Bills, 2004: Numerical modeling of the global semidiurnal tide in the present day and in the last glacial maximum. *J. Geophys. Res.: Oceans*, **109 (C3)**, 2156–2202, doi:10.1029/2003JC001973, c03003.

Farneti, R., T. L. Delworth, A. J. Rosati, S. M. Griffies, and F. Zeng, 2010: The role of mesoscale eddies in the rectification of the southern ocean response to climate change. *J. Phys. Oceanogr.*, **40 (7)**, 1539–1557, doi:10.1175/2010JPO4353.1.

Farneti, R., and P. Gent, 2011: The effects of the eddy-induced advection coefficient in a coarse-resolution coupled climate model. *Ocean Model.*, **39**, 135–145, doi:10.1016/j.ocemod.2011.02.005.

Farneti, R., and Coauthors, 2015: An assessment of antarctic circumpolar current and southern ocean meridional overturning circulation during 1958-2007 in a suite of interannual core-ii simulations. *Ocean Modell.*, **93**, 84–120, doi:https://doi.org/10.1016/j.ocemod.2015.07.009.

Ferrari, R., S. M. Griffies, A. G. Nurser, and G. K. Vallis, 2010: A boundary-value problem for the parameterized mesoscale eddy transport. *Ocean Model.*, **32 (3)**, 143 – 156, doi:https://doi.org/10.1016/j.ocemod.2010.01.004, the magic of modelling: A special volume commemorating the contributions of Peter D. Killworth âĂŞ Part 2.

Flato, G., and Coauthors, 2013: *Evaluation of Climate Models*. IN: T. F. Stocker, D. Qin, G.-K. Plattner, M. Tignor, S.K. Allen, J. Boschung, A. Nauels, Y. Xia, V. Bex and P.M. Midgley (eds.). In: Climate Change 2013: The Physical Science Basis. Contribution of Working Group I to the Fifth Assessment Report of the Intergovernmental Panel on Climate Change. Cambridge University Press. Cambridge, United Kingdom and New York, NY, USA.

Galperin, B., S. Sukoriansky, N. Dikovskaya, P. L. Read, Y. H. Yamazaki, and R. Wordsworth, 2006: Anisotropic turbulence and zonal jets in rotating flows with a β-effect. *Nonlinear Processes Geophys.*, **13 (1)**, 83–98, URL https://hal.archives-ouvertes.fr/hal-00302701.

Gent, P. R., and J. C. McWilliams, 1990: Isopycnal mixing in ocean circulation models. *J. Phys. Oceanogr.*, **20 (1)**, 150–155, doi:10.1175/1520-0485(1990)020<0150:IMIOCM>2.0.CO;2.

Gent, P. R., J. Willebrand, T. J. McDougall, and J. C. McWilliams, 1995: Parameterizing eddy-induced tracer transports in ocean circulation models. *J. Phys. Oceanogr.*, **25 (4)**, 463–474, doi:10.1175/1520-0485(1995)025<0463:PEITTI>2.0.CO;2.

Gnanadesikan, A., 1999: A simple predictive model for the structure of the oceanic pycnocline. *Science*, **283 (5410)**, 2077–2079, doi:10.1126/science.283.5410.2077.

Grianik, N., I. M. Held, K. S. Smith, and G. K. Vallis, 2004: The effects of quadratic drag on the inverse cascade of two-dimensional turbulence. *Phy. Fluids*, **16 (1)**, 73–78, doi:10.1063/1.1630054.

Hallberg, R., and A. Gnanadesikan, 2006: The role of eddies in determining the structure and response of the wind-driven southern hemisphere overturning: Results from the modeling eddies in the southern ocean (meso) project. *J. Phys. Oceanogr.*, **36 (12)**, 2232–2252, doi:10.1175/JPO2980.1.

Hogg, A. M., 2010: An antarctic circumpolar current driven by surface buoyancy forcing. *Geophys. Res. Lett.*, **37 (23)**, doi:10.1029/2010GL044777.

Holton, J. R., 2004: *An Introduction to Dynamic Meteorology (International Geophysics)*, Vol. 88. 4th ed., Elsevier Academic Press, Berlin.

Ito, T., and J. Marshall, 2008: Control of lower-limb overturning circulation in the southern ocean by diapycnal mixing and mesoscale eddy transfer. *J. Phys. Oceanogr.*, **38 (12)**, 2832–2845, doi:10.1175/2008JPO3878.1.

Jansen, M. F., A. Adcroft, S. Khani, and H. Kong, 2019: Toward an energetically consistent, resolution aware parameterization of ocean mesoscale eddies. *J. Adv. Model. Earth Sys.*, **11 (8)**, 2844–2860, doi:10.1029/2019MS001750.

Jansen, M. F., A. J. Adcroft, R. Hallberg, and I. M. Held, 2015: Parameterization of eddy fluxes based on a mesoscale energy budget. *Ocean Model.*, **92**, 28 – 41, doi:https://doi.org/10.1016/j.ocemod.2015.05.007.

Jansen, M. F., L.-P. Nadeau, and T. M. Merlis, 2018: Transient versus equilibrium response of the oceanâĂŹs overturning circulation to warming. *J. Climate*, **31 (13)**, 5147–5163, doi:10.1175/JCLI-D-17-0797.1.

Jones, D. C., T. Ito, and N. S. Lovenduski, 2011: The transient response of the southern ocean pycnocline to changing atmospheric winds. *Geophysical Research Letters*, **38 (15)**, doi:10.1029/2011GL048145.

Karsten, R. H., and J. Marshall, 2002: Constructing the residual circulation of the acc from observations. *J. Phys. Oceanogr.*, **32 (12)**, 3315–3327, doi:10.1175/1520-0485(2002)032<3315:CTRCOT>2.0.CO;2.

Khani, S., M. F. Jansen, and A. Adcroft, 2019: Diagnosing subgrid mesoscale eddy fluxes with and without topography. *J. Adv. Model. Earth Sys.*, **11 (12)**, 3995–4015, doi:10.1029/2019MS001721.

Killworth, P. D., and J. R. Blundell, 1999: The effect of bottom topography on the speed of long extratropical planetary waves. *J. Phys. Oceanogr.*, **29 (10)**, 2689–2710, doi:10.1175/1520-0485(1999)029<2689:TEOBTO>2.0.CO;2.

Kong, H., and M. F. Jansen, 2017: The Eddy Diffusivity in Barotropic β-Plane Turbulence. *Fluids*, **2 (54)**, doi:10.3390/fluids2040054.

Kuhlbrodt, T., R. Smith, Z. Wang, and J. Gregory, 2012: The influence of eddy parameterizations on the transport of the antarctic circumpolar current in coupled climate models. *Ocean Model.*, **52-53**, 1 – 8, doi:https://doi.org/10.1016/j.ocemod.2012.04.006.

Lin, X., X. Zhai, Z. Wang, and D. R. Munday, 2018: Mean, Variability, and Trend of Southern Ocean Wind Stress: Role of Wind Fluctuations. *Journal of Climate*, **31 (9)**, 3557–3573, doi:10.1175/JCLI-D-17-0481.1.

Lumpkin, R., and K. Speer, 2007: Global Ocean Meridional Overturning. *Journal of Physical Oceanography*, **37 (10)**, 2550–2562, doi:10.1175/JPO3130.1.

Mak, J., J. R. Maddison, D. P. Marshall, and D. R. Munday, 2018: Implementation of a geometrically informed and energetically constrained mesoscale eddy parameterization in an ocean circulation model. *J. Phys. Oceanogr.*, **48 (10)**, 2363–2382, doi:10.1175/JPO-D-18-0017.1.

Maltrud, M. E., and G. K. Vallis, 1991: Energy spectra and coherent structures in forced two-dimensional and beta-plane turbulence. *J. Fluid Mech.*, **228**, 321 – 342, doi:10.1017/S0022112091002720.

Marshall, D. P., M. H. P. Ambaum, J. R. Maddison, D. R. Munday, and L. Novak, 2017: Eddy saturation and frictional control of the antarctic circumpolar current. *Geophys. Res. Lett.*, **44 (1)**, 286–292, doi:10.1002/2016GL071702.

Marshall, J., and T. Radko, 2003: Residual-mean solutions for the antarctic circumpolar current and its associated overturning circulation. *J. Phys. Oceanogr.*, **33 (11)**, 2341–2354, doi:10.1175/1520-0485(2003)033<2341:RSFTAC>2.0.CO;2.

Marshall, J., and K. Speer, 2012: Closure of the meridional overturning circulation through southern ocean upwelling. *Nature Geoscience*, **5**, 171–180, doi:10.1038/ngeo1391.

McDermott, D. A., 1996: The Regulation of Northern Overturning by Southern Hemisphere Winds. *Journal of Physical Oceanography*, **26 (7)**, 1234–1255, doi:10.1175/1520-0485(1996)026<1234:TRONOB>2.0.CO;2.

Morrison, A. K., and A. M. Hogg, 2013: On the relationship between southern ocean overturning and acc transport. *J. Phys. Oceanogr.*, **43 (1)**, 140–148, doi:10.1175/JPO-D-12-057.1.

Munday, D. R., H. L. Johnson, and D. P. Marshall, 2013: Eddy saturation of equilibrated circumpolar currents. *J. Phys. Oceanogr.*, **43 (3)**, 507–532, doi:10.1175/JPO-D-12-095.1.

Nadeau, L.-P., and R. Ferrari, 2015: The role of closed gyres in setting the zonal transport of the antarctic circumpolar current. *J. Phys. Oceanogr.*, **45 (6)**, 1491–1509, doi:10.1175/JPO-D-14-0173.1.

Nadeau, L.-P., D. N. Straub, and D. M. Holland, 2013: Comparing idealized and complex topographies in quasigeostrophic simulations of an antarctic circumpolar current. *J. Phys. Oceanogr.*, **43 (8)**, 1821–1837, doi:10.1175/JPO-D-12-0142.1.

Nakamura, N., 1996: Two-dimensional mixing, edge formation, and permeability diagnosed in an area coordinate. *J. Atmos. Sci.*, **53 (11)**, 1524–1537, doi:10.1175/1520-0469(1996)053<1524:TDMEFA>2.0.CO;2.

Nakamura, N., 2001: A new look at eddy diffusivity as a mixing diagnostic. *J. Atmos. Sci.*, **58 (24)**, 3685–3701, doi:10.1175/1520-0469(2001)058<3685:ANLAED>2.0.CO;2.

Nakamura, N., 2008: Sensitivity of global mixing and fluxes to isolated transport barriers. *J. Atmos. Sci.*, **65 (12)**, 3800–3818, doi:10.1175/2008JAS2641.1.

Nakamura, N., and D. Zhu, 2010: Finite-Amplitude Wave Activity and Diffusive Flux of Potential Vorticity in EddyâĂŞMean Flow Interaction. *J. Atmos. Sci.*, **67 (9)**, 2701–2716, doi:10.1175/2010JAS3432.1.

Nikurashin, M., and G. Vallis, 2011: A Theory of Deep Stratification and Overturning Circulation in the Ocean. *Journal of Physical Oceanography*, **41 (3)**, 485–502, doi:10.1175/2010JPO4529.1.

Nikurashin, M., and G. Vallis, 2012: A theory of the interhemispheric meridional overturning circulation and associated stratification. *J. Phys. Oceanogr.*, **42 (10)**, 1652–1667, doi:10.1175/JPO-D-11-0189.1.

Plumb, R. A., and R. Ferrari, 2005: Transformed eulerian-mean theory. part i: Nonquasi-geostrophic theory for eddies on a zonal-mean flow. *J. Phys. Oceanogr.*, **35 (2)**, 165–174, doi:10.1175/JPO-2669.1.

Poulsen, M. B., M. Jochum, and R. Nuterman, 2018: Parameterized and resolved southern ocean eddy compensation. *Ocean Model.*, **124**, 1 – 15, doi:https://doi.org/10.1016/j.ocemod.2018.01.008.

Prandtl, L., 1925: Bericht über untersuchungen zur ausgebildeten turbulenz. *Zeitschrift für angewandte Mathematik und Mechanik*, **5 (2)**, 136–139.

Rhines, P., and F. Bretherton, 1973: Topographic rossby waves in a rough-bottomed ocean. *J. Fluid Mech.*, **61 (3)**, 583–607, doi:10.1017/S002211207300087X.

Rhines, P. B., 1975: Waves and turbulence on a beta-plane. *J. Fluid Mech.*, **69 (3)**, 417–443, doi:10.1017/S0022112075001504.

Sabine, C. L., and Coauthors, 2004: The oceanic sink for anthropogenic co2. *Science*, **305 (5682)**, 367–371, doi:10.1126/science.1097403.

Samelson, R. M., 2011: Time-Dependent Adjustment in a Simple Model of the Mid-Depth Meridional Overturning Cell. *Journal of Physical Oceanography*, **41 (5)**, 1009–1025, doi:10.1175/2010JPO4562.1.

Sinha, A., and R. P. Abernathey, 2016: Time scales of southern ocean eddy equilibration. *J. Phys. Oceanogr.*, **46 (9)**, 2785–2805, doi:10.1175/JPO-D-16-0041.1.

Smith, K. S., G. Boccaletti, C. C. Henning, I. Marinov, C. Y. Tam, I. M. Held, and G. K. Vallis, 2002: Turbulent diffusion in the geostrophic inverse cascade. *J. Fluid Mech.*, **469**, 13–48, doi:10.1017/S0022112002001763.

Srinivasan, K., and W. R. Young, 2014: Reynolds stress and eddy diffusivity of β-plane shear flows. *J. Atmos. Sci.*, **71 (6)**, 2169–2185, doi:10.1175/JAS-D-13-0246.1.

Straub, D. N., 1993: On the transport and angular momentum balance of channel models of the antarctic circumpolar current. *J. Phys. Oceanogr.*, **23 (4)**, 776–782, doi:10.1175/1520-0485(1993)023<0776:OTTAAM>2.0.CO;2.

Swart, N. C., and J. C. Fyfe, 2012: Observed and simulated changes in the southern hemisphere surface westerly wind-stress. *Geophys. Res. Lett.*, **39 (16)**, doi:10.1029/2012GL052810.

Talley, L. D., 2003: Shallow, Intermediate, and Deep Overturning Components of the Global Heat Budget. *Journal of Physical Oceanography*, **33 (3)**, 530–560, doi:10.1175/1520-0485(2003)033<0530:SIADOC>2.0.CO;2.

Thompson, A. F., and A. C. Naveira Garabato, 2014: Equilibration of the antarctic circumpolar current by standing meanders. *J. Phys. Oceanogr.*, **44 (7)**, 1811–1828, doi:10.1175/JPO-D-13-0163.1.

Vallis, G. K., 2006: *Atmospheric and Oceanic Fluid Dynamics*. Cambridge University Press, Cambridge, U.K., 745 pp.

Vallis, G. K., and M. E. Maltrud, 1993: Generation of mean flows and jets on a beta plane and over topography. *J. Phys. Oceanogr.*, **23 (7)**, 1346–1362, doi:10.1175/1520-0485(1993)023<1346:GOMFAJ>2.0.CO;2.

Vasavada, A. R., and A. P. Showman, 2005: Jovian atmospheric dynamics: An update after galileo and cassini. *Rep. Prog. Phys.*, **68 (8)**, 1935–1996, doi:10.1088/0034-4885/68/8/R06.

Viebahn, J., and C. Eden, 2010: Towards the impact of eddies on the response of the southern ocean to climate change. *Ocean Model.*, **34**, 150–165, doi:10.1016/j.ocemod.2010.05.005.

Visbeck, M., J. Marshall, T. Haine, and M. Spall, 1997: Specification of eddy transfer coefficients in coarse-resolution ocean circulation models. *J. Phys. Oceanogr.*, **27 (3)**, 381–402, doi:10.1175/1520-0485(1997)027<0381:SOETCI>2.0.CO;2.

Wang, L., M. Jansen, and R. Abernathey, 2016: Eddy phase speeds in a two-layer model of quasigeostrophic baroclinic turbulence with applications to ocean observations. *J. Phys. Oceanogr.*, **46 (6)**, 1963–1985, doi:10.1175/JPO-D-15-0192.1.

Willebrand, J., and Coauthors, 2001: Circulation characteristics in three eddy-permitting models of the north atlantic. *Progr. Oceanogr.*, **48 (2)**, 123 – 161, doi:http://dx.doi.org/10.1016/S0079-6611(01)00003-9, dynamics of the North Atlantic Circulation: Simulation and Assimilation with High-Resolution Models (DYNAMO).

Wolfe, C. L., and P. Cessi, 2010: What Sets the Strength of the Middepth Stratification and Overturning Circulation in Eddying Ocean Models? *Journal of Physical Oceanography*, **40 (7)**, 1520–1538, doi:10.1175/2010JPO4393.1.

Young, W. R., 2012: An exact thickness-weighted average formulation of the boussinesq equations. *J. Phys. Oceanogr.*, **42 (5)**, 692–707, doi:10.1175/JPO-D-11-0102.1.